

A Novel Microstructured Photocatalytic Membrane Reactor – Application to Micropollutant Removal from Wastewater and to Selective Oxidation of Alcohols

Zur Erlangung des akademischen Grades eines
DOKTORS DER INGENIEURWISSENSCHAFTEN

von der KIT-Fakultät für Chemieingenieurwesen und Verfahrenstechnik des
Karlsruher Instituts für Technologie (KIT)
genehmigte

DISSERTATION

von
(M.Sc.) Xiang Zhan
aus Shandong, China

Tag der mündlichen Prüfung: 28.08.2025

Erstgutachter: Prof. Dr.-Ing. Roland Dittmeyer

Zweitgutachter: Prof. Dr.-Ing. Matthias Franzreb



This document is licensed under a Creative Commons
Attribution-ShareAlike 4.0 International License (CC BY-SA 4.0):
<https://creativecommons.org/licenses/by-sa/4.0/deed.en>

Erklärung

Ich versichere, dass die hier vorliegende Dissertation mit dem eingereichten und genehmigten Prüfungsexemplar der Doktorarbeit übereinstimmt.

Unterschrift

Ort, Datum

*We knew the world would not be the same
A few people laughed
A few people cried
Most people were silent
I remembered the line from the Hindu scripture Bhagavad Gita
“Now I am become Death, the destroyer of worlds.”
I suppose we all thought that
One way or another
- J. Robert Oppenheimer*

Acknowledgement

First and foremost, I extend my sincerest thanks to my supervisor, Prof. Roland Dittmeyer, for granting me the opportunity to pursue this research project. His insightful guidance, unwavering trust, and the academic freedom he provided allowed me to fully immerse myself in this work. The knowledge and skills I gained under his mentorship will continue to benefit me throughout my career. I am also deeply grateful to Prof. Matthias Franzreb for kindly agreeing to serve as the second examiner. Special acknowledgment goes to Dr. Steffen Tischer, who gave a reference when I applied for this PhD position.

I also extend my thanks to my group leader Dr. Michael Rubin, whose meticulous attention to detail, dedication, and steadfast support have been indispensable. Our countless scientific discussions and personal conversations not only enriched my understanding of research principles but also shaped my approach to challenges.

My heartfelt thanks go to my colleagues at IMVT, particularly those from the FAB, ADD, and MAT groups, for their expertise in reactor fabrication and material characterization. I am especially grateful to Chenghao Sun, Wenjin Ding, Oliver Görke, and Andreas Kölbl, whose patient assistance during the initial stages of my work bridged gaps in my chemistry background. Their contributions were pivotal to my progress. I also acknowledge the support of several PhD students, including Paul Kant and Dongxu Xie, as well as many other colleagues whose names I cannot list here individually.

Beyond IMVT, I extend my appreciation to external collaborators whose expertise elevated this work. Foremost among these is Prof. Andrea Schäfer and her team at the Institute for Advanced Membrane Technology, whose profound insights into membrane science greatly influenced my research. Special thanks also go to Dr. Gerald Brenner-Weiß, Frank Kirschhöfer and Dr. Zheqin Dong for their analytical contributions. Additionally, I gratefully acknowledge the financial support provided by the Nanomembrane Initiative of Helmholtz

Association.

Finally, my deepest gratitude belongs to my family. To my parents, whose unwavering emotional and moral support sustained me through every challenge in my master and doctoral study. To my wife, Shuo, your companionship, patience, and resilience transformed this journey's highs and lows into shared triumphs. And to my son, Yi, whose arrival during the final stages of this thesis became my greatest source of joy and motivation.

This thesis stands as a testament to the collective efforts of all who supported me. Thank you.

Abstract

This dissertation delves into the field of photocatalysis, a sustainable approach that leverages light to catalyze chemical reactions and aims at environmental remediation and chemical synthesis. Since the pioneering work on photocatalytic water splitting, photocatalysis has evolved to address the challenge of persistent water pollutants, notably micropollutants like endocrine disrupting compounds, which, despite their minute concentrations, pose considerable environmental and health hazards. This work highlights the synergistic potential of combining photocatalysis with membrane filtration to enhance pollutant degradation and also explores its applicability in selective photooxidation of alcohols.

The first part of this research involves the development of a novel microstructured photocatalytic membrane reactor (μ PMR). This reactor is engineered to operate under well-defined conditions, utilizing TiO_2 -based and C_3N_4 -based catalysts that are effective under both UV and visible light. Innovations include a distinctive light distribution mechanism utilizing optical fibers and a versatile flow system facilitating various operational modes. The catalyst's coating process, achieved through inkjet printing, ensures meticulous control over its loading, thickness, and distribution, which is essential for uniform reaction outcomes and detailed kinetic analysis.

The dissertation presents an extensive study on photocatalytic pollutant degradation within the μ PMR, applying the Langmuir–Hinshelwood model to examine the reaction kinetics, with Rhodamine B (RhB) as a model pollutant. This study accounts for both external and internal mass transport limitations, and introduces a light model to account for light penetration within the catalyst coating. The validation of this kinetic model, which was initially formulated from batch reactor data, was conducted in the μ PMR's surface-flow mode.

Further investigation into photocatalytic degradation showcased the flow-through contactor mode in the μ PMR as significantly more effective at degrading RhB compared to other

modes. The enhanced photocatalytic performance of the μ PMR is attributed to a high mass transport rate enabled by the convective flow due to the flow-through configuration and a high permeate flow rate. Additionally, the standout performance of this mode was partly due to the synergistic effect of combining membrane filtration with photocatalysis, where the increased concentration at the membrane surface - a result of filtration - contributed to enhancing the reaction rate. Such synergy between membrane filtration and photocatalysis has been rarely studied in published works. Tests on light intensity further validated the light transport model, demonstrating closely matched results between experiments and calculations. Additionally, the μ PMR effectively removed micropollutants like Carbamazepine (CBZ), Sulfamethoxazole (SMX), and Bezafibrate (BZF) under UV, visible light, and even real sunlight, achieving more than 60% removal of these pollutants.

The reactor also demonstrated its efficacy in the selective photooxidation of alcohols to aldehydes. The results from preliminary batch reactor experiments reveal that factors such as the solvent used, the type of photocatalyst, the presence of oxygen significantly influence the selectivity and conversion of the reactions. The μ PMR showed its advantage in mass transport when operating in contactor mode, as was also the case in the photodegradation study.

The significance of this dissertation lies in its contribution to both the scientific understanding and practical application of photocatalysis. By developing a system capable of operating under defined conditions, this work lays the groundwork for systematic studies into the kinetics and mechanisms of photocatalytic reactions. This work is expected to advance photocatalysis towards practical applications in addressing pressing environmental challenges and promoting sustainable chemicals production.

Kurzfassung

Diese Dissertation beschäftigt sich mit dem Feld der Photokatalyse, einem nachhaltigen Ansatz, der Licht nutzt, um chemische Reaktionen zu katalysieren, mit dem Ziel der Abwasserreinigung und chemischen Synthese. Aufbauend auf der bahnbrechenden Entdeckung der photokatalytischen Wasserspaltung richtet sich die Photokatalyse nun auf die Herausforderung persistenter Wasserschadstoffe, insbesondere Mikroschadstoffe wie endokrin-disruptive Verbindungen, die trotz ihrer geringen Konzentrationen erhebliche Umwelt- und Gesundheitsrisiken darstellen. Diese Arbeit hebt das synergetische Potenzial der Kombination von Photokatalyse mit Membranfiltration zur Verbesserung der Schadstoffdegradation hervor und erforscht außerdem ihre Anwendbarkeit in der selektiven Photooxidation von Alkoholen.

Der erste Teil dieser Forschung ist die Entwicklung eines neuartigen mikrostrukturierten photokatalytischen Membranreaktors (μ PMR). Dieser Reaktor ist so konstruiert, dass er unter genau definierten Bedingungen arbeitet, wobei TiO_2 -basierte und C_3N_4 -basierte Katalysatoren verwendet werden, die sowohl unter UV- als auch unter sichtbarem Licht wirksam sind. Die erzielten Innovationen umfassen einen ausgefeilten Lichtverteilungsmechanismus, der optische Fasern nutzt, und ein vielseitiges Flusssystem, das verschiedene Betriebsmodi ermöglicht. Der mittels Tintenstrahldruck realisierte Beschichtungsprozess des Katalysators gewährleistet eine sorgfältige Kontrolle über dessen Beladung, Schichtdicke und Verteilung, was für gleichmäßige Reaktionsergebnisse und detaillierte kinetische Analysen unerlässlich ist.

Die Dissertation präsentiert eine umfangreiche Studie zur photokatalytischen Schadstoffdegradation innerhalb des μ PMR, wobei das Langmuir-Hinshelwood-Modell zur Untersuchung der Reaktionskinetik angewendet wird, mit Rhodamin B (RhB) als Modellschadstoff. Diese Studie berücksichtigt sowohl externe als auch interne Stofftransportbeschränkungen und führt ein Lichttransportmodell ein, um die

Lichtpenetration innerhalb der Katalysatorbeschichtung zu berücksichtigen. Die Validierung dieses kinetischen Modells, das ursprünglich auf Basis von Daten aus einem Batchreaktor formuliert wurde, wurde im Oberflächenströmungsmodus des μ PMR durchgeführt.

Weitere Untersuchungen zur photokatalytischen Degradation zeigten, dass der Durchflusskontaktmodus im μ PMR deutlich effektiver beim Abbau von RhB ist im Vergleich zu anderen Modi. Die verbesserte photokatalytische Leistung des μ PMR ist auf eine hohe Stofftransportrate zurückzuführen, die durch die Konvektionsströmung aufgrund der Durchflusskonfiguration und eine hohe Permeatflussrate ermöglicht wird. Zusätzlich wurde die herausragende Leistung dieses Modus teilweise durch den synergetischen Effekt der Kombination von Membranfiltration mit Photokatalyse ermöglicht, wobei die erhöhte Konzentration an der Membranoberfläche – ein Ergebnis der Filtration – zur Steigerung der Reaktionsrate beitrug. Eine solche Synergie zwischen Membranfiltration und Photokatalyse wurde in veröffentlichten Arbeiten selten untersucht. Tests zur Lichtintensität validierten weiter unser Lichtmodell und zeigten eng übereinstimmende Ergebnisse zwischen Experimenten und Berechnungen. Zusätzlich entfernte der μ PMR effektiv Mikroschadstoffe wie Carbamazepin (CBZ), Sulfamethoxazol (SMX) und Bezafibrat (BZF) unter UV-, sichtbarem Licht und sogar unter echtem Sonnenlicht und erreichte eine Entfernung dieser Schadstoffe von mehr als 60%.

Der Reaktor bewies auch seine Wirksamkeit bei der selektiven Photooxidation von Alkoholen zu Aldehyden. Die Ergebnisse von vorläufigen Batchreaktorexperimenten zeigen, dass Faktoren wie das verwendete Lösungsmittel, die Art des Photokatalysators und die Anwesenheit von Sauerstoff die Selektivität und den Umsatzgrad der Reaktionen erheblich beeinflussen. Der μ PMR zeigt seinen Vorteil im Stofftransport, wenn er im Kontaktmodus betrieben wird, wie auch im Fall der Photodegradationsstudie.

Die Bedeutung dieser Dissertation liegt in ihrem Beitrag zum wissenschaftlichen Verständnis und zur praktischen Anwendung der Photokatalyse. Durch die Entwicklung eines Systems, das unter definierten Bedingungen betrieben werden kann, legt diese Arbeit den Grundstein für systematische Studien zur Kinetik und zu den Mechanismen photokatalytischer Reaktionen. Diese Arbeit zielt darauf ab, die Photokatalyse in Richtung praktischer Anwendungen weiterzuentwickeln – insbesondere zur Bewältigung drängender Umweltprobleme und zur Förderung nachhaltiger chemischer Produktionsverfahren.

Publications

Parts of the present thesis have already been published by the author in peer-reviewed journals or presented at national and international conferences.

Publications in peer-reviewed international Journals:

X. Zhan, C. Yan, Y. Zhang, G. Rinke, G. Rabsch, M. Klumpp, A.I. Schäfer, R. Dittmeyer, Investigation of the reaction kinetics of photocatalytic pollutant degradation under defined conditions with inkjet-printed TiO₂ films – from batch to a novel continuous-flow microreactor, *Reaction Chemistry & Engineering*, 5 (2020) 1658–1670.

Z. Dong, H. Cui, H. Zhang, F. Wang, **X. Zhan**, F. Mayer, B. Nestler, M. Wegener, P.A. Levkin, 3D printing of inherently nanoporous polymers via polymerization-induced phase separation, *Nature Communications*, 12 (2021).

X. Zhan, Y. Wang, M. Rubin, Y. Bao, F. Kirschhöfer, G. Brenner-Weiß, A.I. Schäfer, R. Dittmeyer, A novel microstructured photocatalytic membrane reactor for enhanced photodegradation of micropollutants - from process understanding to practical application, *Separation and Purification Technology*, submitted.

Presentations at national and international conferences:

X. Zhan, C. Yan, M. Klumpp, A. Schaefer, R. Dittmeyer. Inkjet-printing of photocatalyst on inorganic membranes for photocatalytic degradation of micropollutants. Poster. 51. Jahrestreffen Deutscher Katalytiker, March 14-16, 2018, Weimar, Germany.

X. Zhan, Y. Zhang, H. Yu, C. Yan, F. Kirschhöfer, M. Klumpp, G. Brenner-Weiß, A. Schäfer, R. Dittmeyer. Degradation of micropollutant in a novel microstructured photocatalytic membrane reactor. Oral presentation. 27th PhotoIUPAC Dublin 2018, July 8-13, 2018, Dublin, Ireland.

X. Zhan, Y. Zhang, H. Yu, C. Yan, G. Rinkel, G. Rabsch, M. Klumpp, A. Schäfer, R. Dittmeyer. Photocatalytic micropollutant degradation and organic synthesis in a novel microstructured membrane reactor. Poster. The 30th GCCCD (Gesellschaft Chinesischer Chemiker und Chemieingenieure in der Bundesrepublik Deutschland e.V.) Annual Conference, Oct. 12-13, 2018, Karlsruhe, Germany.

X. Zhan, Y. Zhang, M. Klumpp, A. Schäfer, R. Dittmeyer. Degradation of micropollutant in a novel microstructured photocatalytic membrane reactor. Oral presentation. International Conference on Micro Reaction Technology - IMRET 2018, October 21-24, 2018, Karlsruhe, Germany.

X. Zhan, C. Yan, Y. Wang, N. M. Jaramillo, F. Kirschhöfer, G. Rinkel, G. Rabsch, M. Klumpp, G. Brenner-Weiß, A. Schäfer, R. Dittmeyer. Degradation of micropollutant in a microstructured photocatalytic membrane reactor. Oral presentation. The 14th International Conference on Catalysis in Membrane Reactors (ICCMR14), July 8–11, 2019, Eindhoven, The Netherlands.

Contents

Acknowledgement	iii
Abstract	v
Kurzfassung	vii
Publications.....	ix
Contents	xi
1. Introduction.....	1
1.1 Background and motivation.....	1
1.2 State-of-the-art	3
1.2.1 Photocatalysis and photocatalysts	3
1.2.2 Photocatalytic reactors	8
1.2.3 Kinetic studies.....	19
1.3 Objectives of this dissertation.....	22
2. Experimental procedures and characterization	25
2.1 Microstructured photocatalytic membrane reactor (μ PMR).....	25
2.1.1 Development of the μ PMR	25
2.1.2 Continuous-flow system.....	27
2.2 Development of catalytically active coatings	30
2.2.1 Coatings for photodegradation	30
2.2.2 Coatings for selective photooxidation.....	40
2.3 Experimental protocol and analytics.....	50
2.3.1 Photodegradation.....	50

2.3.2 Selective photooxidation	57
3. Photocatalytic degradation of pollutant	63
3.1 Kinetic study - from batch to continuous-flow microreactor	63
3.1.1 Modelling	64
3.1.2 Assessment of the reaction kinetics	70
3.1.3 Discussion.....	79
3.2 Study on process enhancement in μ PMR and practical application	81
3.2.1 Flow mode comparison	81
3.2.2 Process intensification – evaluation of mass transport, synergistic effect of filtration and degradation, and light intensity.....	84
3.2.3 Photodegradation of micropollutants.....	93
3.2.4 Photodegradation under real sunlight.....	96
3.2.5 Discussion.....	97
4. Selective photooxidation of alcohols	99
4.1 Experiment in a batch reactor.....	99
4.1.1 Experimental condition study.....	100
4.1.2 Various substrates.....	103
4.2 Photooxidation of benzyl alcohol in the μ PMR	105
4.3 Discussion	107
5. Summary and conclusions	109
6. Outlook	111
Abbreviations and symbols	113
References	119
Appendix	135

1. Introduction

1.1 Background and motivation

Photocatalysis has gained recognition as an eco-friendly technology that utilizes photons as "traceless and green reagents" [1]. Since the pivotal discovery of photocatalytic water splitting by Fujishima et al. in 1972 [2], photocatalysis has been intensively explored across diverse applications including water and air purification, fuel generation, and pharmaceutical synthesis [3, 4].

The treatment of water pollutants has become a focus area, given its potential to mitigate environmental challenges [5, 6]. Much of the existing research in photocatalytic water treatment has used dyes like Methylene Blue (MB) and Rhodamine B (RhB) as model pollutants. However, recent literature increasingly targets the degradation of micropollutants like endocrine disrupting compounds (EDCs), often found in pharmaceuticals [7-13]. Though present in trace amounts - ranging from several ng L^{-1} to a few $\mu\text{g L}^{-1}$ - these compounds represent a considerable environmental and public health risk [14]. They not only disrupt hormonal balance in aquatic life [15-17], but can also have cumulative adverse effects on human health, even at low concentrations [18].

Traditional decontamination methods such as physical separation and biological oxidation are often inadequate for eliminating these persistent micropollutants [1, 9]. Chemical purification methods, such as chlorination and ozonation, come with high operational costs and the risk of generating toxic by-products [19]. Membrane-based techniques like nanofiltration and reverse osmosis offer higher removal rates but are energy-intensive [20-22].

Photocatalysis offers a promising alternative. Emerging research indicates that integrating photocatalysis with traditional methods could result in synergistic improvements in pollutant degradation [23-27]. One such novel approach involves coupling membrane filtration with

photocatalysis. The membrane serves both as a selective barrier against pollutants and as a substrate for immobilized catalysts. This system takes advantage of concentration polarization to accelerate reaction rates, a concept supported by the theoretical work of Deba et al. [28-30], although it still awaits comprehensive experimental validation.

Apart from degrading pollutants, photocatalysis offers exciting possibilities in chemical synthesis, particularly under milder conditions and with cost-efficient energy inputs compared to traditional thermal catalytic processes [31, 32]. Photocatalysts can generate both oxidizing and reducing species after excitation, and therefore maybe suited for organic synthesis via either oxidative [33-35] or reductive pathways [36, 37]. Recently, the field of photochemical/photocatalytic synthesis has seen a surge of interest in the selective oxidation of alcohols to the corresponding aldehydes, a critical transformation in industrial catalysis [38, 39].

Reactors also play a pivotal role in photochemical reaction engineering [40]. While batch reactors have been the go-to design for evaluating catalysts [41, 42], continuous-flow systems like microreactors and photocatalytic membrane reactors (PMRs) offer distinct advantages [43-46]. Even more promising is the microstructured PMR (μ PMR), a subject seldom covered in existing literature [25, 47-50]. Given that operational parameters like light type and intensity, flow rate, transmembrane pressure, and catalyst loading significantly influence the effectiveness of photocatalytic reactions, PMRs operating under well-defined conditions could offer a platform for targeted research, such as in-depth kinetic studies and proof-of-concept tests for various reactions [50-52].

1.2 State-of-the-art

1.2.1 Photocatalysis and photocatalysts

Photocatalysis is broadly categorized into homogeneous and heterogeneous types. In homogeneous photocatalysis, all reacting species are typically in the same physical state, often liquid [53, 54]. Heterogeneous photocatalysis involves reacting species in different physical states, generally featuring a solid-phase catalyst and liquid-phase reagents and products [3, 55]. Heterogeneous photocatalysis is preferred over homogeneous photocatalysis due to the stability, easy separation, and reusability of the catalysts, which are usually semiconductors [19, 56]. In this thesis, the focus is on heterogeneous photocatalysis. Unless otherwise specified, "heterogeneous photocatalysis" is referred to as simply "photocatalysis".

1.2.1.1 Mechanism of photocatalysis

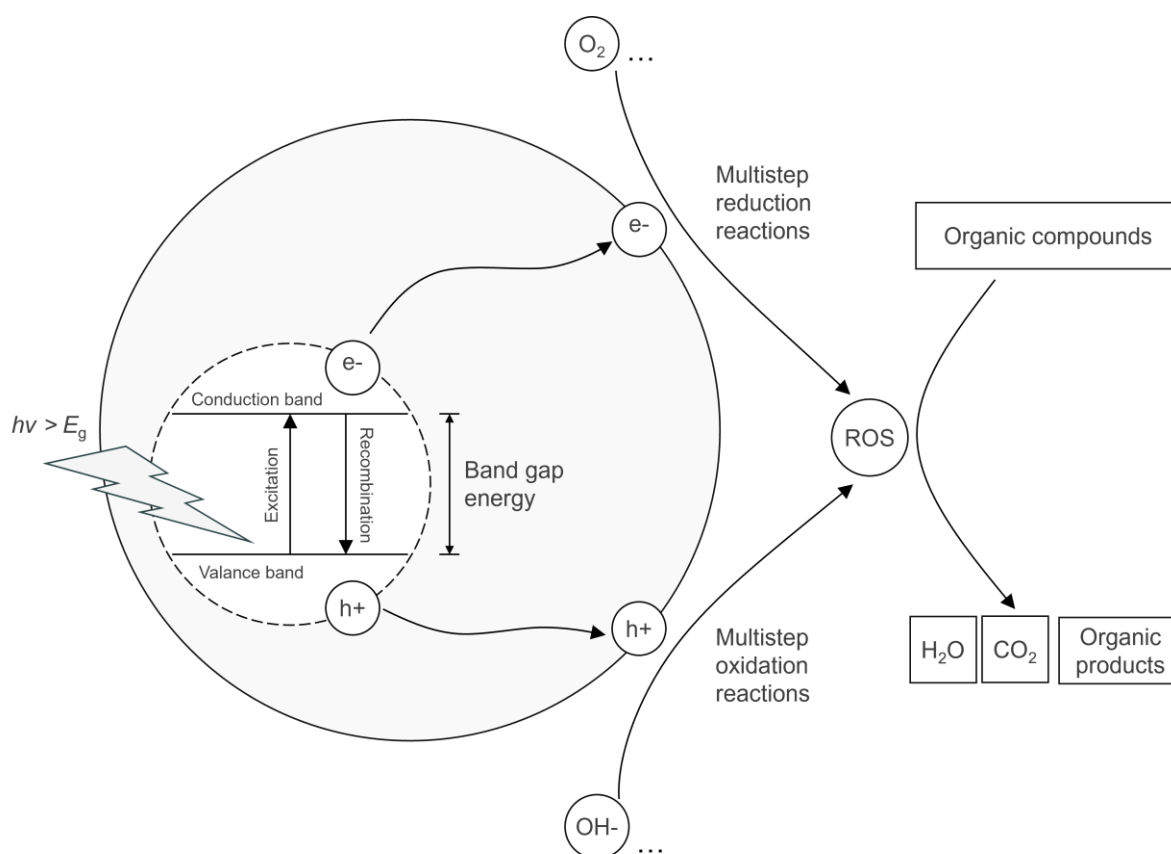
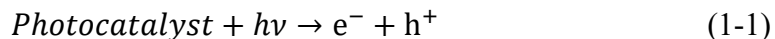


Figure 1-1 Schematic of the photocatalysis mechanism [57]

In photocatalysis, the process begins when a semiconductor catalyst is activated by light, as illustrated in Figure 1-1. When the absorbed energy, denoted as $h\nu$ (where h is Planck's constant and ν is the frequency), surpasses the catalyst's bandgap energy (E_g), it excites

electrons from the valence band to the conduction band. This results in highly reactive electrons (e^-) in the conduction band and positively charged holes (h^+) in the valence band:



These activated carriers (e^- and h^+) can then migrate to the surface of the catalyst, where they interact with water, oxygen, or hydroxyl groups of adsorbed chemicals to generate various reactive oxygen species (ROS) such as superoxide radicals ($O_2^{\cdot-}$), hydrogen peroxide (H_2O_2), and hydroxyl radicals (OH^\cdot) [38, 58]. The most important reactions involved to generate ROS are the following:

Reduction of oxygen:



Ionization of water:



Formation of hydroxyl radicals:



Protonation of superoxide:



Formation of hydrogen peroxide:



H_2O_2 will be resolved again with e^- into OH^- and OH^\cdot [59]:



Hydroxyl radicals are particularly effective in oxidizing and mineralizing almost all organic molecules into carbon dioxide (CO_2) and inorganic ions, making them highly important for the photodegradation of pollutants [15]. However, the recombination of these electrons and holes can happen inside or on the surface of a particle, which significantly limits the generation of ROS. One way to mitigate this is to introduce oxygen, which acts as an electron scavenger, thus

boosting the concentration of the holes and subsequently enhancing the production of hydroxyl radicals and overall photodegradation [25].

ROS are also key players in photooxidation reactions, particularly for the selective oxidation of alcohols to aldehydes [60]. This process involves the adsorption of an alcohol via its hydroxyl groups onto the photocatalyst surface. ROS then trigger the deprotonation of these groups, efficiently converting alcohols to aldehydes [38]. It is worth noting that different ROS have varying levels of reactivity; while some are selective and only partially convert alcohols, more aggressive ROS like hydroxyl radicals may fully oxidize alcohols into CO₂ and water [58].

For a typical heterogeneous photochemical reaction, assuming that the process is irreversible, the general steps can be outlined as follows, as illustrated in Figure 1-2 [61-63]:

- (1) Diffusion of reactant from the bulk solution to the external surface of the catalyst;
- (2) Diffusion of reactant inside the pores towards the center of the catalyst particle;
- (3) Reversible adsorption of reactant at an active site;
- (4) Photochemical reactions that lead to product formation;
- (5) Desorption of the formed product(s) from the active sites;
- (6) Diffusion of product(s) inside the pores towards the external surface of the catalyst;
- (7) Diffusion of product(s) back to the bulk solution;

Steps 1 and 7 are described by a mass transfer coefficient β_m , which is influenced by multiple factors, such as liquid properties, reactor configuration, flow regime, and the diffusion coefficient of the materials being transferred from the bulk [63, 64]. Steps 2 and 6 are characterized by an effective diffusivity D_{eff} . Steps 3 and 5 are determined by adsorption-equilibrium, quantified by the equilibrium constant K_{ad} . This constant is dependent on various physico-chemical properties like surface charge, pH, and ionic strength [65, 66]. Step 4 is governed by the chemical reaction(s), with kinetics described by the reaction rate constant k . Note that Step 4 may be actually composed of many reaction steps depending on the mechanism.

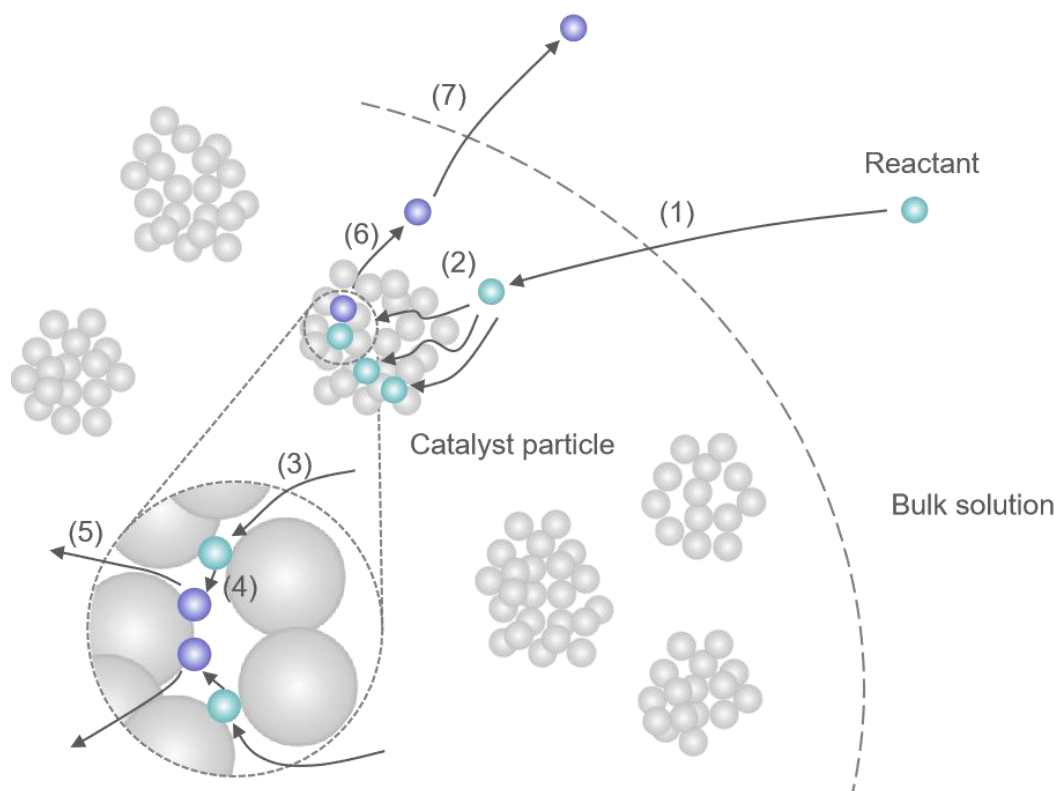


Figure 1-2 Main steps in heterogeneous photochemical reaction.

It is also critical to emphasize that light transmission in photocatalytic systems significantly impacts overall process efficiency and quantum yield [62]. In reactors employing immobilized catalysts, photon penetration depth is highly dependent on the catalyst layer thickness. For instance, as illustrated in Figure 1-3, light intensity can exhibit a nonlinear decline within porous catalyst layer due to scattering effects (e.g., diffraction, reflection), thereby reducing light utilization efficiency [67]. To address these challenges, recent studies have incorporated light attenuation models into kinetic analyses. These models quantify how photon flux diminishes with depth in porous media, enabling the correlation between local light intensity and reaction rates (reviewed in Section 1.2.3.).

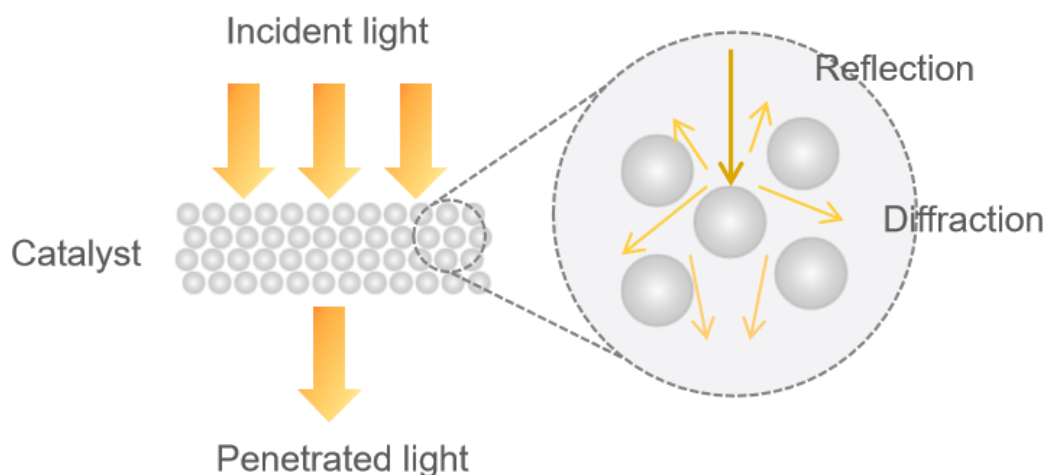


Figure 1-3 Light decay through catalyst layer.

1.2.1.2 Photocatalysts

Numerous photocatalysts, predominantly semiconductors, have been explored for their efficacy in pollutant degradation. Among them, titanium dioxide (TiO_2) stands out for its affordability, non-toxicity, and chemical stability [4, 68]. However, TiO_2 is primarily activated by ultraviolet (UV) light, which constitutes a mere 5% of the total solar energy. To tap into the potential of visible light, researchers commonly modify TiO_2 by narrowing its band gap. This is achieved by doping with nonmetal elements (N [69], C [70], and S [71]) or metal elements (Pt [72], Fe [73], and Mn [74]), forming composite catalysts such as graphene- TiO_2 [75], carbon nanotubes- TiO_2 [76], etc. Additionally, WO_3 [77], Bi_2WO_6 [78], MoS_2 [79], SnWO_4 [80] and graphite carbon nitride [81] have been studied for pollutant degradation in the visible light spectrum.

For the selective organic synthesis, several semiconductor photocatalysts have been evaluated. However, when UV light is employed, the risk of forming undesirable by-products due to over-oxidation is significant, leading to compromised selectivity for the targeted aldehydes or ketones [38]. For instance, photooxidation of benzyl alcohol under UV light and aerobic conditions produces not just benzaldehyde, but also CO_2 and benzoic acid [82]. To address this issue, photocatalysts responsive to visible light have been developed to improve both light harvesting and reaction selectivity.

In general, the engineering of visible-light-responsive photocatalysts for photooxidation of alcohols can be accomplished through various strategies like doping, defect engineering, and the construction of hetero-structures using wide-band and narrow-band semiconductors. A range of materials such as oxides [83-85], sulfides [86-88], nitrides [89-93], metal-organic

frameworks (MOFs) [94], covalent organic frameworks (COFs) [95, 96], and their hybrid variants [97-99] have been studied for this purpose. Among these, graphitic carbon nitride (g-C₃N₄) has garnered significant attention due to its unique features, including chemical robustness - being insoluble in acids, alkalis, or organic solvents - and thermal stability up to 600°C, in addition to its straightforward preparation from readily available, nitrogen-rich precursors [100, 101]. g-C₃N₄ has relatively mild oxidation capacity and shows much higher selectivity towards partial oxidation products [102]. These attributes make g-C₃N₄ an excellent option for selective photooxidation reactions.

1.2.2 Photocatalytic reactors

In the field of reactor design for photochemical processes, key factors to consider include limitations in photon and mass transfer, as well as scalability [103]. Furthermore, creating reactors that can function under well-defined conditions is essential for specialized studies, such as kinetic analysis and examinations of catalytic mechanisms.

Photocatalytic reactors can be categorized into two primary configurations based on the state of the photocatalyst [41, 42, 47]: 1) slurry reactors with suspended photocatalysts, and 2) fixed-bed reactors with immobilized photocatalysts.

Slurry reactors, commonly described in literature as batch systems with continuous stirring, are often used for evaluating photocatalysts and typically yield higher reaction rates than fixed-bed reactors due to fewer diffusion limitations for reactants moving from the bulk solution to the catalyst [48, 104]. However, they require an extra step to separate the catalyst from the solvent, usually through filtration, which adds both complexity and cost to the overall process [104]. Moreover, the suspended catalyst particles induce significant light scattering, severely restricting light penetration depth - particularly at high catalyst loadings or with larger particle sizes [105]. Furthermore, undefined hydrodynamic conditions (e.g., uneven stirring, particle aggregation) and non-uniform light distribution in large-scale slurry reactors complicate process reproducibility, making performance prediction and process control challenging for scaling-up [106]. Additionally, while nanoscale particles minimize bulk diffusion limitations, they may introduce intraparticle pore diffusion barriers when the photocatalyst possesses mesoporous structure, or when particle agglomeration occurs, paradoxically diminishing the expected advantages of the suspended catalyst system [64].

On the other hand, fixed-bed reactors with immobilized photocatalysts eliminate the need for post-reaction catalyst separation, making it more suitable for industrial applications [48].

Particularly, fixed-bed reactors operating under continuous-flow have received considerable attention in recent research [103]. However, this configuration comes with its own set of challenges, outlined as three key constraints [67]:

- 1) external mass transport may restrict the overall reaction kinetics, particularly in laminar flow conditions at low fluid flow rates, because the diffusion of the reactant from the bulk fluid to the catalyst layer may not be sufficiently fast;
- 2) internal mass transport within the catalyst layer can also be a limiting factor, depending on the thickness of the layer;
- 3) photon transmission inside the catalyst layer may decrease dramatically due to factors such as diffraction, adsorption and reflection, etc., which may compromise the light utilization efficiency.

This section will focus on recent advancements in continuous-flow photocatalytic reactors, particularly those designed for photodegradation and photooxidation that use immobilized catalysts.

1.2.2.1 Reactors for photodegradation

In this section, photocatalytic reactors with immobilized photocatalyst are reviewed. These reactors can be categorized into three types: conventional fixed-bed photocatalytic reactors (FPR), micro-structured photocatalytic reactors, and photocatalytic membrane reactors (PMR).

1) Conventional fixed-bed photocatalytic reactor (FPR)

One common design for conventional FPR involves coating the photocatalyst on the reactor walls, which can be either flat or curved, as illustrated in Figure 1-4 (a). The most frequently used substrates for this approach are glass slides or tubes [107-109], while membranes [110, 111] and stainless steel [112] have also been utilized. Oftentimes, this setup yields lower degradation efficiency due to its reduced surface-to-volume ratio when compared to slurry reactors.

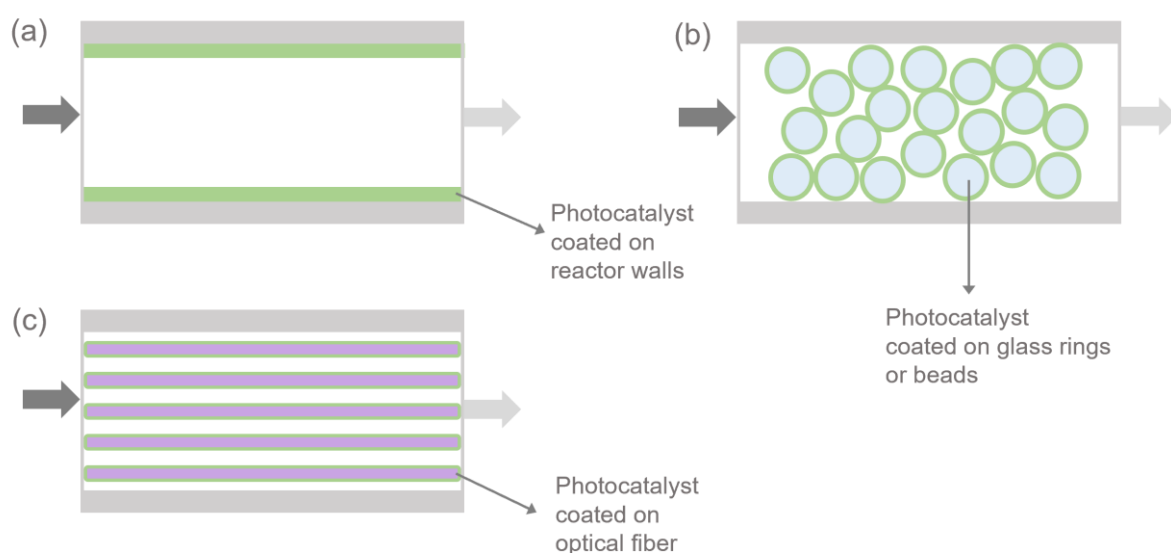


Figure 1-4 Three typical types of normal FPR, differentiated by the substrate on which the photocatalyst is coated: (a) coated on reactor walls; (b) coated on translucent glass rings or beads; (c) coated on optical fibers. Green film represents the coated photocatalyst.

Figure 1-4 (b) shows an alternative configuration that employs glass beads [113-115] or rings [108] as the immobilizing substrate. Claes et al. [113] argue that this design allows for higher catalyst loading and photon utilization efficiency, resulting in enhanced reaction rates. They also noted that reducing the size of the glass beads could potentially ease external mass transport limitations.

Manassero et al. compared the degradation of clofibric acid under continuous-flow conditions using TiO_2 coatings on both flat glass plates and glass rings [108]. Their findings suggest that both configurations produce similar degradation rates under comparable catalyst loading. However, the glass ring setup exhibits superior potential due to its over 20 times higher surface area per reactor volume available for catalyst coating and more uniform radiation distribution across the reaction space. This enhanced photon utilization directly translates to a quantum efficiency (reaction rate per absorbed photon) nearly 1.5 times higher for the glass ring setup compared to the flat plate setup. The disparity arises because the larger surface area of the glass rings allows for greater catalyst accessibility, while their geometry promotes uniform light penetration, minimizing localized photon starvation.

Optical fibers offer another typical reactor configuration, as depicted in Figure 1-4 (c) [116, 117]. With the photocatalyst coated on multiple optical fibers while the pollutant solution flows over their surfaces, this design also provides a higher surface-to-volume ratio. However, it generally falls short in terms of light utilization efficiency [113].

Considering the aforementioned challenges associated with FPRs, submerging a catalytic substrate in a large volume of solution generally results in slower overall conversion rates. Therefore, efforts to enhance the degradation could focus on optimizing the mass transfer between the immobilized photocatalyst and the dissolved contaminant while maintaining effective photon transfer within the catalyst layer.

2) Microstructured photocatalytic reactor

Microstructured photocatalytic reactors, also known as photocatalytic microreactors, provide efficient mass transport, even under laminar flow conditions. Typically, these microreactors feature one or more channels with widths and/or depths ranging from several tens to a few hundred micrometers [45]. The reduced diffusion path length between the bulk pollutant solution and the catalyst layer substantially mitigates external mass transport limitations, addressing a key challenge associated with catalyst immobilization [118]. Additionally, internal mass transport and light transmission within the catalyst layer can be optimized through careful selection of layer thickness, porosity and pore sizes of the catalyst [62-64].

Previous studies have employed continuous-flow microreactors with immobilized TiO_2 for photocatalytic water treatment [25, 63, 64, 119-121]. For example, the reactor shown in Figure 1-5 features a stainless-steel microchannel plate with immobilized Ag/TiO_2 catalyst, and its performance was evaluated under UV irradiation for the degradation of terephthalic acid [122]. According to a recent comparative study that evaluated different reactors for TiO_2 -based photocatalytic water treatment [113], microreactors demonstrated superior reaction kinetics compared to conventional slurry reactors in terms of space-time yield. However, to meet the demands of practical applications in terms of throughput, a well-designed strategy for scaling-up and numbering-up microchannel-based systems is essential [1, 113].

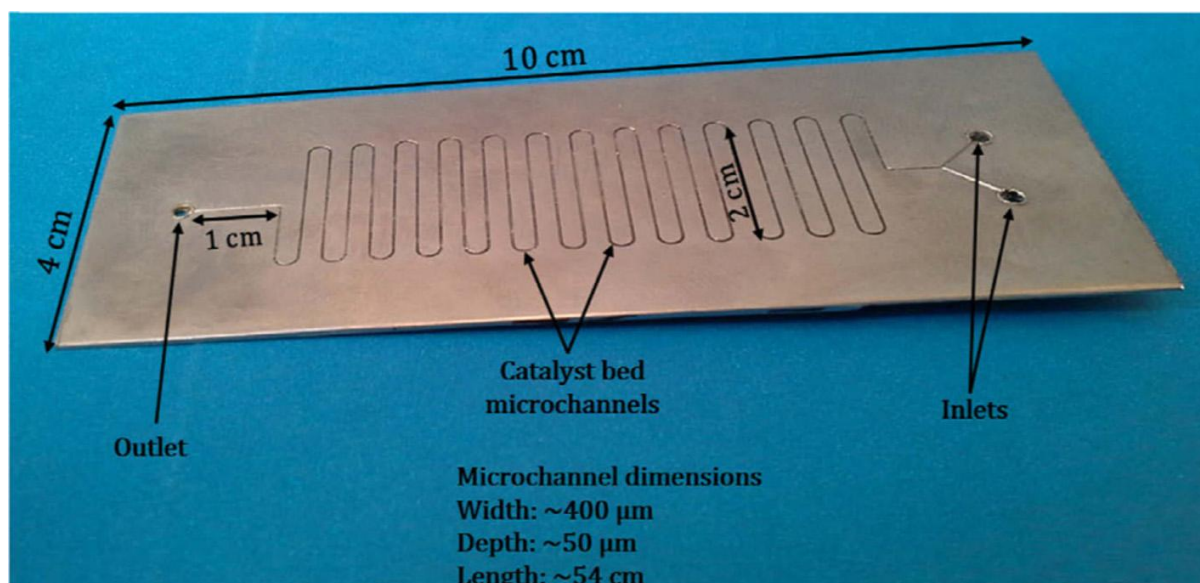


Figure 1-5 Microreactor fabricated with stainless steel plate coated by Ag/TiO₂ catalyst for terephthalic acid degradation. [122]

3) Photocatalytic membrane reactor (PMR)

Recent advancements in the development of photocatalytic reactors have increasingly focused on integrating membrane filtration with photocatalysis to create photocatalytic membrane reactors (PMRs) [103, 123]. In these systems, membranes either serve to separate catalyst particles post-reaction in slurry reactors or act as substrates for catalyst immobilization in fixed-bed reactors. PMRs featuring immobilized photocatalysts have gained particular attention for several key reasons: (1) they simplify system operations by eliminating the need for an additional catalyst separation step [104]; (2) photodegradation on the membrane surface can mitigate fouling issues commonly encountered when using nanofiltration (NF) or reverse osmosis (RO) [21, 22, 124]; (3) enhanced contact between the pollutant and the photocatalyst can be achieved in a "contactor" mode when, e.g., the aqueous solution flows through the catalyst layer and the membrane, as shown in Figure 1-6 (a) [106, 110, 111, 125, 126]; (4) reactants such as oxygen can be distributed evenly via the membrane to the reaction zone, which can enhance the degradation, as shown in Figure 1-6 (b) [25].

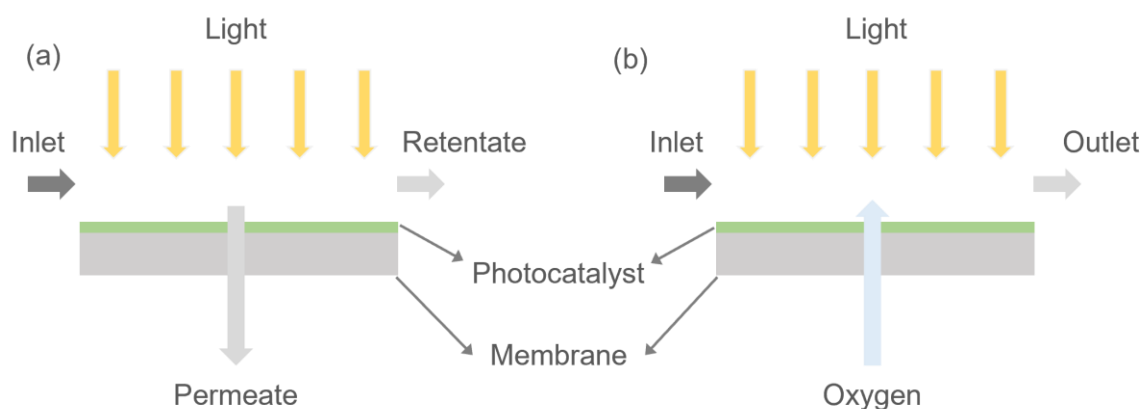


Figure 1-6 Two typical configurations of PMR: (a) mixed flow-through and surface-flow contactor which is a cross-flow mode; (b) pure surface-flow contactor with built-in oxygen distributor.

Much of the existing research has centered on flow-through PMRs. For instance, Horovitz et al. achieved higher Carbamazepine (CBZ) removal by flowing the pollutant solution through an N-doped TiO_2 coated membrane under visible light [110]. They claim that the results can be attributed to the enhanced mass transport between the reactants and the coated photocatalyst. Similar results were reported by Regmi et al., who compared PMRs operating in different flow modes [111]. Lotfi et al. reported up to 94% removal of β -Oestradiol (E2) using TiO_2 -coated polyethersulfone membranes in a dead-end PMR system [11]. Numerous other researchers have developed continuous-flow PMRs that have effectively removed dyes and micropollutants under both UV and visible light conditions [24, 28-30, 127-133].

Some studies have explored the potential of using oxygen-distribution modes through membranes, as shown in Figure 1-6 (b). A representative work by Aran et al. employed a porous Al_2O_3 membrane with TiO_2 -coated microchannels for oxygen supply, significantly enhancing phenol degradation, and the reactor setup is shown schematically in Figure 1-7 [25]. However, this setup showed only marginal improvements for methylene blue (MB) degradation, highlighting the system's limitations concerning gaseous reactant requirements [22].

Despite the promising outcomes, several challenges still remain for PMRs: (1) most PMRs operate on a millimeter scale for reaction zones or channels. Implementing the reaction in a PMR with micrometer-scaled channels could be beneficial for improving mass transport, as well as controlling the reaction under well-defined conditions, which has not been very much presented except the aforementioned work by Aran et al. [25]; (2) most studies on PMR for pollutant degradation assert that the forced flow-through mode (e.g., dead-end flow) enhances mass transport compared to surface-flow mode but often lack a theoretical analysis; and (3)

higher local reaction rates can potentially be achieved through concentration polarization, especially when using membranes with lower molecular weight cut-off (MWCO) such as NF membranes. Although some simulative studies have been conducted by Deba et al. [28], there are few experimental studies as yet discussing this interesting effect.

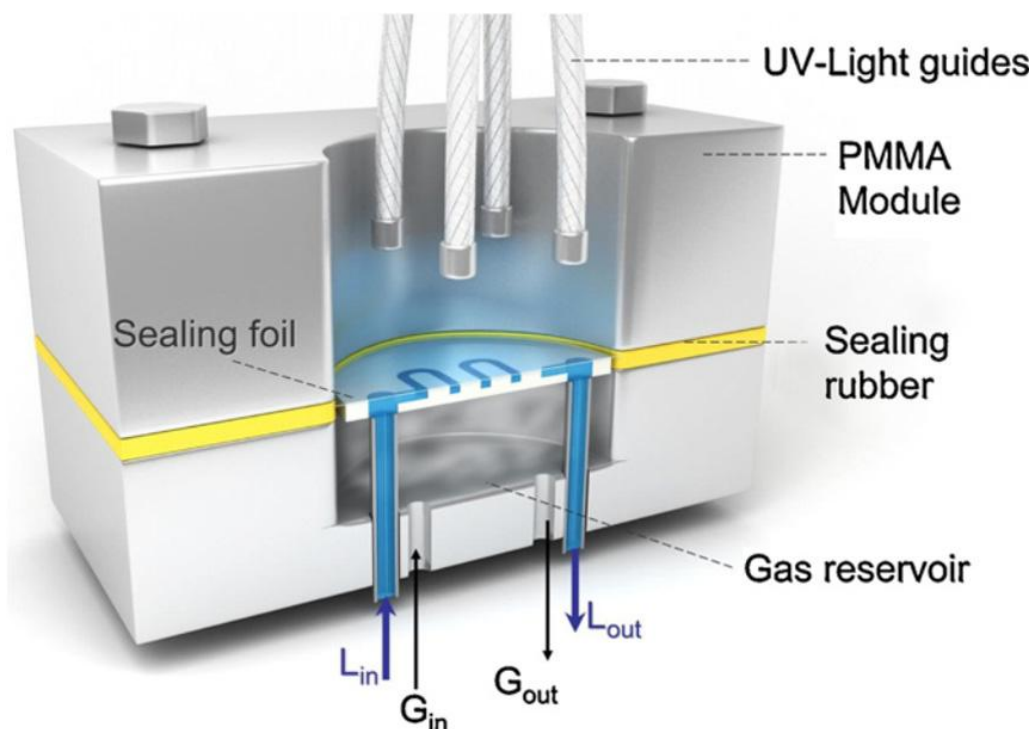


Figure 1-7 A PMR employing oxygen-distribution mode for MB and phenol degradation. [25]

1.2.2.2 Reactors for photocatalytic synthesis

Compared to wastewater treatment, less progress has been made in reactor development for general photocatalytic synthesis. Most studies utilize slurry reactors, typically in batch mode, to assess catalyst behavior. Continuous-flow fixed-bed reactors are relatively less documented.

Figure 1-8 depicts some standard reactor structures for photocatalytic synthesis: falling film reactor, packed-bed reactor, and wall-coated microreactor.

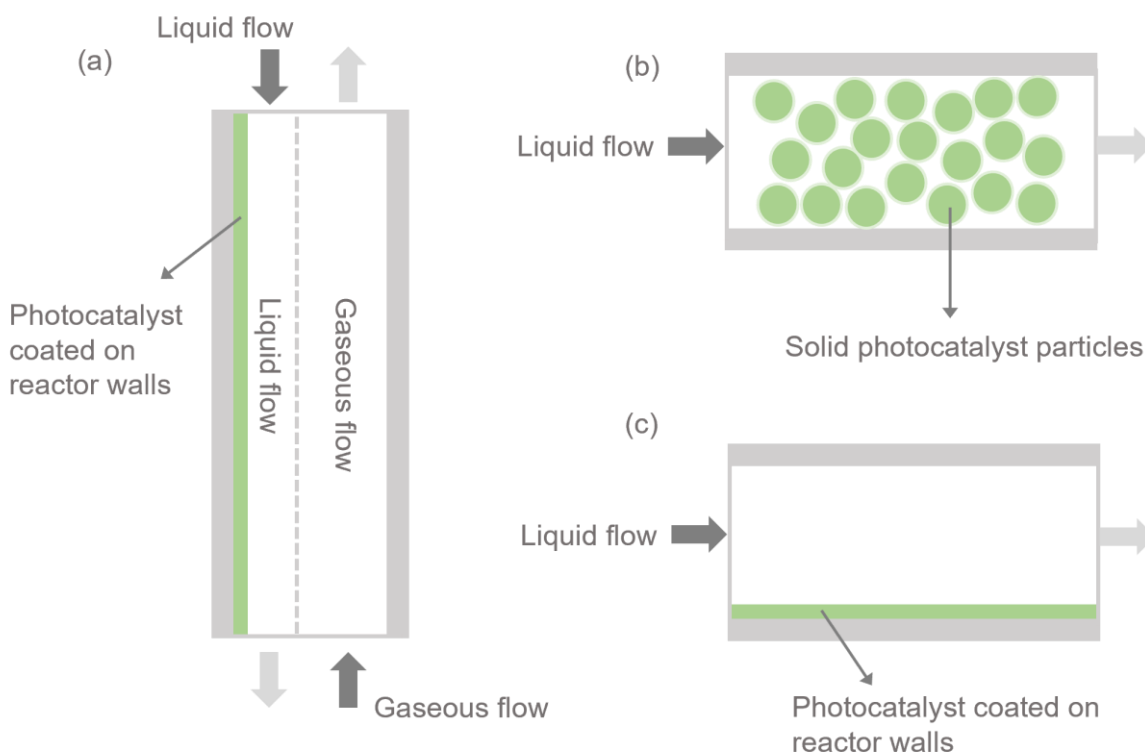


Figure 1-8 Typical fixed-bed reactors for photocatalytic synthesis: (a) falling-film reactor with gaseous counter flow [134]; (b) packed-bed reactor [135]; (c) wall-coated microreactor [136-138]

1) Continuous-flow fixed-bed reactors for general photocatalytic synthesis

Falling film reactors, as demonstrated in Figure 1-8 (a), have found applications in photocatalytic synthesis. A notable example is the TiO_2 -catalyzed photochemical coupling between diazoarenes and heterocycles under blue-light irradiation, as explored by Rehm et al. [134]. In their design, the reactor walls were TiO_2 -coated, and nitrogen gas flowed counter-currently to enable self-draining.

Noël et al. designed a packed-bed reactor for TiO_2 -catalyzed synthesis of disulfides under aerobic conditions, illustrated in Figure 1-8 (b) [135]. Their innovative continuous-flow protocol can handle various thiol substrates, producing both homo- and hetero-dimerized disulfides.

2) Continuous-flow fixed-bed reactors for photooxidation of alcohols

For the selective photooxidation of alcohols using immobilized catalysts, continuous-flow microreactors dominate the literature due to their high surface-to-volume ratio, reduced mass transfer restrictions, and optimized illumination conditions, as shown in Figure 1-8 (c) [139].

For instance, Nair et al. engineered a microreactor lined with ZnO nanoparticles for the oxidation of benzyl alcohol into benzaldehyde using a UV-LED light source [136]. The catalyst was coated by an ultrasound-assisted deposition method. Their system showcased impressive benzaldehyde selectivity and superior specific conversion rates compared to conventional batch reactors.

Further, Pradhan et al. reported a microtube reactor, coating its inner walls with TiO₂ for both TiO₂ UV [137] and visible light [138] applications. This apparatus, when used for the selective photocatalytic oxidation of benzyl alcohol, outperformed traditional methods, requiring no additional oxidants and yielding commendable conversion rates and selectivity.

3) PMRs for photocatalytic synthesis

Although some progress has been made in reactors equipped with immobilized catalysts for photocatalytic synthesis, PMRs specifically tailored for this application are still in an early stage [140]. Comprehensive literature reviews have yet to find PMRs where catalysts are directly coated on the membrane where photocatalytic synthesis takes place. Nonetheless, it is worth noting certain PMRs in which the membrane aids in catalyst or product separation, with the reaction zone being distinctly separated.

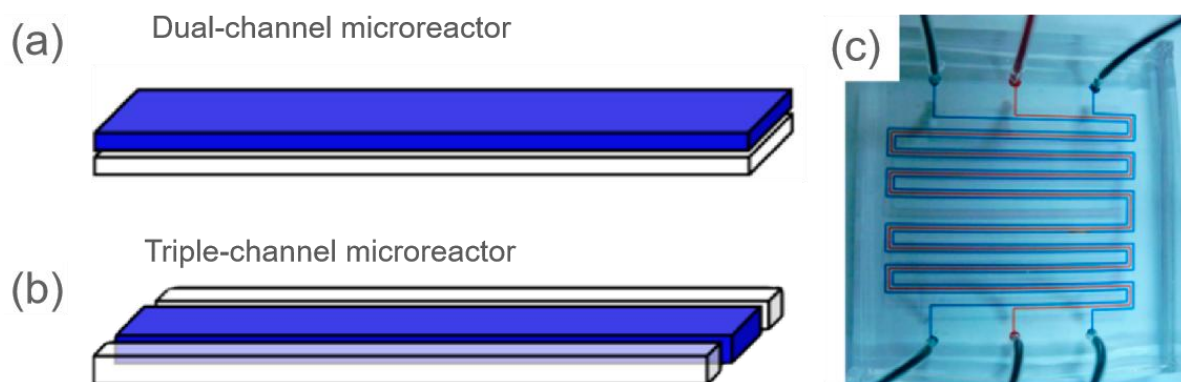


Figure 1-9 Graphical representation of: (a) dual [141] and (b) triple-channel [142] microreactor for photooxidation of allylic alcohol; (c) photograph of the triple-channel microreactor, reaction channel (red) and outer channels (blue) are filled with dye solution for demonstration purposes. Copyright 2011 Park and co-workers.

Molinari et al. delved into the benzene-to-phenol conversion using a hybrid PMR that utilizes suspended TiO₂ [143]. Their system simultaneously achieved phenol production and its separation, limiting the formation of oxidation by-products like benzoquinone, hydroquinone, and other derivatives. Additionally, Molinari et al. leveraged this PMR system for the

photocatalytic hydrogenation of acetophenone into phenylethanol, both under UV and visible light conditions [144]. When comparing the PMR's performance to traditional batch systems, the PMR demonstrated superior conversion and yield. This efficiency can be attributed to the concurrent extraction of phenylethanol into the organic phase, driving the reaction towards product formation.

Although the main focus here is on photocatalytic synthesis with solid catalyst, Park et al.'s unique multi-channel microchannel membrane reactor deserves mention [141, 142]. Illustrated in Figure 1-9, their design uses a membrane to infuse oxygen into the reaction zone, markedly amplifying the biphasic gas-liquid photosensitized oxygenation of allylic alcohols. It's crucial to note that this setup didn't incorporate any immobilized photocatalyst on the membranes. Instead, a photosensitizer, methylene blue, was used alongside a separate oxygen flow within the channels.

1.2.2.3 Development of photocatalytically active coatings

As aforementioned, heterogeneous photosynthesis employing immobilized solid photocatalysts is rare in literature, whereas most applications focus on the photodegradation of pollutants with immobilized catalyst, particularly in PMRs. This section reviews the state-of-the-art methods exclusively for photocatalyst immobilization for photodegradation.

Photocatalysts can be applied to porous membranes or non-porous substrates using numerous deposition techniques, as highlighted in Table 1-1. Traditional methods such as magnetron sputtering, chemical vapor deposition (CVD), dead-end filtration coating, and dip coating face certain challenges, including high energy consumption, the complexity of precursor preparation, or coating non-uniformity.

In contrast, inkjet-printing emerges as a cost-effective and versatile approach, allowing to form a homogeneous layer with precisely controllable catalyst loading and layer thickness, which is a prerequisite for kinetic studies [64, 67, 145]. Previously, Mogalicherla and Lee et al. at IMVT have used inkjet-printing to fabricate alumina layers on stainless steel substrates in microreactors [146]. Recently, this technology has garnered significant interest for its ability to create homogeneous porous layers of photocatalysts, such as TiO_2 [121, 147, 148]. Such photocatalytically active layers can be integrated with filtration membranes to form composite structures, which demonstrate high permeability and are promising for wastewater treatment applications [50]. Despite its potential, research on inkjet-printing of photocatalysts onto membranes remains rare, and comparative analyses of its degradation efficiency against other

techniques are limited.

Table 1-1 Various methods for coating photocatalyst on porous membrane for photodegradation of pollutants

Catalyst	Membrane	Coating method	Ref.
TiO ₂	Al ₂ O ₃	Dip coating	[30]
TiO ₂	TiO ₂ NF layer with Al ₂ O ₃ support	Magnetron sputtering	[23]
TiO ₂	Al ₂ O ₃	CVD	[149]
N-TiO ₂	Al ₂ O ₃	Drop-coating	[110]
TiO ₂	TiO ₂ NF layer with Al ₂ O ₃ support	Inkjet-printing	[64]
TiO ₂	Al ₂ O ₃	Atomic layer deposition (ALD)	[128]
TiO ₂	Polyether sulfone (PES)	Dip coating	[11]
TiO ₂	Porous Stainless Steel	Dead-end filtration	[150]
TiO ₂ -WO ₃	Polyaniline (PANI)	Dead-end filtration	[151]
g-C ₃ N ₄	Polyvinylidene fluoride (PVDF)	Dip coating	[152]

In the field of PMRs for photodegradation, membranes are categorized into polymeric and ceramic types. Polymeric membranes, such as PVDF, are widely used in water treatment and are often employed as substrates for photocatalyst coatings [152, 153]. Nevertheless, these membranes exhibit lower thermal and chemical resistance compared to ceramic membranes [154]. For instance, inkjet-printing operates by dispersing inks - a liquid phase containing solutes or fine particles in a solvent. The coating process normally includes a calcination step to evaporate the solvent in the as-coated layer, which requires the substrate to be thermally stable. Furthermore, the exposure to UV light and the oxidative species produced during PMR applications may compromise the integrity of polymer-based membranes [104]. In contrast, ceramic membranes are distinguished by their robust thermal and chemical stability, making

them preferred substrates for coatings [155]. Yet, they are also inherently more brittle, rendering them susceptible to cracking from mechanical stresses during use - a factor that must be considered carefully.

1.2.3 Kinetic studies

1.2.3.1 Photodegradation

Kinetic studies play a crucial role in understanding the dynamics of photocatalytic pollutant degradation across various reactor systems. Over the past two decades, significant research in this area has been reviewed by Visan and Ateia et al. [62, 156]. Commonly, these studies employ a pseudo-first-order reaction model derived from the Langmuir-Hinshelwood model. However, this approach may oversimplify the process by overlooking the pollutant's adsorption to the catalyst, which can significantly impact kinetics [157]. Additionally, while the apparent reaction rate constant calculated using the Langmuir-Hinshelwood model is a popular metric for assessing reactor performance, it may obscure the distinction between the intrinsic reaction rate and mass transfer rate [158, 159].

In systems with immobilized photocatalysts, kinetic analysis becomes more complex compared to slurry systems. This complexity arises mainly from two factors: the attenuation of light intensity within the catalyst layer and the internal mass transport limitations. These factors, linked with the coating thickness, have received limited attention in existing literature. Ray et al. [67, 160-162] specifically addressed these issues in their kinetic studies of a semi-batch swirl-flow reactor with immobilized catalysts, developing models that factor in layer thickness, mass transport, and light decay. Similar considerations have been applied in studies of continuous-flow microreactors with immobilized photocatalysts [63, 163, 164], which examine both internal and external mass transport limitations.

Kinetic studies also extend to PMRs with immobilized catalysts. For instance, Phan et al. developed a quantitative model for MB photodegradation in a dead-end flow system, incorporating mass transfer and intrinsic reaction rates [106]. This model also integrated a Beer-Lambert law-based light model to account for light intensity decay within the catalyst layer, while highlighting the substantial role of external mass transfer in the overall reaction rate.

Additionally, Deba et al. conducted simulative studies for a dead-end flow PMR for MB degradation [28], proposing a simple 1D model that considers the synergistic effects of membrane filtration and photodegradation. Their model suggests that membrane rejection

significantly aids pollutant degradation, especially with slower reactions. However, their findings lack experimental validation.

It is also important to note that many kinetic studies on photodegradation do not always incorporate light-related factors. These include not only light decay due to scattering within the catalyst layer but also the non-uniformity of illumination, particularly when using overhead lamps that may light non-reactive areas of the reactor. This scenario can reduce light utilization efficiency and poses challenges for kinetic studies and reactor modeling. Potential optimization strategies include using micro-LED arrays [113, 165] or optical fibers with lenses to evenly distribute light over the reactive area.

There remains a gap in validating models across different reactor systems to demonstrate their universal applicability. Reporting and comparing photocatalytic performances between various systems should consider defined experimental conditions, including the catalyst, model pollutant, light type, and intensity [166, 167].

Given these considerations, there is an increased need for developing reactor systems operating under well-defined conditions. Such systems are essential for more accurate kinetic studies, leading to a deeper understanding of the photocatalytic processes involved.

1.2.3.2 Photooxidation of alcohols

Despite being less prevalent than studies on pollutant photodegradation, the kinetic study of alcohol photooxidation, particularly within heterogeneous catalysis, has garnered notable attention.

The study by Giannakoudakis et al. investigates the photocatalytic oxidation of benzyl alcohol to benzaldehyde using various titanium oxide catalysts in a slurry reactor [168]. The research focuses on the mechanistic and kinetic aspects of this reaction, utilizing different light sources and scavenger tests to understand the involved reactive oxygen species and reaction mechanisms. The study reveals that the photocatalytic activity and selectivity towards benzaldehyde are influenced by the physical and chemical properties of the catalysts.

Giacco et al. offered a mechanistic and kinetic exploration of the photooxidation of benzylic alcohols [169]. The research determines the quantum yields related to this photo-oxidation process. A Langmuir-Hinshelwood isotherm treatment was employed to understand the reaction kinetics and mechanisms, particularly the electron transfer and benzylic deprotonation rate constants. This study offers significant insights into the influence of substrate structure on

the reactivity and kinetics of photo-oxidation in heterogeneous catalysis.

Estahbanati et al. examined the selective photocatalytic oxidation of cyclohexanol to cyclohexanone using TiO_2 -based photocatalysts [170]. Their study employed in situ attenuated total reflectance - Fourier transform infrared spectroscopy (ATR-FTIR) analysis and developed a kinetic model to predict cyclohexanone production rates. The research revealed high selectivity of cyclohexanone formation without significant production of carbonates and carboxylates.

Based on extensive literature review, researches on the photooxidation of alcohols have been conducted using slurry reactors. However, studies focusing on immobilized catalysts, especially on PMRs for alcohol oxidation, are notably scarce and warrant further investigation.

1.3 Objectives of this dissertation

The primary objective of this research is the development of a μ PMR, operational under well-defined conditions, and its application in two key fields: photodegradation of pollutants in water and selective photooxidation of alcohols. The structure of the dissertation is illustrated in Figure 1-10.

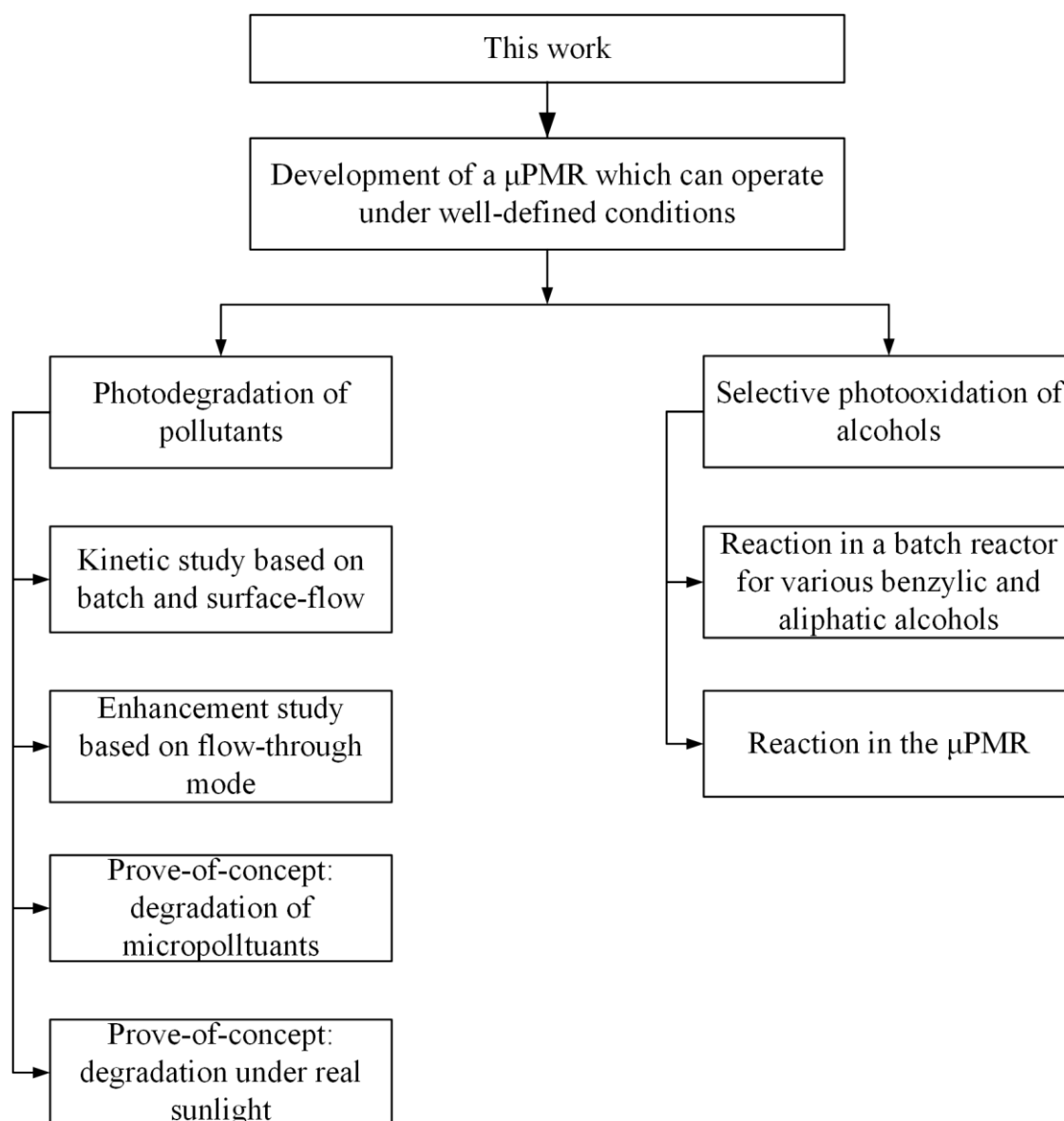


Figure 1-10 Structure of this dissertation

Initially, the μ PMR was developed with a novel design of the optical part, incorporating optical fibers to achieve homogeneous light illumination on the reaction zone. Significant emphasis was placed on the development of catalytically active coatings with precisely controllable loading and thickness of the catalyst layer by employing a novel coating technique inkjet-printing. The core of this coating technique is the formulation of inks for various photocatalysts.

For the photodegradation of pollutants, TiO_2 -based catalysts were selected, while C_3N_4 -based catalysts were chosen for the photooxidation of alcohols.

In its application to photodegradation, the μPMR was first employed in the degradation of a model dye pollutant, Rhodamine B (RhB). A detailed kinetic study was conducted, adopting the Langmuir–Hinshelwood kinetic model. This study accounted for the intrinsic reaction kinetics, alongside external and internal mass transport considerations. Furthermore, the μPMR 's capabilities were extended to analyze the enhancement of RhB photodegradation under UV light. This included variations in flow modes, specifically examining the synergistic effects of membrane filtration and photocatalysis, and the impact of light intensity on the photodegradation process. Moreover, the μPMR was instrumental in photodegrading three pharmaceutical micropollutants - Carbamazepine (CBZ), Sulfamethoxazole (SMX), and Bezafibrate (BZF) - under both UV and visible light. Degradation using real sunlight was also part of this work.

For the task of photooxidation of alcohols, a carbon-nanodot-doped C_3N_4 (CD- C_3N_4) catalyst was developed and formulated for the inkjet-printing of the reactive coating. This catalyst was initially tested in a batch reactor for the oxidation of various benzylic and aliphatic alcohols. Subsequently, benzyl alcohol was chosen as a model substrate for further oxidation studies to benzaldehyde using the μPMR .

The development of the μPMR as well as the catalyst coating is elaborated in Chapter 0 of this thesis. Chapter 0 is dedicated to the comprehensive study of the photodegradation of pollutants, while Chapter 0 delves into the study on photooxidation of alcohols.

Selected results presented in this work have been adapted from prior publications [50, 64], with additional data and analysis expanded for this thesis.

2. Experimental procedures and characterization

2.1 Microstructured photocatalytic membrane reactor (μ PMR)

2.1.1 Development of the μ PMR

A major task of this work is the development of a μ PMR, which enables continuous-flow operation under well-defined conditions. As shown in Figure 2-1, the reactor consists of two main components: the reactor body and the optical part.

2.1.1.1 Reactor body

The reactor body features two microchannels, each having identical dimensions: 100 mm in length, 5 mm in width, and 0.3 mm in depth. The upper microchannel is fabricated within the PTFE membrane holder, while the lower microchannel is constructed within the metallic reactor body. O-rings seal the reactor, with an epoxy sealant being applied at the contact area between the membrane and the PTFE holder (shown in Figure A 1).

This μ PMR is designed to accommodate various membrane types, including both ceramic and polymeric. For membranes too thin for the holder, a porous support is required (refer to Figure A 1). Polymeric membranes, though common in water treatment, are less suitable for catalytic coatings due to their lower chemical and thermal resistance [171]. Therefore, considering inkjet-printing requires calcination to eliminate organic additives after printing, ceramic membranes were chosen for this work.

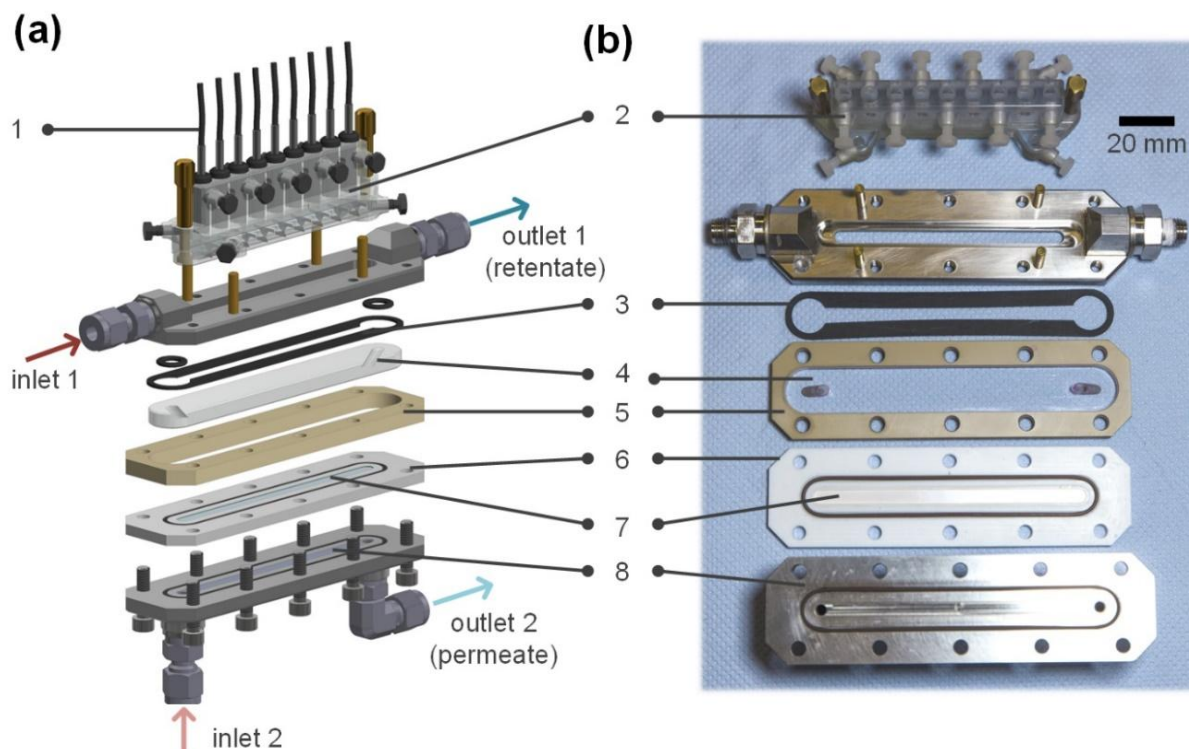


Figure 2-1 Illustration of the μ PMR: (a) CAD structure; (b) picture of the components: 1. optical fiber; 2. 3D printed fiber holder; 3. O-ring for sealing; 4. quartz glass; 5. polyetheretherketone (PEEK) frame for the quartz glass; 6. polytetrafluoroethylene (PTFE) membrane holder; 7. photocatalyst-coated membrane; 8. metallic reactor body with a microchannel for permeate or gas flow. [50]

2.1.1.2 Optics

Figure 2-2 shows the optical setup of the reactor, comprising nine optical fibers (numerical aperture = 0.63, core diameter 1 mm, Prizmatix) that channel light from a high-power LED source (Prizmatix) into the reactor. These fibers are split from three main fibers, each connected directly to the light source, and are precisely positioned using a 3D-printed polymeric holder (material: Veroclear, Stratasys) secured by polyvinyl chloride (PVC) screws. The light is focused through cylindrical lenses made of quartz glass (H-K9L, Worldhawk), ensuring that the illumination area precisely aligns with the microchannel area, thus optimizing photonic energy utilization. Additionally, the upper microchannel is covered by a quartz plate featuring two cylindrical oblique holes for inlet and outlet flow. The configuration allows for precise tuning of light intensity from 0 to 2 mW cm^{-2} , accommodating both UV (365 nm) and visible light (white light). The spectrum of both light types is shown in Figure A 2.

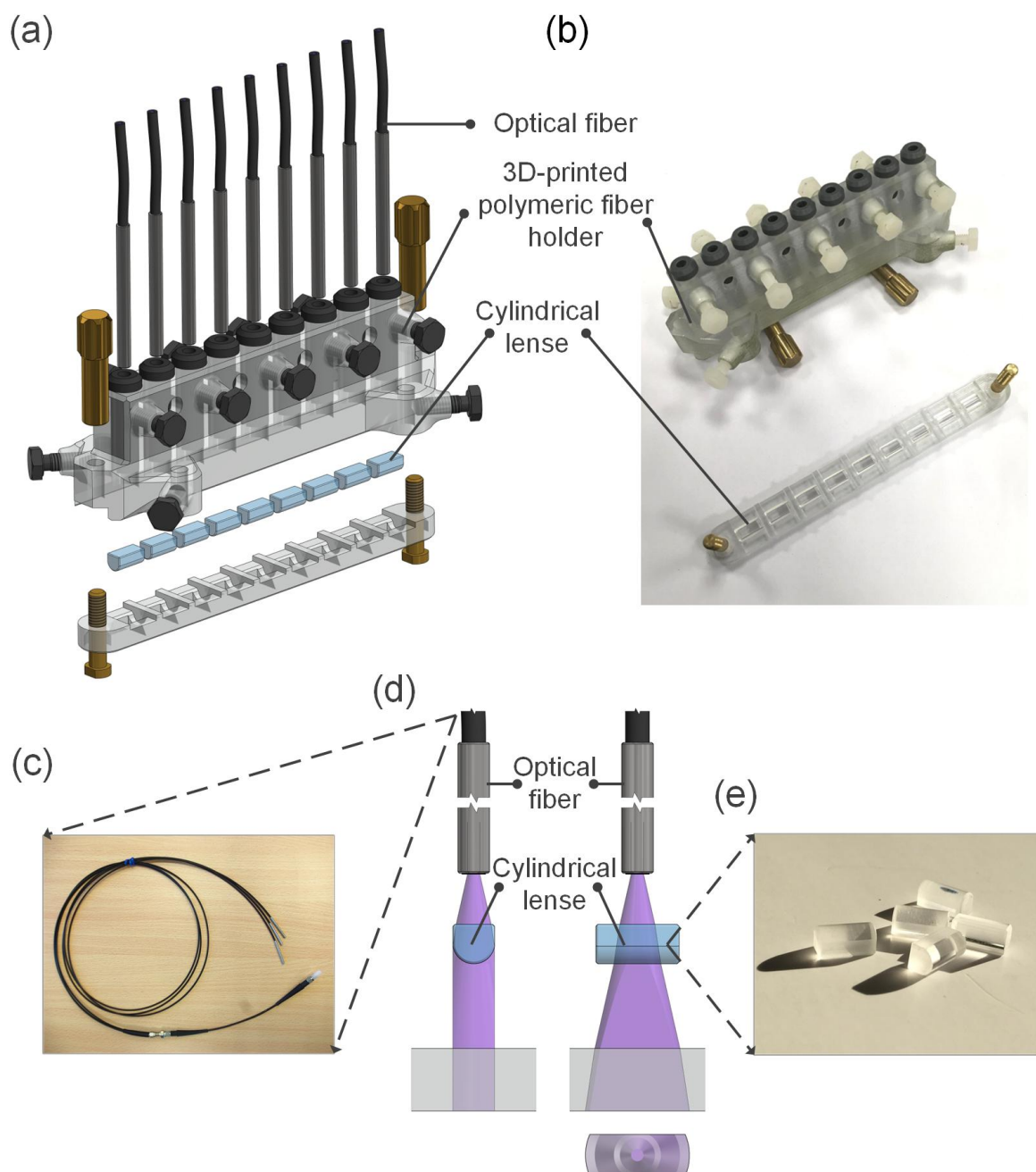


Figure 2-2 Optical part: (a) CAD schematic; (b) picture of the 3D-printed polymeric fiber holder and lens holder; (c) picture of the optical fiber; (d) illustration of the light path from the fiber to the channel via the lens; (e) quartz cylindrical lenses. [64]

2.1.2 Continuous-flow system

The μ PMR was integrated into a continuous-flow system, as depicted in Figure 2-3 and Figure 2-4. This system features a high-precision high performance liquid chromatography (HPLC) pump from Knauer for efficient liquid solution delivery to the μ PMR. Gas flow to the feed bottle, for saturating the feed solution or to the lower microchannel, is regulated by a mass flow controller (MFC, MKS Instruments), depending on the chosen flow mode. Pressure within the

upper microchannel of the μ PMR is maintained using a precision back pressure regulator (BPR 1, U3L series, Equilibar) coupled with a nitrogen pressurization system from Air Liquide Deutschland GmbH. Additionally, another back pressure regulator (BPR2, Swagelok) manages the gas pressure in the lower microchannel. Light intensity measurements were averaged from 18 points beneath the reactor's quartz glass using an irradiation meter TM213 (Tenmars) for UV light and a solar power meter TES1333 (TES) for visible light.

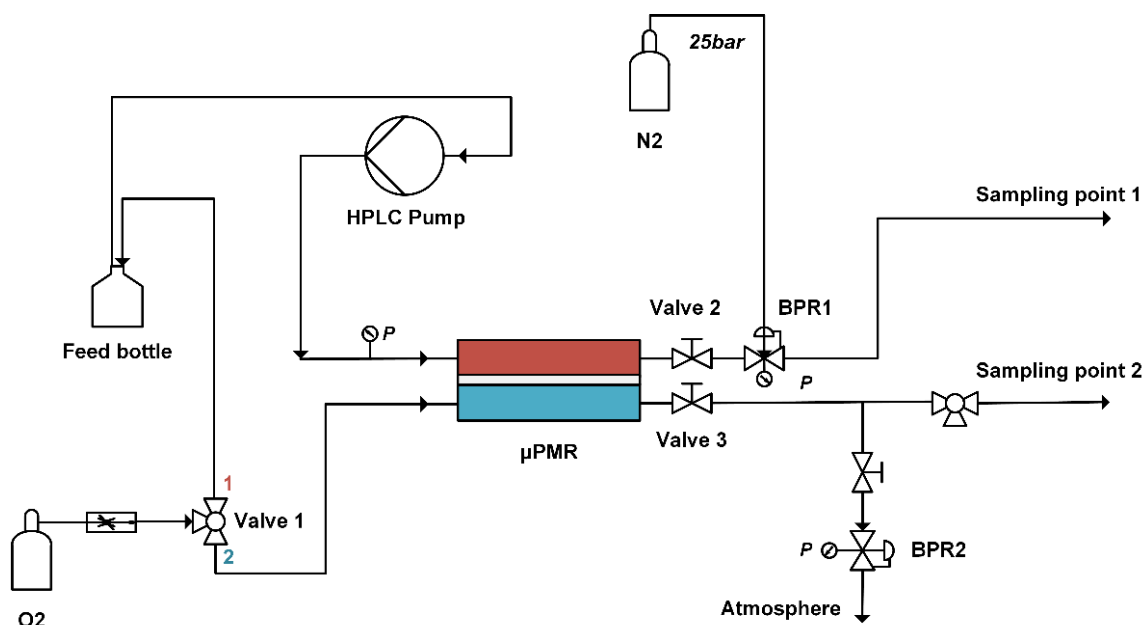


Figure 2-3 Flow chart of the continuous-flow μ PMR system. [50]

The continuous-flow μ PMR system's versatility is highlighted by its ability to operate under four distinct flow modes:

- Mode 1: Mixed flow-through and surface-flow contactor, where the feed solution flows through and above the membrane, which is a cross-flow setup (see Figure 1-6 (a)).
- Mode 2: Pure surface-flow contactor with built-in oxygen distributor, utilizing the membrane for direct gas distribution to the catalyst-coated membrane across the entire reaction zone, in order to intensify the reaction, as illustrated in Figure 1-6 (b).
- Mode 3: Nanofiltration mode, employing uncoated NF membranes in a cross-flow configuration without light for comparative analysis in pollutant rejection studies.
- Mode 4: Pure surface-flow mode, where the feed liquid flows over the membrane surface without permeating, a common approach in photocatalytic microchannel reactors, as discussed in Chapter 1.2.2.

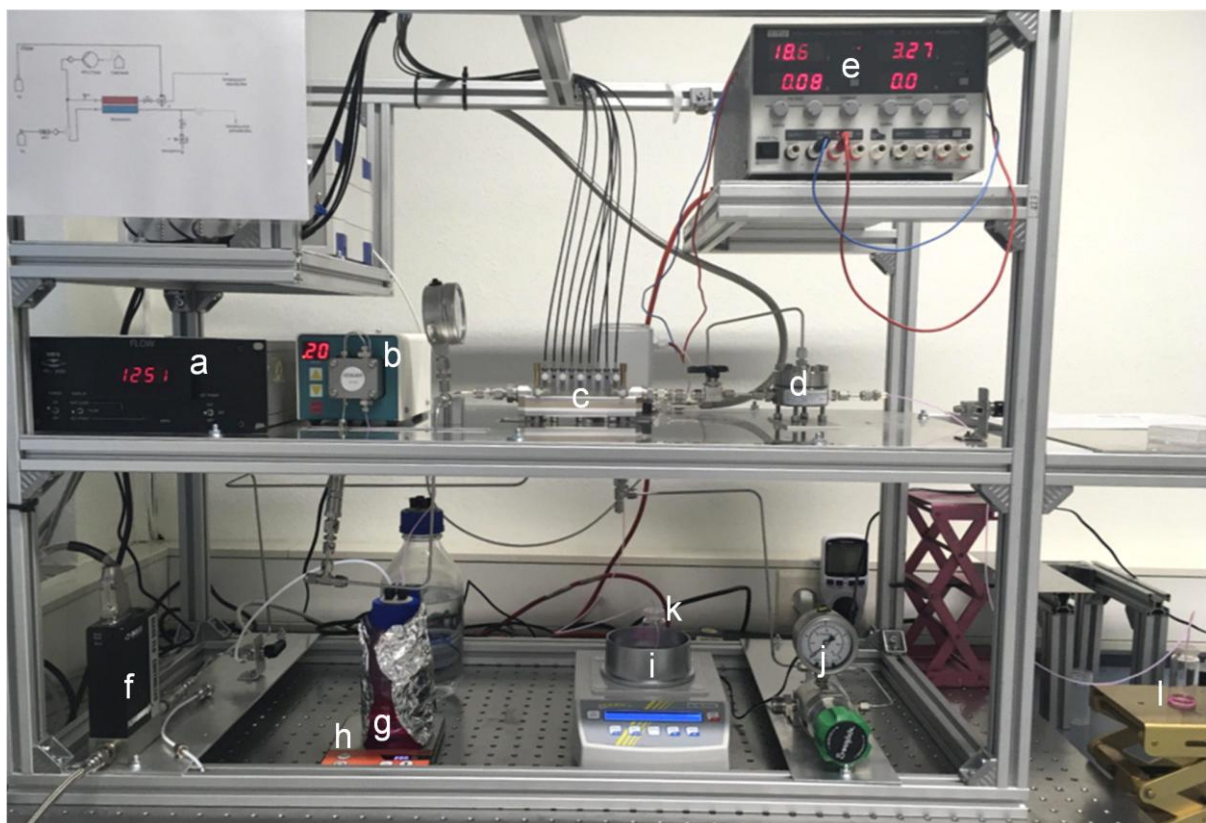


Figure 2-4 Picture of the continuous-flow μ PMR system: (a) MFC controller; (b) HPLC pump; (c) μ PMR; (d) BPR1; (e) controller of BPR1; (f) MFC; (g) feed bottle; (h) magnetic stirrer; (i) electronic scale; (j) BPR2; (k) sampling bottle (point 2); (l) sampling bottle (point 1). [50]

2.2 Development of catalytically active coatings

2.2.1 Coatings for photodegradation

2.2.1.1 Preparation of the catalysts

In this work, two types of photocatalysts were used: commercially available TiO_2 (P25) from Evonik, and in-house synthesized Nitrogen-doped TiO_2 (N- TiO_2). Following the methodology described by Cong et al. [172], the synthesis of N- TiO_2 started with the preparation of a microemulsion. For this, 10 mL of cyclohexane (VWR Chemicals) was mixed with 10 μL of Triton X-100 (Sigma-Aldrich) to create the oil phase. In parallel, the aqueous phase was prepared by adding 5.1 g of tetrabutyl titanate (Acros Organics) dropwise to 20 mL of a 5 mol L^{-1} nitric acid solution (Merck). The aqueous phase was then slowly incorporated into the oil phase under constant stirring at 100 rpm. Next, 1.77 g of triethylamine (Fluka), serving as the nitrogen source, was added to the stirred microemulsion. This mixture was then stirred continuously at the same speed for an additional 4.5 hours. The resultant emulsion was then transferred to an 80 mL Teflon-lined stainless-steel autoclave and heated to 120°C at a rate of 5°C min^{-1} , where it was maintained for 13 hours. After cooling to room temperature, the precipitate formed at the bottom of the autoclave was collected, washed thrice with ethanol and deionized water, and dried overnight in a vacuum oven (Vacutherm, Heraeus) to obtain the final N- TiO_2 powder. Both TiO_2 P25 and N- TiO_2 are shown in Figure 2-5.

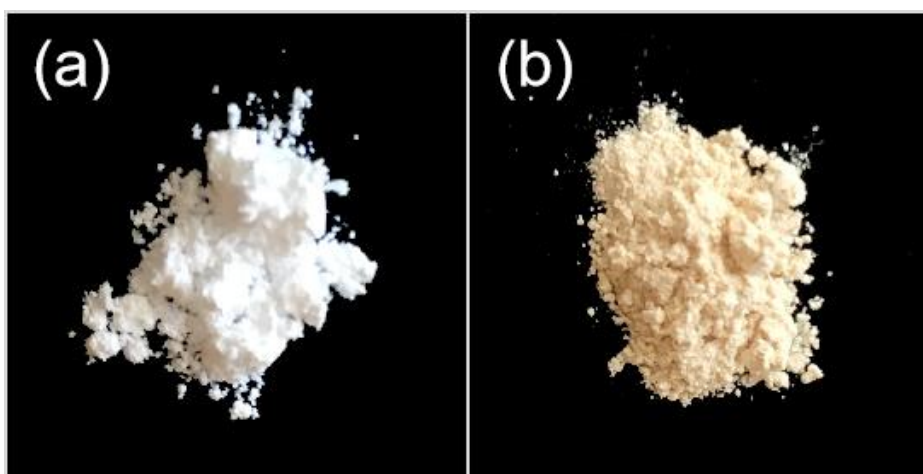


Figure 2-5 Picture of the two catalysts: (a) TiO_2 P25 and (b) N- TiO_2 .

2.2.1.2 Preparation of the ink

Adhering to established protocols in the literature [147, 173], the ink suspension was prepared using TiO_2 powder, a dispersant (Zetasperse 1200, Air Products), an electrolyte ($\text{Na}_4\text{P}_2\text{O}_7$,

Sigma-Aldrich), and two co-solvents (N, N-Dimethylformamide, VWR Chemicals, and PEG-400, Sigma-Aldrich) mixed into deionized water (Milli-Q, Merck). A trace amount of NaOH solution (1 M) was added to adjust the pH. All chemicals, including the electrolyte, co-solvents, and NaOH (analytical grade), were used as received without further purification. The prepared ink underwent ultrasonication (Elmasonic P) at 80 kHz for 20 minutes before printing.

For reproducible printing and to form homogeneous catalyst layers, the following criteria were essential, as summarized from literature [145, 146, 174, 175]: 1) particle size should be less than 1/100 of the nozzle diameter ; 2) the ink suspension must maintain stability to avoid rapid agglomeration and sedimentation; 3) the rheological properties of the suspension, including viscosity, must be optimized to ensure stable ink formation with the printer.

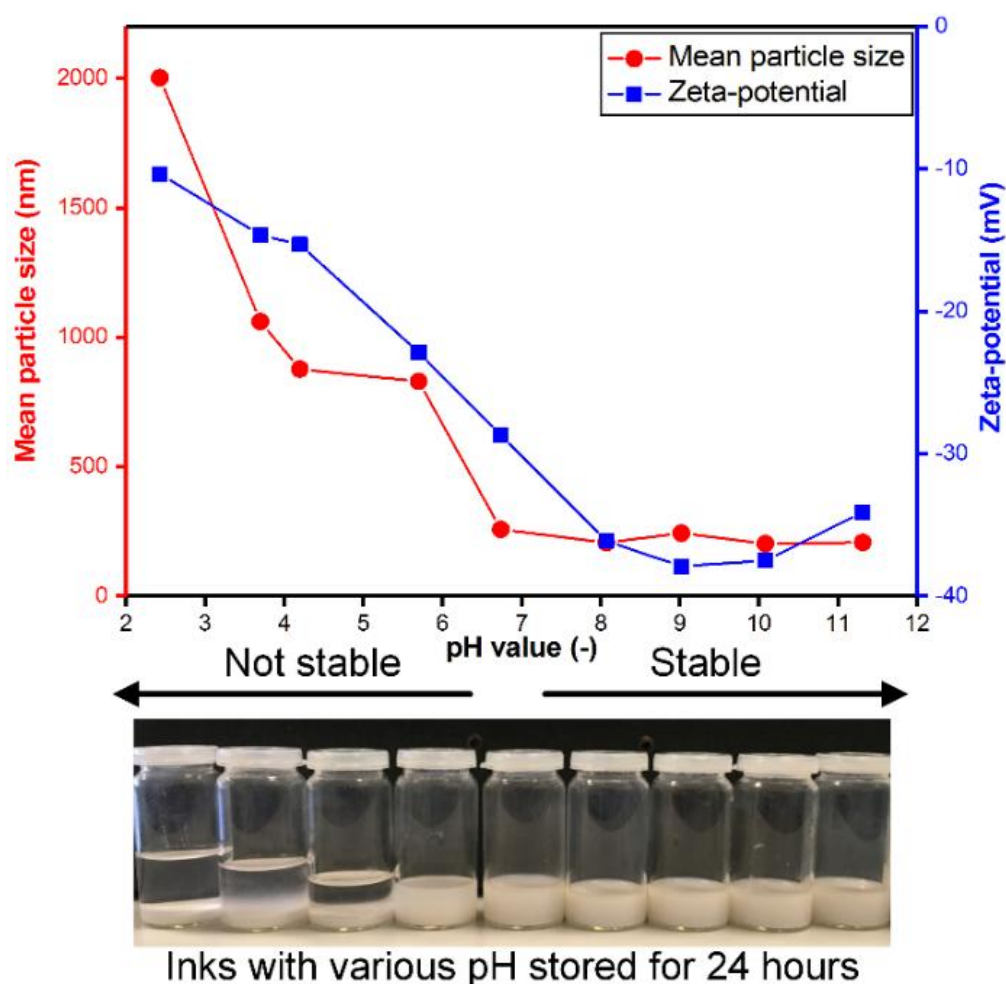


Figure 2-6 Particle size, zeta-potential and pictures of the TiO₂ P25 ink at various pH values. [64]

With a nozzle diameter of 100 μm of the printer used in this study, particle size needed to be under 1 μm . It has to be noted that the particle size measurement must take particle agglomeration into account. Suspension stability, typically gauged by zeta potential, requires

2. Experimental procedures and characterization

values above 30 mV or below -30 mV for effective electrostatic repulsion and agglomeration prevention [147]. pH values can have a critical impact on particle size and zeta potential, which was investigated in this work. Both of these parameters were measured using a Delsa Nano instrument (Beckman Coulter).

As shown in Figure 2-6, the TiO₂ P25 ink suspensions' pH significantly influenced the mean particle size and zeta potential. Higher pH values increased the overall suspension stability, thereby reducing agglomeration and sedimentation. The ideal pH range for optimal ink stability was identified between 8 and 10, with an optimized pH set at 10 (± 0.3).

The investigated ranges and optimum values of each component are summarized in Table 2-1. The viscosity of the optimized inks, measured at 1.60 mPa s at a shear rate of 100 s⁻¹ (HAAKE RheoStress 1, Thermo Scientific), falls within the recommended range of 0.4 - 100 mPa s for the nozzle. The ink density for both catalysts was measured at 1.07 g mL⁻¹.

Table 2-1 Composition of the TiO₂ ink for inkjet-printing [64]

Material	Function	Investigated range	Optimum Value
TiO ₂	Catalyst	0.1 – 1.0 wt.%	0.5 wt.%
Water	Main solvent	/	88.5 wt.%
Zetasperse 1200	Surfactant	0.5 - 4.0 wt.%	2 wt.%
Na ₄ P ₂ O ₇	Electrolyte	/	5×10 ⁻⁴ M
PEG 400	Co-solvent	5 – 10 wt.%	7 wt.%
DMF	Drying and surface tension control	0.5 - 5.0 wt.%	2 wt.%
NaOH	Adjusting pH	/	10 (± 0.3)

Note that the co-solvent and polymer functioned as humectants, slowing down water evaporation at the nozzle tip and promoting quick rehydration of the ink. Additionally, these co-solvents served as viscosity modifiers, effectively preventing air ingestion issues at the nozzle, which is crucial for stable droplet formation during extended periods of operation.

2.2.1.3 Development of the coatings

An Autodrop Compact (Microdrop Technologies) drop-on-demand inkjet-printer was used for printing. Ink droplets were created by piezoelectric impulses from the dispenser head, with the voltage and pulse length tuned for stable droplet formation, as monitored by a high-speed CCD camera (see Figure 2-7 (a)).

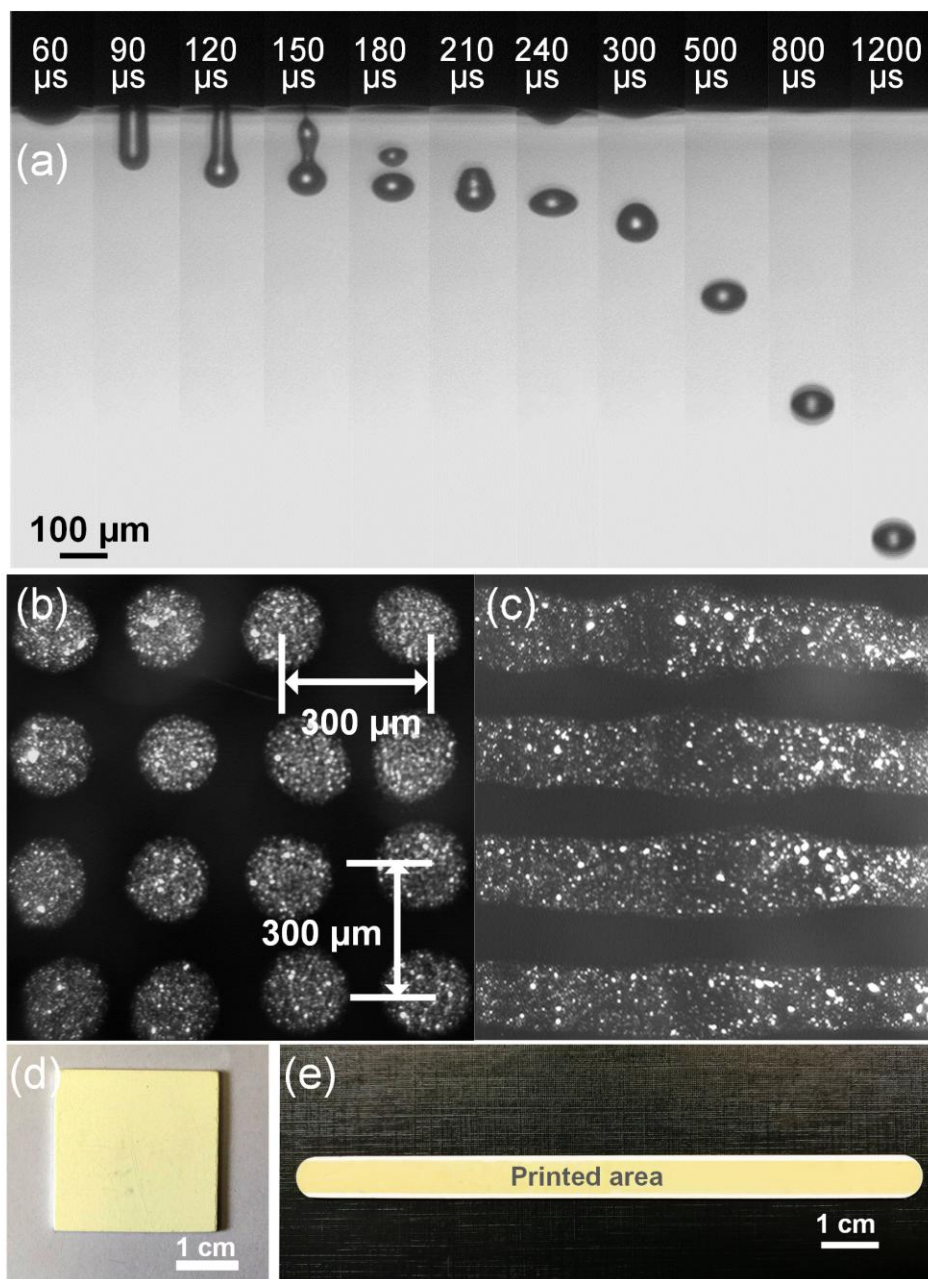


Figure 2-7 (a) Illustration of droplet generated from the nozzle at different time intervals from the pulse start; (b) ink drops on the substrate with variation of the drop distance $i_x = 300 \mu\text{m}$ and $i_y = 300 \mu\text{m}$ in x and y direction; (c) ink drops on the substrate with $i_x = 130 \mu\text{m}$, $i_y = 300 \mu\text{m}$; (d) 2.5 cm \times 2.5 cm square substrate printed by 9 layer of the catalyst; (e) 10.8 cm \times 0.8 cm substrate with a rectangular printed area of 0.6 cm \times 10 cm printed by 9 layer of the catalyst.

After stable droplet formation ensured, the pulse voltage and length can be further fine-tuned to adjust the size of the droplets [145]. Figure 2-8 exemplifies how these parameters affect the droplet size for the developed ink. Generally, higher actuation energy leads to larger droplets due to more ink being drawn from the nozzle, with the droplet diameter increasing correspondingly with the voltage. For this study, a pulse voltage of 41 V and a pulse length of 40 μs were selected for printing both P25 and N-TiO₂ inks, resulting in a droplet size of 83 μm , as measured by the CCD camera.

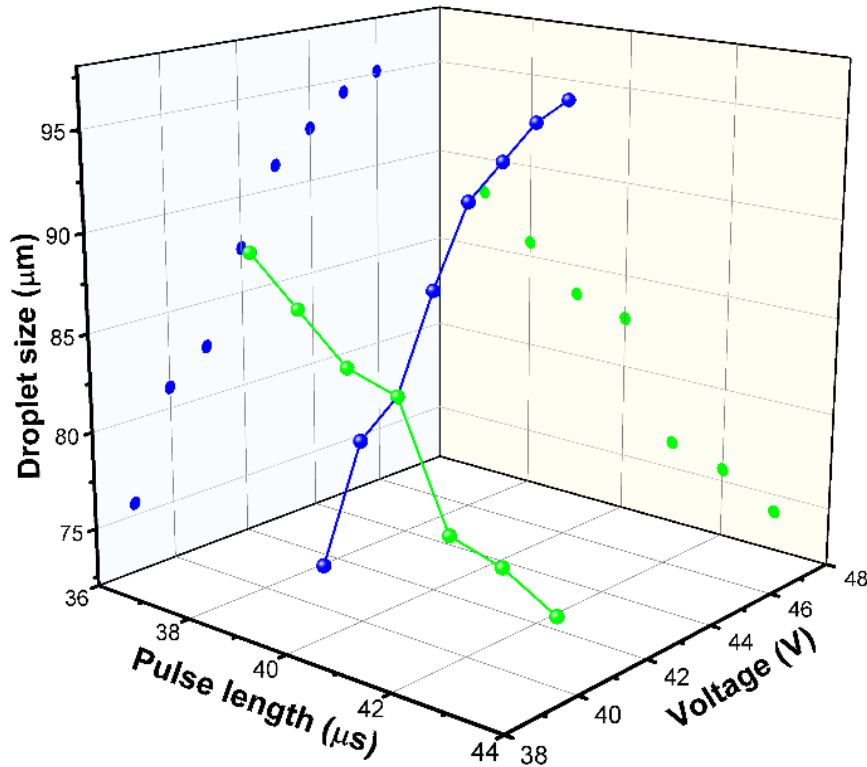


Figure 2-8 Droplet size change with variation of pulse length and voltage. [64]

By knowing the droplet size, the loaded mass of the TiO₂ printed on a certain area can be calculated by:

$$g_{\text{cat}} = N_L \cdot \frac{l_x}{i_x} \cdot \frac{l_y}{i_y} \cdot \frac{4}{3} \pi \left(\frac{d}{2}\right)^3 \cdot \rho_{\text{ink}} \cdot C_{\text{ink}} \quad (2-1)$$

where N_L is the total number of printed layers, l_x and l_y is the length of the printing area in x- and y-direction, i_x and i_y is the distance between two droplets in x- and y-direction as set in the printer (as shown in Figure 2-7 (b, c)), d is the droplet diameter, ρ_{ink} is ink density (1.07 g mL⁻¹) and C_{ink} represents the catalyst concentration of the ink suspension (0.5 wt.%).

The ink suspension was coated layer-by-layer on the 1mm thick ceramic NF membranes (Inopor). No drying was applied between the printing of each layer, as water, the main solvent,

either evaporated rapidly or was absorbed by the porous NF membrane. Three types of ceramic NF membranes, differing in molecular weight cut-off (MWCO) values as provided by Inopor, were used: Membrane 1 (200 Da MWCO), Membrane 2 (450 Da MWCO), and Membrane 3 (750 Da MWCO). Each membrane consisted of a microporous TiO_2 NF surface layer supported by meso- and macroporous Al_2O_3 layers [23]. Membranes of two sizes were employed: rectangular ones ($2.5 \text{ cm} \times 2.5 \text{ cm}$) for batch experiments, and longer ones ($10.8 \text{ cm} \times 0.8 \text{ cm}$) for μPMR experiments, as shown in Figure 2-7 (d, e).

Post-coating, the membranes were calcined at 250°C (2°C min^{-1} ramp rate) in a Heraeus muffle oven to remove solvents and additives, while enhancing coating adhesion. This temperature was set based on thermogravimetric analysis (TGA, Setsys Evolution 16/18, Setaram) and by evaluating RhB degradation in a batch reactor under UV light using coated substrates calcined at various temperatures (procedures detailed in Chapter 2.3.1.2). 250°C ensures complete removal of ink additives and had the highest photocatalytic removal performance [64]. During both batch and μPMR experiments, the coatings showed no signs of peeling off or defects.

For the $2.5 \text{ cm} \times 2.5 \text{ cm}$ substrates, setting the droplet distance to $105 \mu\text{m}$ yielded a per-layer catalyst loading of 0.09 mg (Eq. (2-1)). Although direct comparison of calculated and actual printed layer mass was challenging since the value of the mass per layer is considerably low, droplet size consistency before and after printing indicated precise control of the loaded mass. This precision in mass loading control was also corroborated by a previous study at IMVT using the same inkjet-printing device for Al_2O_3 [145].

2.2.1.4 Characterization method

In order to establish a comprehensive understanding of the catalyst coatings' properties and lay the groundwork for subsequent kinetic studies, a series of characterizations were performed on both TiO_2 P25 and N- TiO_2 catalysts and their respective coatings.

Characterization of catalyst powder:

- Diffuse Reflectance Spectroscopy (DRS): the optical properties of the pristine catalysts were analyzed using a Lambda 650 instrument (PerkinElmer). Spectra were recorded in the range of 250 to 650 nm, employing a scan speed of 0.5 s nm^{-1} .
- X-Ray Diffraction (XRD): structural properties were examined post-calcination at 250°C for the catalyst powders, utilizing a Bruker D8 Advance X-ray diffractometer with $\text{Cu K}\alpha$ radiation at 40 kV and 40 mA. Diffraction data were captured in the 2θ range from 20 to

60°, with a scanning rate of 4° per minute.

- Nitrogen Physisorption: surface area measurements were conducted at 77 K using a Micromeritics 3Flex Surface Characterization Analyzer. Pristine and catalyst samples calcined at 250°C, underwent degassing at 343 K for 8 hours in a SmartVac Prep system (Micromeritics), with specific surface areas determined via the Brunauer–Emmett–Teller (BET) method.

Characterization of catalyst coating:

- Scanning Electron Microscopy (SEM): morphological analysis of the calcined printed layers was performed using a JSM 6300 instrument (JEOL), applying a 10 kV electron beam.
- X-Ray Photoelectron Spectroscopy (XPS): chemical composition and states were assessed using a Scienta 4000 (Al K α line) instrument.
- Optical Profiling: both 2D and 3D surface maps of the printed layers were acquired with an S-neox 3D optical profiler (Sensofar) in confocal mode. The layer thickness was determined from the topological data (detailed in Appendix B1).
- UV-Vis Spectrophotometry: the UV light transmission (TL %) of the coating, ranging from 1 to 9 layers on quartz glass, was measured using an HP 8453 spectrophotometer for the TiO₂ P25 coating. Measurements were conducted at 365 nm wavelength with the quartz glass immersed in a RhB solution within a quartz cuvette. Transmission data were normalized against a blank test using identical quartz glass without coating (refer to Appendix 02 for details).

2.2.1.5 Characterization results

The DRS spectra depicted in Figure 2-9 (a) show that P25 does not absorb visible light ($\lambda > 400$ nm), whereas N-TiO₂ exhibits visible light absorption, consistent with their respective colorations: N-TiO₂ is yellowish and P25 is white. The band gaps, calculated using the Kubelka-Munk function, were determined to be 2.96 eV for N-TiO₂ and 3.16 eV for P25, with the latter aligning with previously reported values [176, 177]. In contrast, the reported band gaps for N-TiO₂ vary widely, ranging from 2.5 to 3.0 eV, as influenced by different catalyst preparation methods [4, 172]. XPS analysis further investigated the state of nitrogen atoms within the TiO₂, scanning the N1s region of N-TiO₂. Figure 2-9 (b) suggests a narrower band gap and the

presence of substitutional nitrogen in the TiO_2 lattice, indicated by a binding energy of 396.8 eV of the Ti-N bond. The peak near 400 eV likely corresponds to interstitial nitrogen interacting with both Ti and O centers [178].

Figure 2-9 (c) presents XRD patterns of both catalysts post-calcination at 250 °C. N-TiO₂ shows an exclusively anatase phase, while P25 displays both anatase and rutile phases. Using the Reference Intensity Ratio (RIR) method [179], the phase composition of TiO₂ P25 was quantified as 83% anatase and 17% rutile, consistent with known compositions for this product [180, 181]. This confirms that the calcination process did not alter the crystalline phases of the coatings.

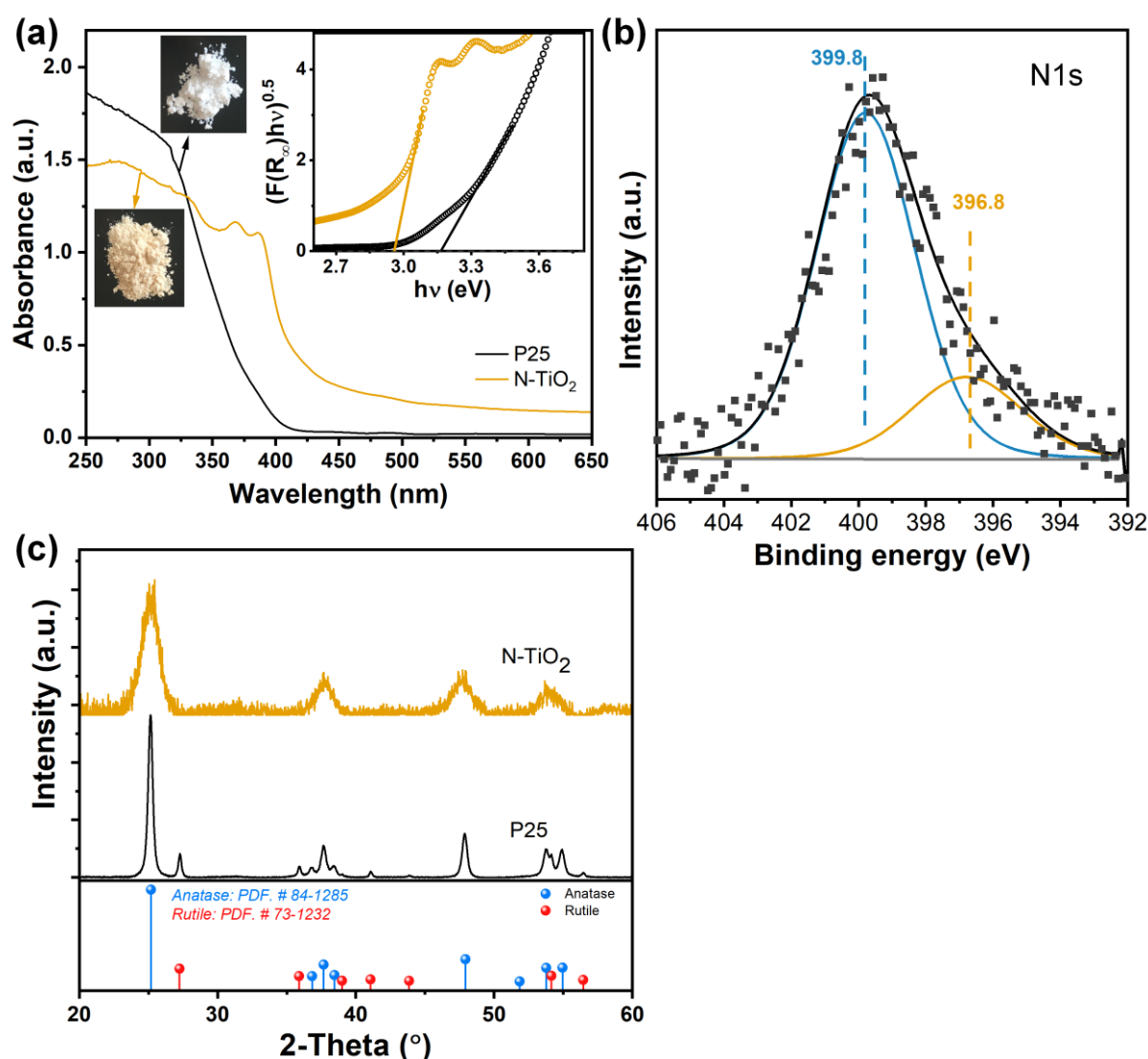


Figure 2-9 (a) DRS spectra with inset showing the transformed Kubelka-Munk curve for determining the bandgaps of the pristine catalysts; (b) XPS spectra of the N 1s region for the N-TiO₂ coating; (c) XRD pattern of the catalyst powder after calcination at 250 °C. [50]

Figure 2-10 illustrates that the inkjet-printed TiO₂ layer is notably porous, with particles

exhibiting slight agglomeration but not forming larger sintered aggregates, a phenomenon also observed in other studies [173]. This figure also distinctly shows that N-TiO₂ particles are smaller in size compared to P25. Smaller particles increase the specific surface area, thus offering more active sites, which is beneficial for catalysis. BET surface area measurements via N₂ physisorption analysis revealed that calcined N-TiO₂ has a significantly larger surface area of 258 m² g⁻¹, which is fivefold greater than P25's 50 m² g⁻¹. Notably, the surface area of N-TiO₂ exceeds the typical range for most TiO₂-based photocatalysts in literature, which is usually below 200 m² g⁻¹ [3, 182-184], while the pristine N-TiO₂ powder shows an even higher surface area of 316 m² g⁻¹. Consistent results across various batches of N-TiO₂ in this study suggest that the adopted synthesis method is effective for producing visible-light-active TiO₂ with enhanced surface areas, holding promise for future applications.

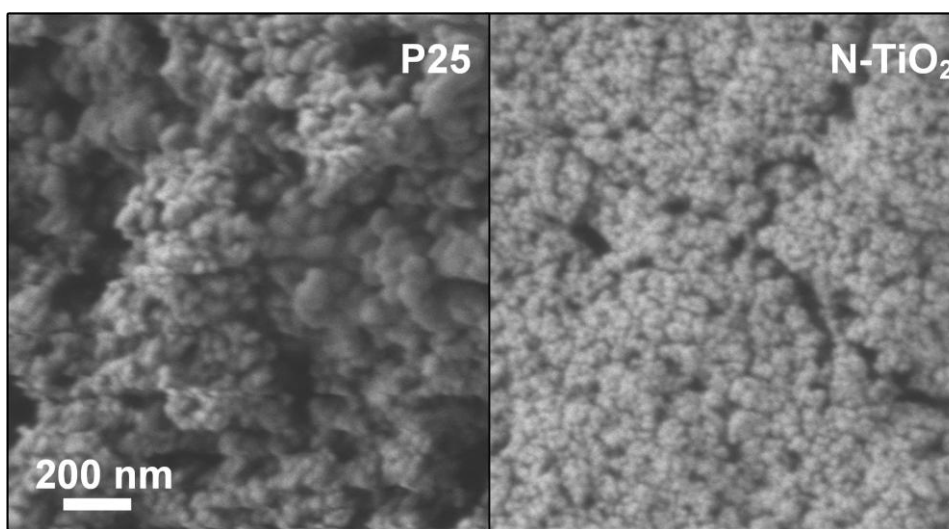


Figure 2-10 SEM picture of the TiO₂ coatings. [50]

Figure 2-11 exemplifies the surface characterization of a nine-layer TiO₂ P25 coating, demonstrating its significant roughness compared to the substrate. As shown in Figure 2-11 (b), the SEM cross-sectional image reveals a coating thickness varying between 0.72 and 1.42 μm in the examined area. Given the non-uniformity in thickness, optical profilometry was utilized to ascertain the average thickness over a larger area, approximately 0.1 – 0.3 mm². For enhanced contrast and more reliable thickness measurement in confocal mode, glass substrates were used in this analysis. The resultant 3D morphology, depicted in Figure 2-11 (c), displays the coating's topography.

Furthermore, as illustrated in Figure 2-11 (d), a clear linear relationship between the mean layer thickness and the number of printed layers indicates effective control over the layer thickness achieved through inkjet-printing. The slope of this relationship suggests an average thickness

of about 110 nm per layer. The surface's RMS roughness is measured at 0.6 μm , corroborating the observed local non-uniformity in thickness.

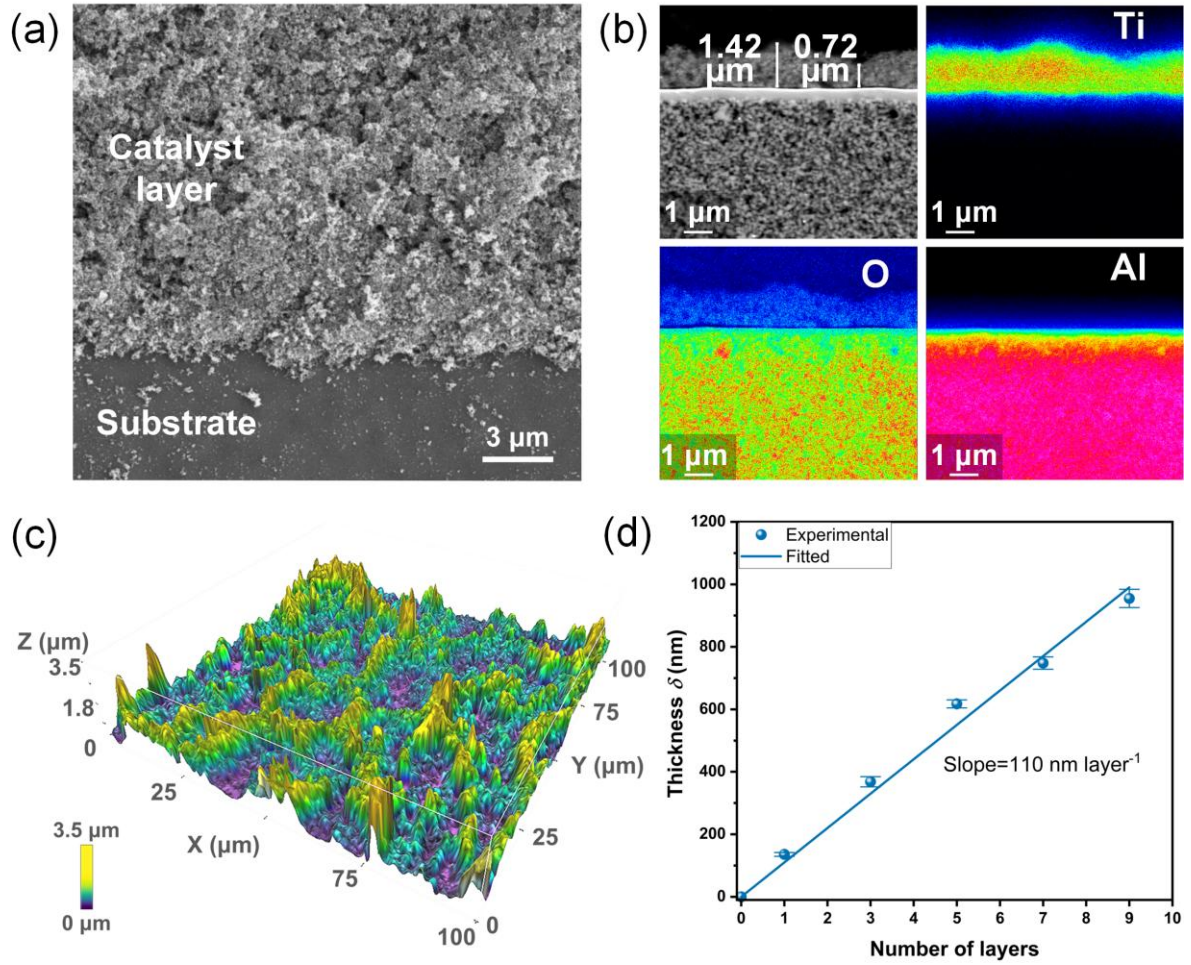


Figure 2-11 Characterization of the 9-layered TiO_2 P25 coating after calcination at 250 $^{\circ}\text{C}$: (a) top-view SEM image of the catalyst layer; (b) cross-sectional view of the coating and element distribution map (from blue to red: increasing signal intensity); (c) 3D morphology of the coating; (d) layer thickness as a function of the number of layers (data given are mean values of $n \geq 3$ replicates, error bar: standard error of the mean). [64]

For kinetic study applications, the porosity of the layer was calculated using the formula:

$$\varepsilon = 1 - \frac{g_{\text{cat}}}{\rho_b \delta_L A_{\text{cat}}} \quad (2-2)$$

where g_{cat} is the catalyst mass for the given layer thickness δ_L according to Eq. (2-1), ρ_b is the bulk density of TiO_2 and A_{cat} is the area of the coating. Taken TiO_2 P25 as an example, its bulk density is 4.26 g cm^{-3} (from manufacturer). The porosity of its coating was calculated to be 0.69, which aligns perfectly with literature values for TiO_2 P25 thin films prepared by doctor blading [185]. The density of the coated thin film can be calculated with Eq. (2-3) by knowing g_{cat} , δ_L and A_{cat} , which yields 1.31 g cm^{-3} for TiO_2 P25.

$$\rho_{cat} = \frac{g_{cat}}{\delta_L A_{cat}} \quad (2-3)$$

2.2.2 Coatings for selective photooxidation

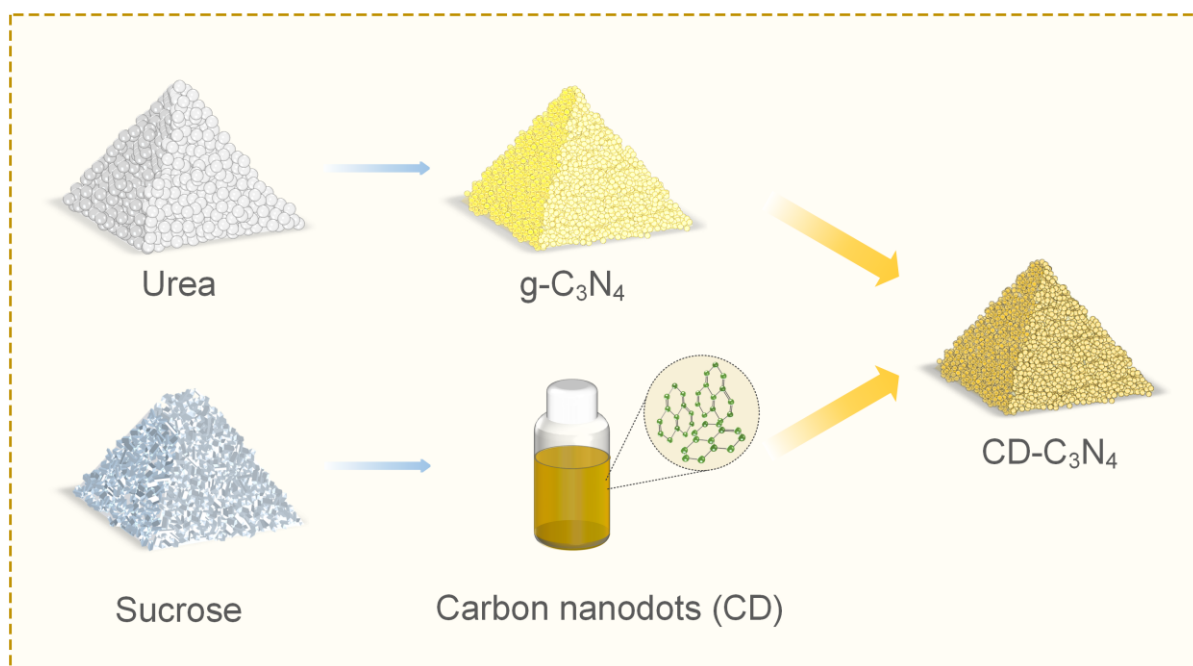
2.2.2.1 Preparation of the catalysts

Graphitic carbon nitride (g-C₃N₄) was employed as the catalyst for photooxidation research. g-C₃N₄ is typically synthesized through various methods, including the pyrolysis of urea or other nitrogen-rich precursors, or through the exfoliation of bulk materials [186]. For the synthesis of carbon-nanodot-doped g-C₃N₄ (CD-C₃N₄) in this work, the procedure outlined by Zhang et al. [187] was followed, as detailed in Figure 2-12.

The synthesis began with the calcination of 10 g of urea (Sigma-Aldrich) at 600 °C for 4 hours with a ramp rate of 5 °C min⁻¹. This method, adapted from Tang et al. [188], resulted in the formation of a yellowish g-C₃N₄ powder upon cooling to room temperature.

Next, the carbon nanodots were synthesized using a thermal decomposition method with sucrose. Initially, 0.75 g of sucrose (Sigma-Aldrich) was dissolved in 30 mL of MilliQ water, followed by stirring at room temperature for 30 minutes. This solution was then transferred to a 45 mL Teflon-lined stainless-steel autoclave and heated at a rate of 10 °C min⁻¹ to 180 °C, where it was maintained for 5 hours. Upon cooling the reactor to room temperature, a brown mixture was obtained. This mixture was then centrifuged at 8000 rpm for 20 minutes, after which the resulting pellet was washed thrice with water and subsequently dried at 50 °C for 24 hours.

To deposit carbon nanodots onto the surface of g-C₃N₄, the method described by Liu et al. [189] was followed. Initially, a stock solution containing 1 mg of carbon nanodots in 25 mL of water was prepared. Then, 15.0 mL of this solution was combined with 15.0 mL of NH₄OH (28%) in a 45 mL Teflon-lined autoclave reactor, which was subsequently sealed. The mixture was heated to 150 °C at a rate of 10 °C min⁻¹ and maintained at this temperature for 5 hours. After cooling the reactor to room temperature, the mixture was transferred to a beaker and dried at 80 °C.

Figure 2-12 Preparation of the CD-C₃N₄.

The dried carbon nanodots were then re-suspended in 2.0 mL of water and mixed with 10.0 g of urea. This mixture was calcined at 600 °C for 4 hours (ramp rate 5 °C min⁻¹) and cooled down naturally to room temperature. The resulting carbon nanodots-C₃N₄ (CD-C₃N₄) concentration in the final product was estimated to be approximately $2.4 \times 10^{-3} \text{ g g}^{-1}$ as described by Liu et al. [189].

2.2.2.2 Preparation of the ink

To synthesize the C₃N₄ ink for inkjet printing, adherence to the specifications mentioned in Section 2.2.1.2 was essential. Initially, replication of the composition used for TiO₂ ink was attempted. However, this resulted in a non-stable ink, characterized by rapid sedimentation, primarily due to the larger, 2D form of C₃N₄ particles compared to TiO₂.

Leveraging ink formulation expertise at the IMVT, the recipe by Mogalicherla et al., using ethylene glycol as the primary solvent and water as a co-solvent was adopted [146]. The ink's development involved adjusting the catalyst content, solvent proportions, pH levels, and testing various surfactants. The optimization process was guided by examining particle size, zeta potential, sedimentation behavior, and printability.

Recognizing the influence of ink properties like density, surface tension, and viscosity on droplet formation, a non-dimensional number, Z , akin to the inverse of the Ohnesorge number (Oh) was used, for assessing printability prior to the actual printing process [146, 175, 190]:

$$Z = \frac{1}{Oh} = \frac{Re}{\sqrt{We}} = \frac{(\gamma_{ink} \cdot \rho_{ink} \cdot \alpha_{noz})^{0.5}}{\eta_{ink}} \quad (2-4)$$

In the given equation, η_{ink} represents dynamic viscosity, γ_{ink} denotes surface tension, ρ_{ink} signifies ink density, and α_{noz} refers to the nozzle diameter. The Z number quantifies the balance between surface and inertial forces during droplet formation in print heads. Jang et al. identified the range of $4 < Z < 14$ as optimal for printing in various systems [191], while Derby suggested a range of $1 < Z < 10$ as suitable for printing [190].

The composition of the finalized C_3N_4 ink is detailed in Table 2-2. After mixing the composites, the ink suspension was subjected to ultrasonication using an Elmasonic P device at 80 kHz for 20 minutes to ensure homogeneity and optimal consistency prior to printing.

Table 2-2 Composition of the C_3N_4 ink

Material	Function	Value
C_3N_4 (for both g- C_3N_4 and CD- C_3N_4)	Catalyst	0.3 wt.%
Water	Co-solvent	24.7 wt.%
Ethylene glycol	Main-solvent	75 wt.%
NaOH	Adjusting pH	9 (\pm 0.3)

The ink's dynamic viscosity (η_{ink}) was recorded at 13 mPa s for a shear rate of 100 s^{-1} . Its surface tension (γ_{ink}) measured 0.03 N m^{-1} , determined through ImageJ analysis of a sessile drop image captured by a Krüss DSA25 drop shape analyzer with a drop volume of $5 \text{ }\mu\text{L}$. The ink density (ρ_{ink}) was found to be 1.1 g cm^{-3} , and the nozzle diameter (α_{noz}) was $100 \text{ }\mu\text{m}$. Based on Equation (2-4), the calculated Z number is 4.4, aligning well within the recommended printing range as previously noted.

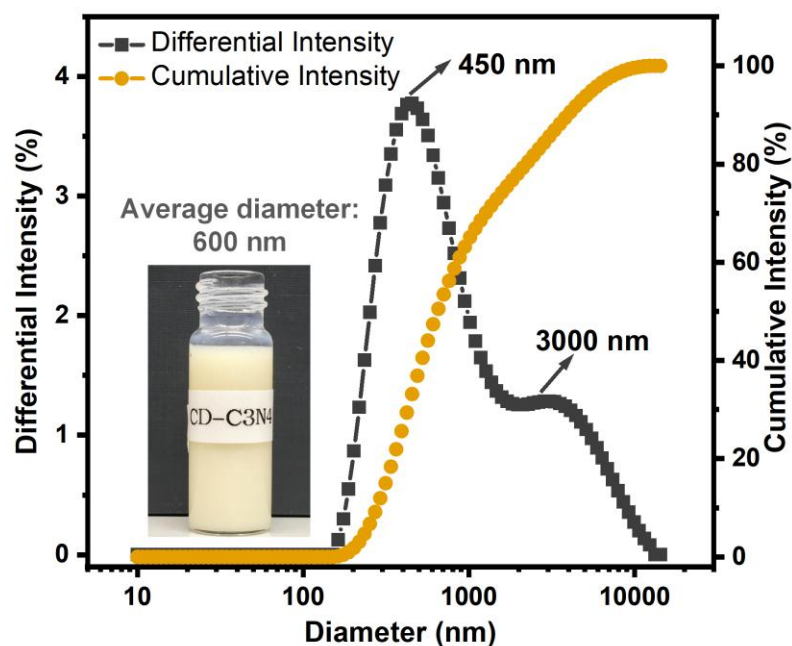


Figure 2-13 Differential and cumulative intensity distribution of the particle size in the CD- C_3N_4 ink (0.3 wt.%) measured by dynamic light scattering (DLS).

Figure 2-13 illustrates that the ink's average particle size is 600 nm, which is within the upper limit of the recommended 1 μm for effective printing using a 100 μm nozzle. The differential particle size distribution reveals two peaks: a prominent peak at 450 nm and a smaller one at 3000 nm, indicating the presence of some larger particles exceeding 1 μm .

The zeta potential of the ink is measured at -40.51 mV, comfortably surpassing the -30 mV criterion for electrostatic stability. Additionally, no significant sedimentation was observed within the initial 2 hours, as illustrated in Figure 2-14, although sedimentation became noticeable after this period.

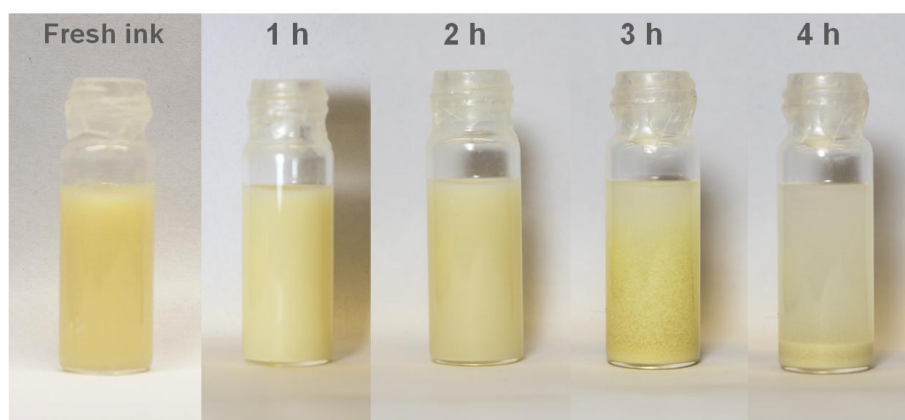


Figure 2-14 CD- C_3N_4 Ink placed for 4 hours.

2.2.2.3 Development of the coatings

The methodology for coating C_3N_4 was closely aligned with the previously established procedure used for TiO_2 . The developed ink demonstrated successful printing at a pulse voltage of 60 V and pulse length of 45 μs , yielding a droplet size of 86 μm . This printing process remained stable for up to 2 hours, as monitored by the printer's CCD camera. Despite the presence of some particles larger than 1 μm , the ink was still printable. The observation of stable droplet formation for 2 hours correlates well with the ink's sedimentation behavior. Post 2 hours, droplet formation became visibly unstable, marked by the emergence of satellite droplets. The ink's functionality could be readily restored with just 5 minutes of sonication.

The substrate utilized was Membrane 2, featuring a 450 Da MWCO. After printing the coated membranes underwent a calcination process in a muffle oven. This was executed at specific temperatures with 2°C min⁻¹ ramp rate. The primary purpose of this calcination was to eliminate solvents and additives, simultaneously improving the adhesion of the coating. The selection of the optimal calcination temperature was guided by evaluating the coatings' catalytic performance in catalyzing the conversion of benzyl alcohol (BA) to benzaldehyde (BAI).

2.2.2.4 Characterization method

XRD, DRS, and Nitrogen Physisorption were conducted to characterize the catalyst powder, with the detailed procedures outlined in Section 2.2.1.4, similar to those applied for TiO_2 . Additionally, Transmission Electron Microscopy (TEM) using bright-field (BF) mode was employed for further examination of the catalyst. The TEM-BF imaging was carried out on a Philips CM200 FEG transmission electron microscope, operating at an acceleration voltage of 200 kV. Image acquisition was facilitated by a TIETZ CMOS F416 (4kx4k) camera. The sample for TEM was prepared by nebulizing a catalyst powder suspension onto a carbon-coated copper TEM grid.

To assess the coating's morphology, SEM was utilized, while Optical Profiling was also employed to determine the coating's thickness with test method described in 2.2.1.4.

2.2.2.5 Characterization results

Figure 2-15 offers detailed insights into the morphological and crystalline characteristics of the synthesized CD- C_3N_4 composite, as revealed by TEM analysis. The TEM images, particularly Figure 2-15 (a), display the CD- C_3N_4 particles (or flakes) with sizes ranging from

approximately 100 to 500 nm, corroborating previous DLS particle size findings. This size range is consistent with the results reported by Liu et al. [189], who observed, using Atomic Force Microscopy (AFM), that the grains of a similarly prepared CD-C₃N₄ composite varied between 90 and 400 nm in diameter, aligning with our observations.

Additionally, Figure 2-15 illustrates the highly porous nature of the CD-C₃N₄ grains, which are composed of carbon nanodots interspersed within a porous g-C₃N₄ matrix. The selected area electron diffraction (SAED) pattern, depicted in Figure 2-15 (a), reveals a series of continuous diffraction halos, confirming the polycrystalline nature of the composite. This diffraction pattern contrasts with the discrete spots that would signify a single-crystalline structure, further underscoring the polycrystalline composition of our CD-C₃N₄ composite.

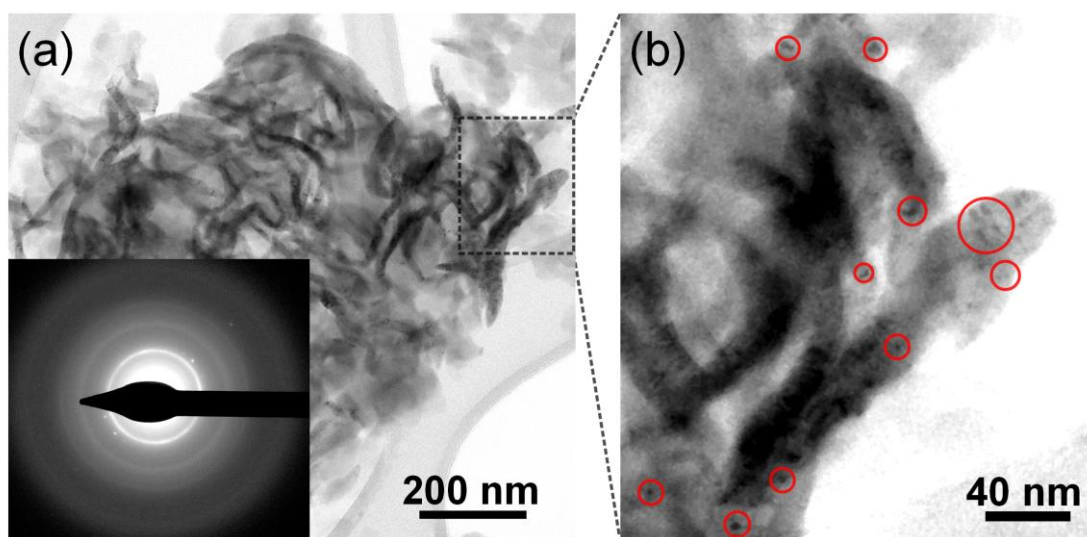


Figure 2-15 Characterization of the as-prepared CD-C₃N₄: (a) TEM image with inset showing the crystal ring pattern of the selected area electron diffraction (SAED); (b) enlarged TEM image of a selected area with red circles indicating the carbon nanodots.

Figure 2-16 depicts the optical properties and bandgap energies of CD-C₃N₄ and g-C₃N₄, analyzed through DRS and Tauc plot interpretation. CD-C₃N₄ displays an absorption edge that extends into the visible light spectrum, indicating that the incorporation of carbon dots has effectively altered the electronic structure of C₃N₄, enabling it to absorb more UV and visible light. The catalysts' color differences, as shown in the insets of Figure 2-16 (a), reflect their absorption characteristics, with CD-C₃N₄'s darker appearance suggesting carbon nanodots incorporation.

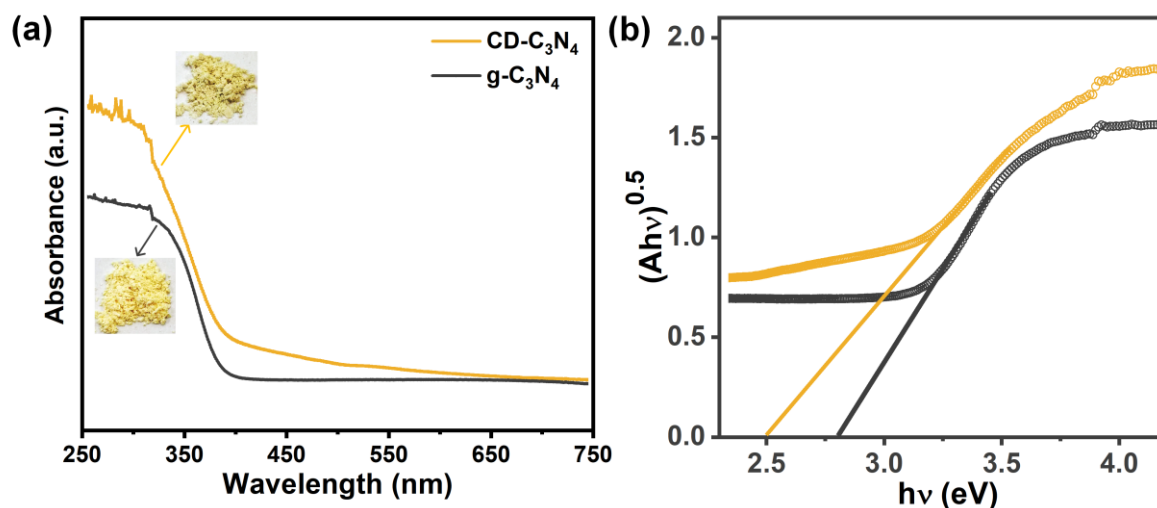


Figure 2-16 (a) DRS spectra of CD-C₃N₄ and g-C₃N₄ (b) Tauc plot showing the $(ah\nu)^{0.5}$ curve for determining the bandgaps of these two catalysts.

The optical band gap of a semiconductor can be estimated from the Tauc plot. The Tauc plot is the curve of converted $(ah\nu)^r$ versus $h\nu$ from the UV-vis spectrum, in which a is the absorption coefficient, h is Planck's constant, ν is the frequency of light, and r depends on the band gap nature (2 for direct, 0.5 for indirect band gap materials). For CD-C₃N₄, a linear fit with $r = 0.5$ suggests an indirect band gap, determining an E_g value of 2.5 eV from the Tauc plot's x-axis intercept (Figure 2-16 (b), yellow curve), while g-C₃N₄ exhibits a bandgap of 2.8 eV.

It is important to note that g-C₃N₄'s band gap characteristics, direct or indirect, may vary based on its structural composition and any modifications made to it [192]. Therefore, applying r values of 0.5 or 2 in Tauc plot analysis might not accurately represent the actual band gap properties of the material.

Figure 2-17 (a) presents the N₂ adsorption-desorption isotherms for CD-C₃N₄ samples, showcasing Type IV isotherms with a hysteresis loop indicative of mesoporous structures. The CD-C₃N₄ exhibits a BET surface area of 85 m² g⁻¹, closely aligning with Lima et al.'s reported 87 m² g⁻¹ for C₃N₄ [193], though higher surface area values exceeding 100 m² g⁻¹ have also been noted [194]. The pore size distribution, peaking at approximately 60 nm, reveals a bimodal pattern that suggests the presence of both small and large mesopores, potentially enhancing the material's surface area and accessibility to its catalytic sites.

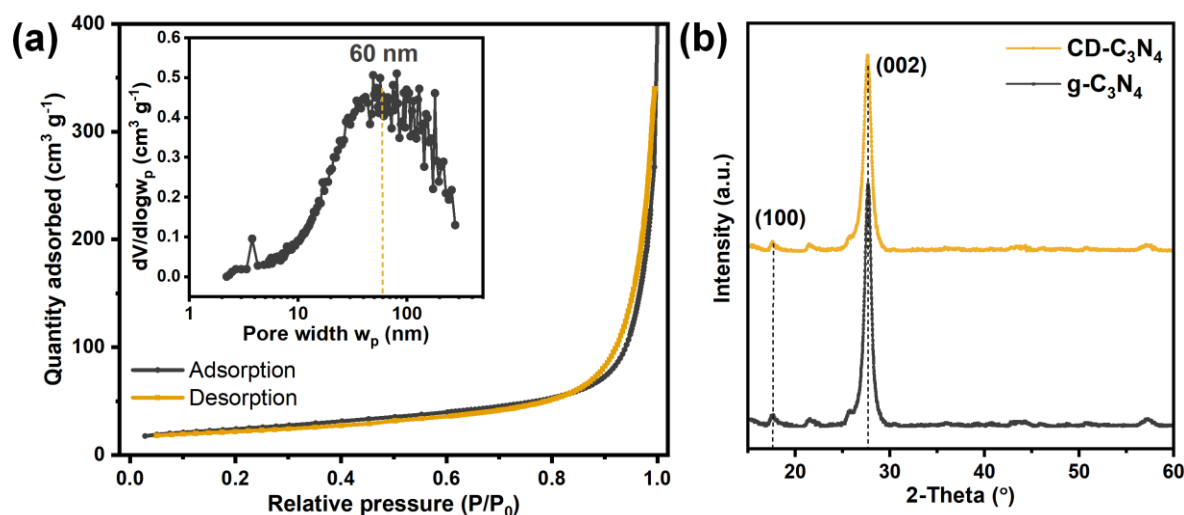


Figure 2-17 (a) N_2 adsorption–desorption isotherms of the $\text{CD-C}_3\text{N}_4$ samples with inset illustrating the BJH desorption pore width distribution; (b) XRD pattern of $\text{CD-C}_3\text{N}_4$ and $\text{g-C}_3\text{N}_4$.

The XRD spectra of $\text{CD-C}_3\text{N}_4$ and $\text{g-C}_3\text{N}_4$, depicted in Figure 2-17 (b), feature two peaks at 13° and 27° , with the latter being the more intense peak associated with the (002) interlayer-stacking structure, and the former attributed to (100) interlayer reflection. These findings are consistent with literature [195, 196]. Notably, the XRD pattern of $\text{CD-C}_3\text{N}_4$ remains largely unchanged from the starting material $\text{g-C}_3\text{N}_4$, likely due to the carbon nanodots' amorphous nature being adsorbed onto the structure.

Figure 2-18 presents an SEM image of a 20-layer $\text{CD-C}_3\text{N}_4$ coating, offering insights into its structure. From Figure 2-18 (a), the coating's high porosity is evident, with layered C_3N_4 flakes obviously visible. The cross-sectional view in Figure 2-18 (b) indicates a consistent coating thickness of approximately $4\ \mu\text{m}$ across the substrate, contrasting with the uneven distribution of the printed TiO_2 layers as previously described. Elemental mapping images, shown in Figure 2-18 (c) and (d), illustrate the uniform distribution of carbon and nitrogen throughout the $\text{CD-C}_3\text{N}_4$ coating, confirming the compositional integrity of the $\text{CD-C}_3\text{N}_4$ structure.

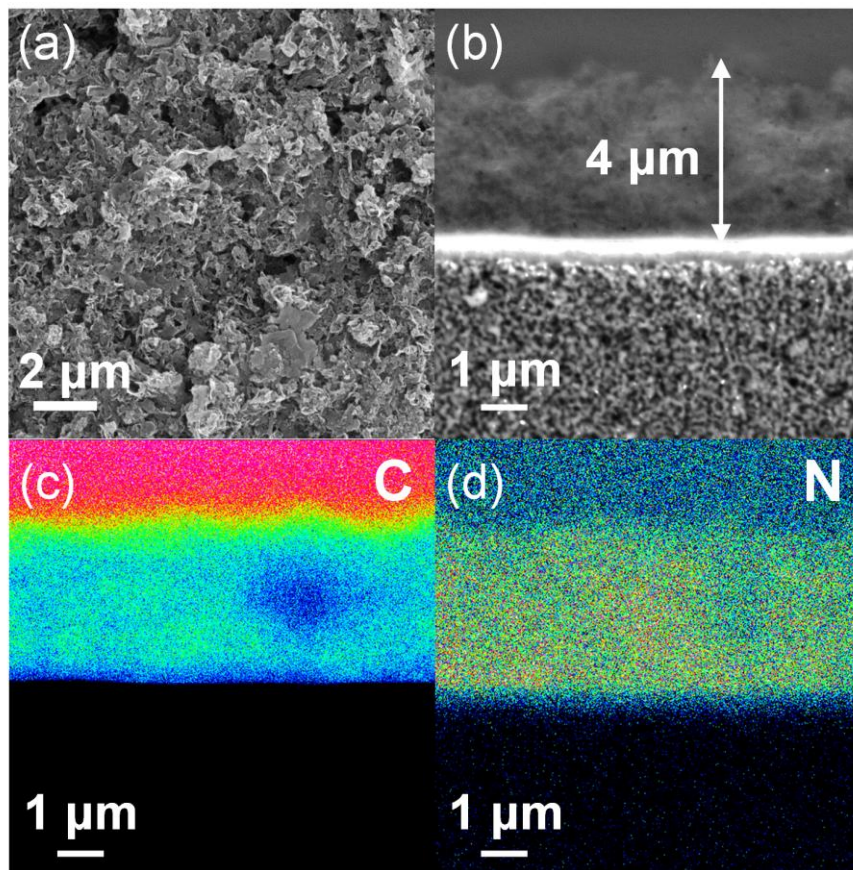


Figure 2-18 SEM images of a 20-layer CD-C₃N₄ coating, showcasing (a) topographical surface details and (b) cross-sectional morphology, complemented by elemental distribution mapping for (c) carbon and (d) nitrogen, with color gradients representing signal intensity from low (blue) to high (red).

Figure 2-19 (a) presents a 3D optical surface profile of the CD-C₃N₄ coating with 30 layers printed on a ceramic substrate, illustrating an even distribution across the substrate on a larger scale as compared with smaller scale shown in Figure 2-18 (b). The mean layer thickness's graphical analysis against the layer number reveals a direct and linear relationship, highlighting the consistency of the deposition process. The 200 nm increase per layer indicates precise control over the coating process, with the standard error margins underscoring the technique's reliability.

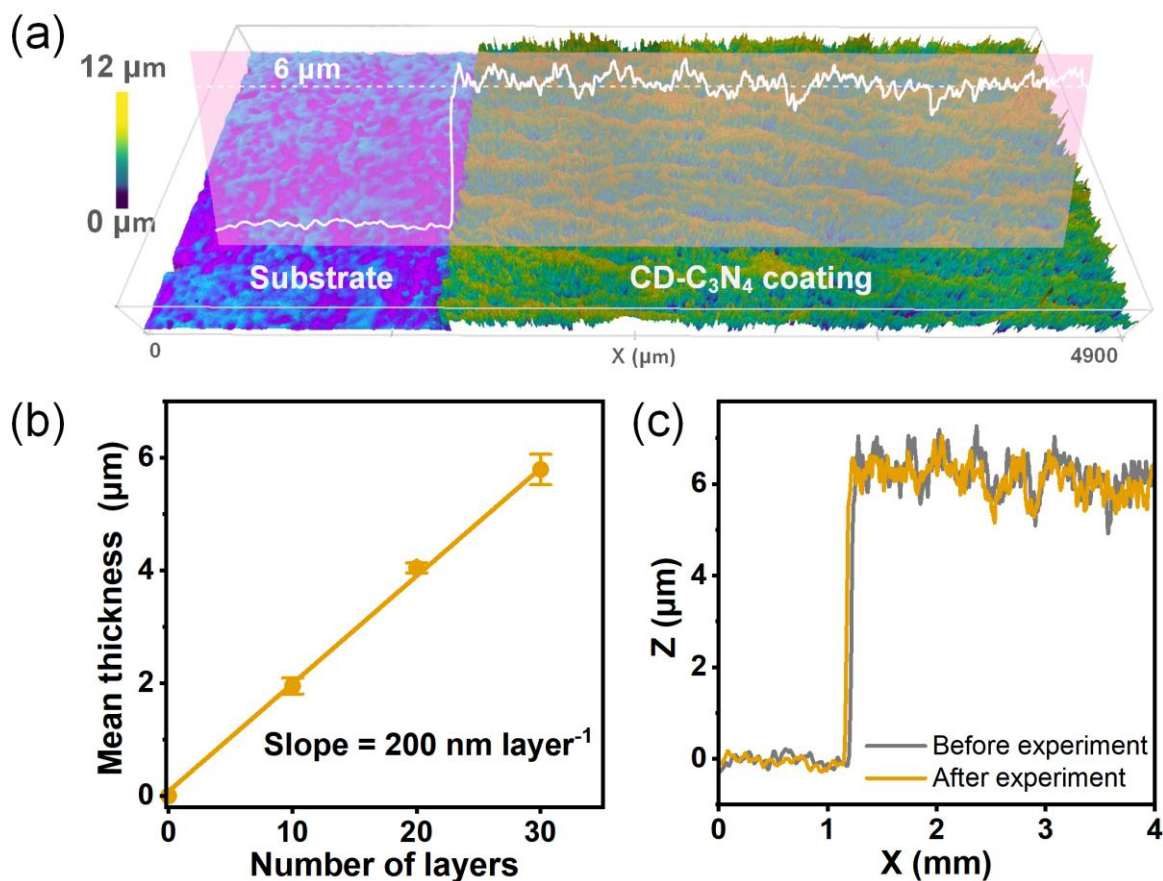


Figure 2-19 (a) 3D optical surface profile image of a sample with 30 printed layers of CD-C₃N₄; (b) mean layer thickness in the function of layer numbers; (c) mean layer thickness of an identical sample before and after a batch experiment (error bars: standard errors).

The coating's durability is further verified by measuring the thickness of an identical sample before and after conducting a batch experiment with a continuously stirred magnet bar beneath the substrate, as detailed in section 2.3.2.2. Figure 2-19 (c) demonstrates that the experimental conditions preserve the coating's thickness, confirming the high stability and strong attachment of the CD-C₃N₄ layers to the substrate.

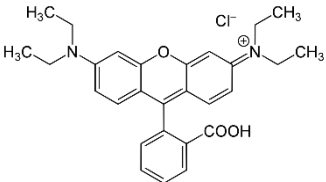
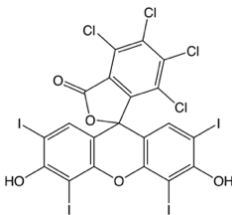
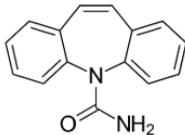
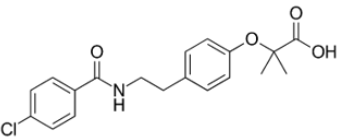
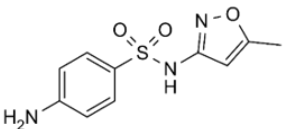
2.3 Experimental protocol and analytics

2.3.1 Photodegradation

2.3.1.1 Chemicals

Rhodamine B (RhB), Carbamazepine (CBZ), Sulfamethoxazole (SMX), and Bezafibrate (BZF) were purchased from Merck, while Rose Bengal (RB) was obtained from Sigma-Aldrich. The physicochemical properties of these model pollutants are detailed in Table 2-3.

Table 2-3 Model pollutants used in this study.

Pollutant	Molecular weight (g mol ⁻¹)	Structural formula	pKa
RhB	479		4.2 [197]
RB	974		pKa ₁ = 3.93 and pKa ₂ = 1.89 [198]
CBZ	236		pKa ₁ < 2.3 and pKa ₂ ≥ 13.9 [199]
SMX	253		pKa ₁ = 1.7 and pKa ₂ = 5.6 [200]
BZF	362		3.2 [201]

Stock solutions for RhB and RB were prepared at 15 mg L⁻¹ by dissolving the respective dye powders in deionized water (Milli-Q, Merck). The concentrations for CBZ, SMX, and BZF solutions were set at 20 µg L⁻¹ (lab experiment) or 50 µg L⁻¹ (sunlight experiment) achieved by

diluting a 10 mg L^{-1} mother solution in methanol by a factor of 500 with deionized water. The pH of the solutions was not adjusted unless specified otherwise. The recorded pH values for the solutions were as follows: RhB at 8.3, RB at 8.1, CBZ at 7.2, SMX at 7.3, and BZF at 7.3. It is important to note that all chemicals used in preparing these solutions were of analytical grade.

2.3.1.2 Batch reactor experiment

Prior to the μPMR experiments, catalyst performance was evaluated using a batch reactor test to optimize parameters such as calcination temperature after inkjet-printing catalyst on the ceramic substrate. Furthermore, kinetic studies, a crucial aspect of the photodegradation section of this dissertation, were conducted in the batch reactor to determine kinetic parameters. For these studies, RhB served as the sole model pollutant.

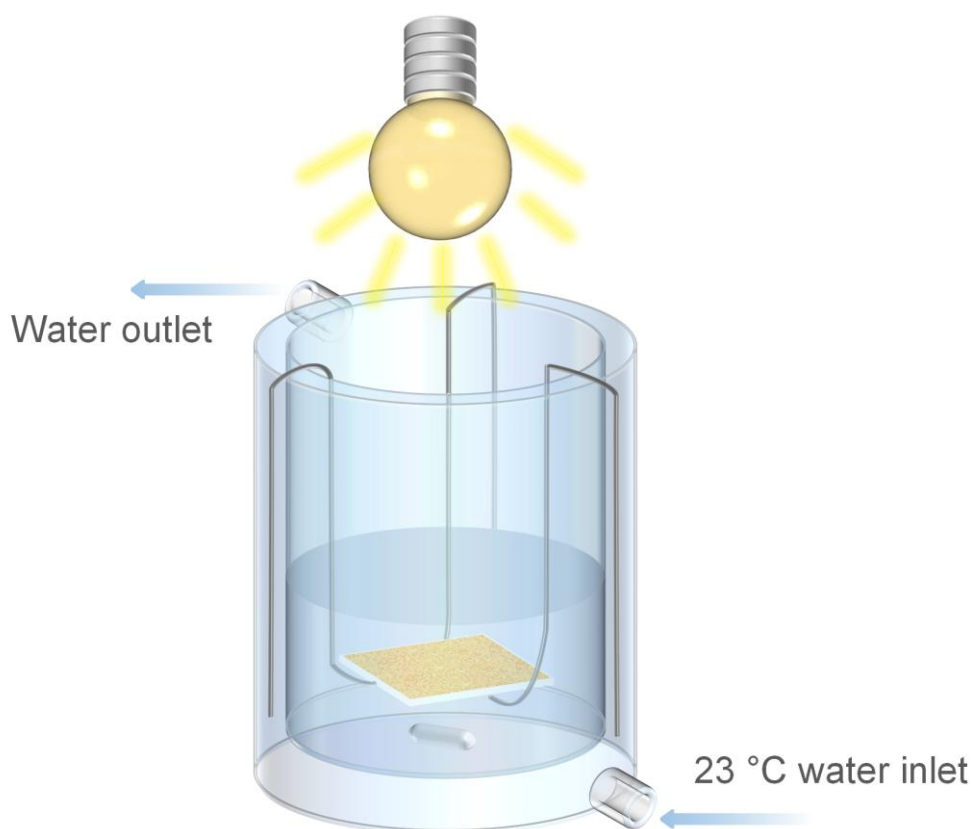


Figure 2-20 Illustration of the batch reactor set-up. [64]

The experimental setup, depicted in Figure 2-20, utilized a halogen lamp (VL-115.L, Vilber Lourmat) emitting UV light at a wavelength of 365 nm as the light source. The prepared sample (ceramic membrane with catalyst coating) was submerged 3 mm below the solution's surface (14 mL total volume) and secured in a stainless-steel holder. Light intensity at the sample's location was measured at 3.5 mW cm^{-2} using a UV irradiation meter TM213 (Tenmars). The

solution temperature was kept at 23 °C by recirculating water via a Polystat CC1 (Huber).

Prior to irradiation, the solution was magnetically stirred in the dark for 60 min, which - according to preliminary tests - is sufficient for the establishment of an adsorption/desorption equilibrium between the immersed sample and the pollutant. RhB concentration was periodically measured by extracting 1 mL of solution, which was then returned to maintain volume. The effects of varying initial RhB concentrations (3, 6, 12, 15 g m⁻³) and catalyst layer thicknesses (110 - 990 nm) on degradation were assessed. Blank tests with non-coated substrates under irradiation showed negligible degradation.

2.3.1.3 Continuous-flow experiment in the μ PMR

The μ PMR experiments utilized the custom-built μ PMR depicted in Figure 2-1 and the continuous-flow system from Figure 2-3. As outlined in chapter 2.1.2, four distinct flow modes were employed:

Mode 1: Mixed flow-through and surface-flow contactor mode with light;

Mode 2: Pure surface-flow contactor with built-in oxygen distributor with light;

Mode 3: Nanofiltration mode in a cross-flow configuration without light;

Mode 4: Pure surface-flow contactor with light;

Before starting, the system was flushed with the pollutant solution for an hour at a 0.5 mL min⁻¹ inlet flow rate and 1 bar pressure (excluding Modes 2 and 4, which did not require pressure) to saturate the system with the pollutant, based on preliminary equilibrium tests. After reaching stability, experimental conditions were precisely adjusted. A further 30-minute stabilization was followed by regular sampling throughout the experiment. These samples were analyzed to determine the concentration (analytical method introduced in 2.3.1.5), and the flow rates of retentate and permeate were calculated by dividing the mass of each sample by the duration of sampling.

For Modes 1 and 3, samples were collected from both retentate (outlet 1) and permeate (outlet 2) for concentration analysis. In Mode 2, the oxygen overpressure in the lower microchannel was set at 0.2 bar to allow oxygen diffusion through the membrane, with only upper microchannel (outlet 1) samples analyzed. Mode 4 also involved analysis of samples from outlet 1 only. Steady-state conditions were confirmed via material balance monitoring (Figure C 1), with blank tests in Mode 4 using a metal plate instead of a coated membrane.

Table 2-4 Summary of experimental parameters

Pollutant	Mode	Light type	Light intensity (mW cm ⁻²)	Inlet flow rate (mL min ⁻¹)	Pressure (bar)
RhB	3	/	/	0.5	10
RhB	1, 2, 4	UV	0.5 ~ 1.5	0.2 ~ 0.6	0.3 ~ 0.8
RB	1	UV	2	0.2	0.2 ~ 0.8
CBZ, SMX, BZF	1	UV	1.5	0.1	0.2
CBZ, SMX, BZF	1	Vis	0.8	0.1	0.3

Table 2-4 summarizes key experimental variables (light type, intensity, flow rate, and pressure). To ensure reproducibility, each experiment was repeated three times, unless otherwise stated, with standard error representing the variation. Notably, in Mode 1, "pressure" refers to the overpressure in the upper microchannel relative to atmospheric pressure, with adjustments made to maintain a consistent split between permeate and retentate. Mode 3 operated at a constant 10 bar, whereas Modes 2 and 4 had no pressure adjustments.

2.3.1.4 Real sunlight experiment

The versatility and functionality of the system were further assessed through experiments conducted under actual sunlight conditions, as depicted in Figure 2-21 and Figure 2-22. Utilizing the catalyst N-TiO₂, applied in 10 inkjet-printed layers, the system's proficiency in degrading the model dye pollutant RhB and the micropollutants SMX and BZF was tested. For simplicity and to reduce experimental complexity, a dead-end flow mode was employed.

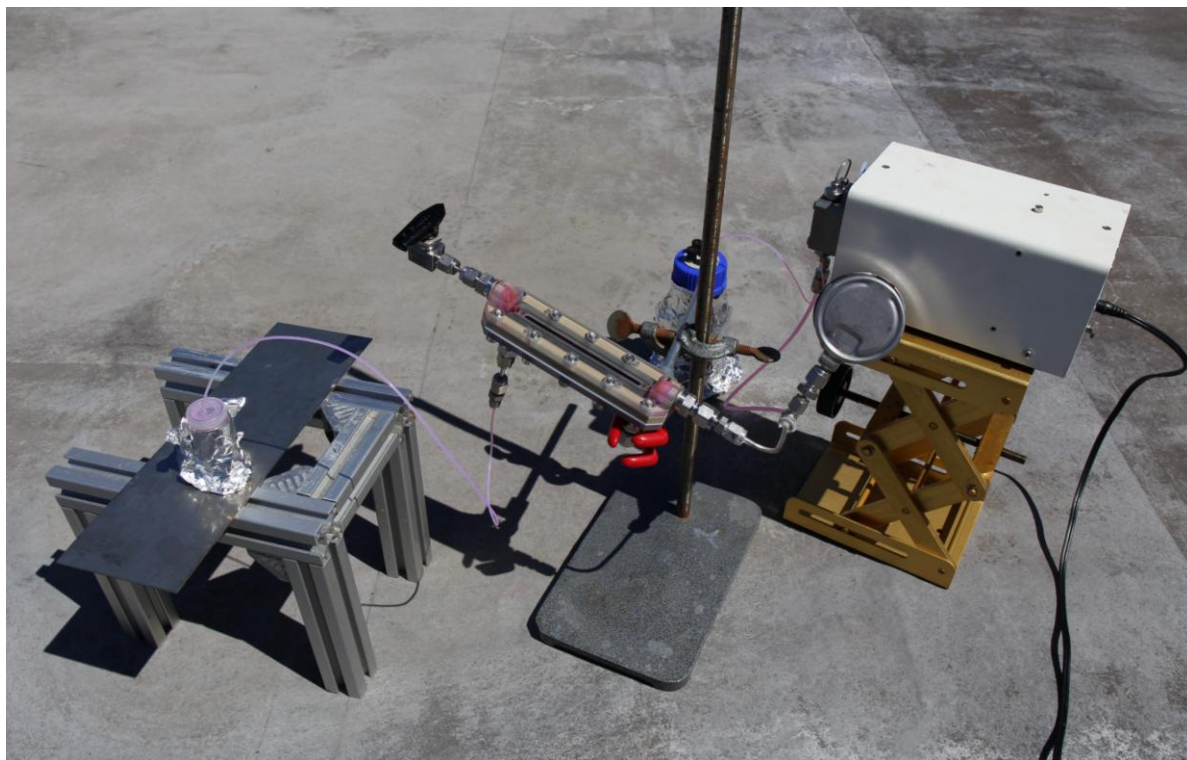


Figure 2-21 Continuous-flow system for sunlight experiment.

On the afternoon of July 9, 2020, from 16:30 to 18:20, the light intensity naturally declined from 90 to 78 mW cm^{-2} as the sunlight waned, while the system worked to degrade RhB at an inlet concentration of 15 mg L^{-1} , with an inlet flow rate maintained at 0.1 mL min^{-1} .

This was followed by experiments on July 11 and 12, 2020, targeting the micropollutants SMX and BZF at 20 $\mu\text{g L}^{-1}$ concentrations, with light intensities measured at 98 mW cm^{-2} and approximately 96 mW cm^{-2} , respectively, during midday when the sunlight was at its peak.

Before each experiment, a 30-minute period was allotted for the system to reach a material balance, after which samples were collected at 20-minute intervals. Conducted without replication, these tests offered preliminary but valuable insights into the photocatalytic capabilities of the system under real-world sunlight exposure.

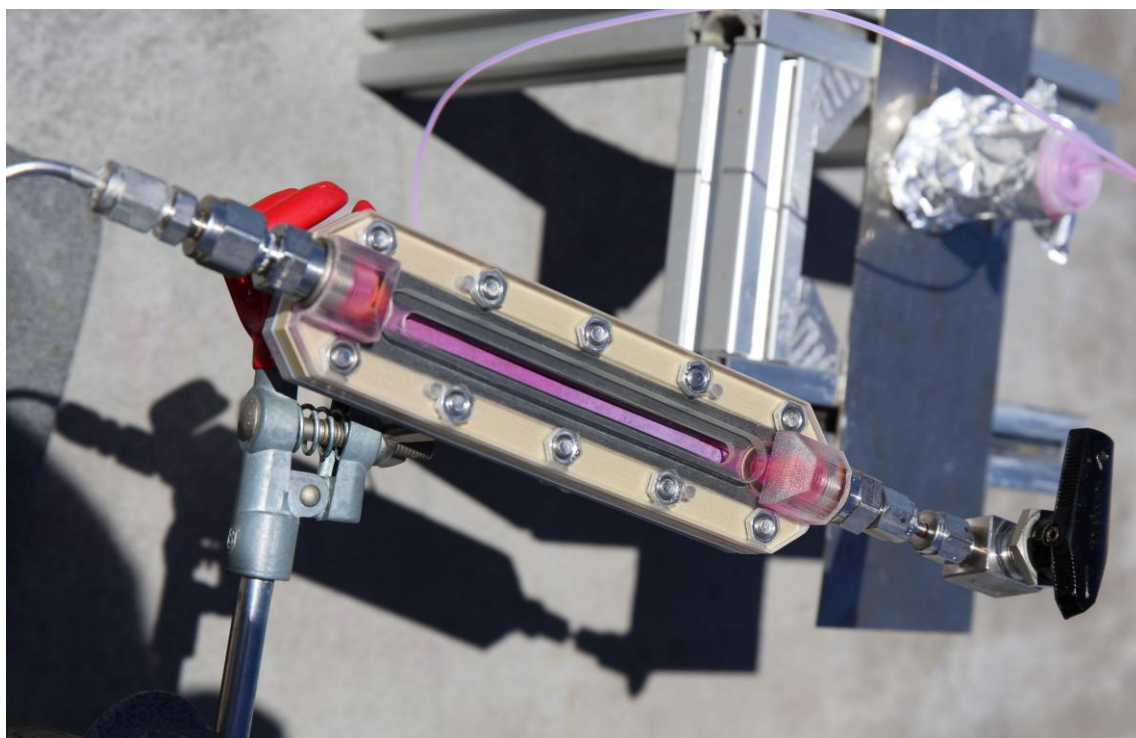


Figure 2-22 Reactor in photodegradation experiment under sunlight.

2.3.1.5 Analytics

The concentrations of RhB and RB were determined using a UV-Vis Spectrophotometer (HP, 8453) at wavelengths of 554 and 562 nm, respectively. Figure 2-23 exemplifies the spectrum of RhB during a batch reactor degradation experiment over a period of 360 minutes.

The concentrations of SMX, CBZ and BZF were analyzed via LC-MS/MS. Mass spectrometric (MS) analysis was performed using an API 4000TM quadrupole mass spectrometer (Applied Biosystems/MDS Sciex Toronto) equipped with an electro spray ionization (ESI) source. MS/MS was conducted by using the compound optimization mode in the software Analyst V 1.6.3. An Agilent 1100 HPLC system was used for sample separation using a LiChrospher 100 RPC-18 EC column (5 μm , 125 x 4 mm). A gradient of acetonitrile (ACN) and 0.1 % acetic acid (AcOH) was used, resulting in a total run time of 30 min. The initial conditions of the gradient (ACN: 0.1 % AcOH) were set at 30:70, ramped to 80:20 within 9 min, held for 5 min and then returning to 30:70 to equilibrate the column for the next run. The ion source temperature was set to 400 $^{\circ}\text{C}$, and a flow rate of 500 $\mu\text{L min}^{-1}$ was applied. The injection volume for all samples was 20 μL . The retention time for SMX, CBZ and BZF was 7.2, 8.7 and 10.3 min, respectively.

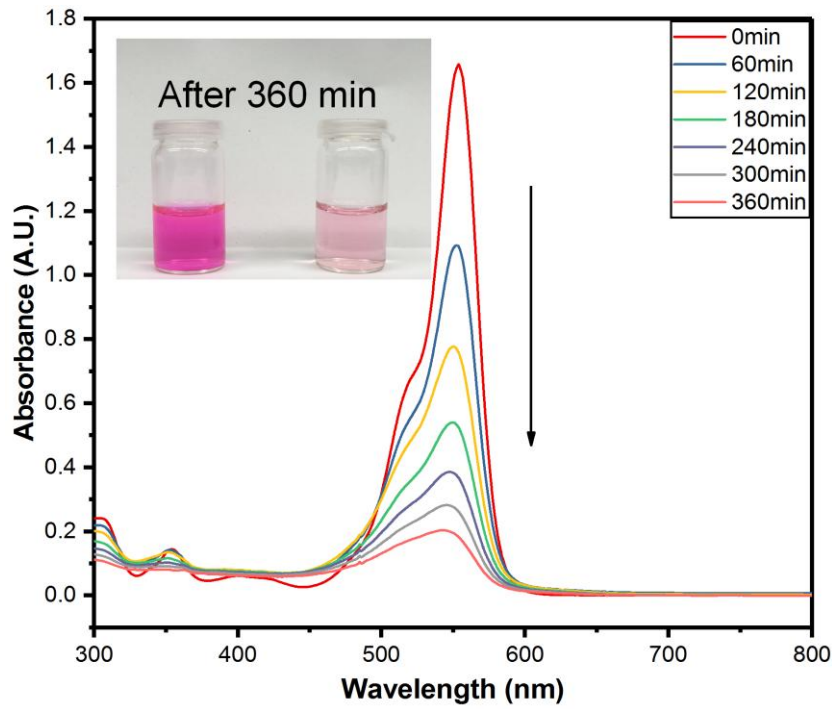


Figure 2-23 UV-Vis spectrum of RhB in a batch reactor over 360 min using a 990 nm thick TiO₂ P25 coating under UV light. Inset shows the RhB color change during 360 min.

2.3.1.6 Calculation

In batch experiments, the degradation performance is evaluated by monitoring the degree of removal for the pollutant X_{re} [%] over a specified time, t [s], using Eq. (2-5):

$$X_{re} = \frac{C_0 - C_t}{C_0} \times 100 \quad (2-5)$$

Here, C_0 [g m^{-3}] is the initial bulk concentration and C_t [g m^{-3}] is the bulk concentration at time t , with the assumption of uniform concentration throughout the reactor due to vigorous stirring (will be discussed in detail in section 3.1).

For the continuous-flow μPMR experiment, considering the steady state of the operation, the material balance for the reactor can be written as:

$$\dot{V}_0 \cdot C_0 = \dot{V}_1 \cdot C_1 + \dot{V}_2 \cdot C_2 + R_{\text{obs-PMR}} \quad (2-6)$$

where \dot{V}_0 , \dot{V}_1 and \dot{V}_2 is the volumetric flow rate [$\text{m}^3 \text{s}^{-1}$] of inlet, retentate and permeate, respectively; C_0 , C_1 and C_2 is the inlet, retentate (outlet 1) and permeate (outlet 2) concentration of pollutant [g m^{-3}]. $R_{\text{obs-PMR}}$ is the observed reactor-averaged reaction rate of photodegradation of pollutant in the μPMR [g s^{-1}], which is calculated by transforming Eq. (2-6) to the following:

$$R_{\text{obs-PMR}} = \dot{V}_0 \cdot C_0 - \dot{V}_1 \cdot C_1 - \dot{V}_2 \cdot C_2 \quad (2-7)$$

The μPMR 's photodegradation performance is assessed using the degree of removal X_{re} [%], as with batch experiments, defined by Eq. (2-8):

$$X_{\text{re}} = \frac{\dot{V}_0 \cdot C_0 - \dot{V}_1 \cdot C_1 - \dot{V}_2 \cdot C_2}{\dot{V}_0 \cdot C_0} \times 100 \quad (2-8)$$

For Modes 2 and 4, and in blank tests where only outlet 1 is active, the term $\dot{V}_2 \cdot C_2$ in Eq. (2-8) vanishes. For Mode 3, only permeate flow from outlet 2 was active, and hence term $\dot{V}_1 \cdot C_1$ in Eq. (2-8) vanishes, and the degree of removal denotes the membrane rejection α_{mem} [%], which is calculated as:

$$\alpha_{\text{mem}} = X_{\text{re}} = \frac{\dot{V}_0 \cdot C_0 - \dot{V}_2 \cdot C_2}{\dot{V}_0 \cdot C_0} \times 100 \quad (2-9)$$

To standardize the measurements and simplify calculations, concentrations initially provided in $[\text{mg L}^{-1}]$ and $[\mu\text{g L}^{-1}]$ have been standardized here to $[\text{g m}^{-3}]$. Similarly, flow rates have been adjusted from $[\text{mL min}^{-1}]$ to $[\text{m}^3 \text{s}^{-1}]$.

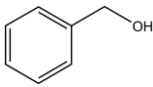
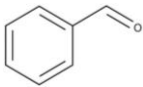
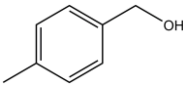
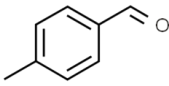
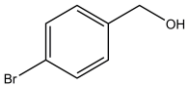
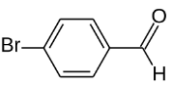
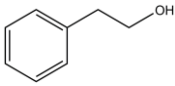
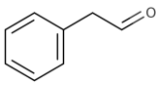
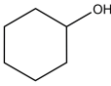
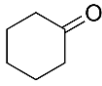
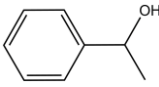
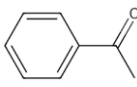
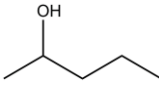
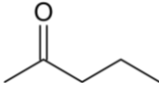
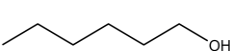
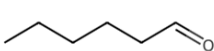
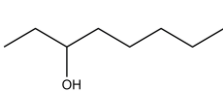
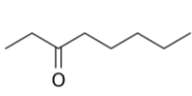
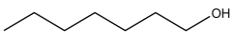
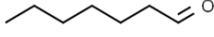
2.3.2 Selective photooxidation

2.3.2.1 Chemicals

For the investigation of selective photooxidation, a variety of alcohols served as substrates, with their conversions to corresponding aldehydes being the focus. The reagents utilized are cataloged in Table 2-5. With the exception of specific mentions, all chemicals, purchased from Sigma-Aldrich, Fluka, Acros, or Alfa-Aesar, were of the highest available purity and used as received.

Solutions of the alcohols and aldehydes were prepared by first creating a concentrated mother solution, which was then diluted to the required concentrations. The pH levels were not altered for these solutions.

Table 2-5 Alcohols and aldehydes used in this work

Substrate - Alcohol	Structural Formula	Target - Aldehyde	Structural Formula
Benzyl alcohol		Benzaldehyde	
4-Methylbenzyl alcohol		4-Methylbenzaldehyde	
4-Bromobenzyl alcohol		4-Bromobenzaldehyde	
Phenethyl alcohol		Phenylacetaldehyde	
Cyclohexanol		Cyclohexanone	
1-Phenylethanol		Acetophenone	
2-Pentanol		2-Pentanone	
1-Hexanol		Hexanal	
3-Octanol		3-Octanone	
1-Heptanol		Heptanal	

2.3.2.2 Batch reactor experiment

The catalyst coating's performance was evaluated using square substrates of 2.5 cm × 2.5 cm in batch experiments, considering factors such as calcination temperature, catalyst type, solvent, gaseous environment, layer number, and initial concentration. The experimental setup is similar to the one used in photodegradation, as depicted in Figure 2-20 and Figure 2-24. The light

source is an in-house developed xenon lamp with a 200 W power (supplier: Lifyn2) for illumination, standardized to a light intensity of 100 mW cm^{-2} . The initial volume of the substrate solution was 15 mL. Temperature control was maintained at $23 \text{ }^{\circ}\text{C}$ through water recirculation. Gas flow was set at 5 mL min^{-1} at atmospheric pressure. Experiments were conducted over 4 hours, except for those assessing initial concentration variations, which extended to 12 hours. The specific conditions for each experiment are summarized in Table 2-6.

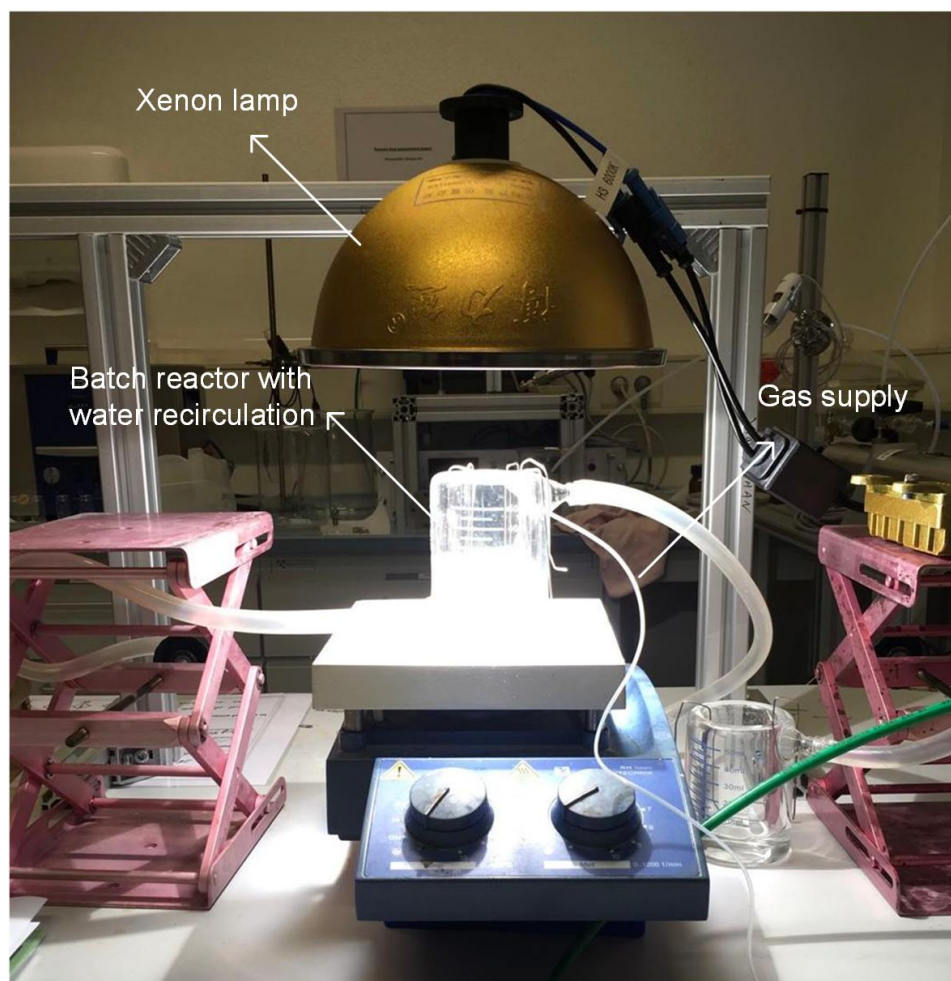


Figure 2-24 Picture of the batch reactor setup for photooxidation of alcohols

It is crucial to acknowledge that despite water recirculation, solvent evaporation occurred during the experiments, potentially due to the thermal effects from the high-power lamp on the solution's surface, influencing concentration measurements. To address this issue, the evaporation rates of the two solvents employed in this study were quantified based on three independent replicates. The rates were determined to be 0.538 mL h^{-1} for CH_3CN and 0.125 mL h^{-1} for water, respectively. These values were subsequently used to correct the actual concentrations of alcohols and aldehydes over defined experimental durations using the following equation:

2. Experimental procedures and characterization

$$C_{act} = C_{meas} \times \frac{V_{ini} - V_{eva}}{V_{ini}} \quad (2-10)$$

Here, C_{act} denotes the corrected concentration, C_{meas} the measured concentration, V_{ini} the initial solution volume (15 mL), and V_{eva} the total evaporated volume, calculated as the product of the evaporation rate and the experimental duration.

Table 2-6 Experimental condition of the photooxidation experiment in the batch reactor.

Investigated variable	Calcination temperature [°C]	Catalyst	Solvent	Gas	Layer number	Initial concentration [mM]
Calcination temperature	200 250 300 350 400	CD-C ₃ N ₄	CH ₃ CN	O ₂	10	0.5
Catalyst	350	CD-C ₃ N ₄ g- C ₃ N ₄ TiO ₂	CH ₃ CN	O ₂	10	0.5
Solvent	350	CD-C ₃ N ₄	CH ₃ CN H ₂ O	O ₂	10	0.5
Gas	350	CD-C ₃ N ₄	CH ₃ CN	N ₂ Air O ₂	10	0.5
Layer number	350	CD-C ₃ N ₄	CH ₃ CN	O ₂	10 20 30	0.5
Initial concentration	350	CD-C ₃ N ₄	CH ₃ CN	O ₂	30	0.5 5

2.3.2.3 Continuous-flow experiment in the μ PMR

In the continuous-flow experiments conducted with the μ PMR, Modes 1 and 4 were implemented. Specifically, Mode 1 operated in dead-end flow, akin to a membrane contactor mode. A comparative analysis of the two modes was conducted by recirculating the outlet fluid back to the feed bottle across an 8-hour duration to attain distinctively differential results. Benzyl alcohol (BA) was the sole substrate used in these experiments. Illumination was provided by the same light source as in the batch experiments, maintaining an intensity of 100 mW cm⁻². Acetonitrile (CH₃CN) served as the solvent, and the catalyst was CD-C₃N₄, which was coated for 30 layers followed by a 350 °C calcination. The starting concentration of the reactant was 0.5 mM, and no gas was introduced during the experiment. Concentration measurements were derived from feed bottle samples taken after the 8-hour duration.

Subsequently, Mode 1 was tested again in a dead-end flow configuration without solution recirculation, allowing for single-run outlet monitoring over 12 hours. Samples were collected

for concentration analysis at the beginning and then hourly.

2.3.2.4 Analytics

The concentration of benzyl alcohol (BA) and benzaldehyde (BAI) was determined using a PerkinElmer LC 300 HPLC system equipped with a C18 column (250 mm × 4.6 mm, 5 μm particle size). The column temperature was maintained at 30 °C. The mobile phase consisted of a 70:30 volume ratio mixture of water and acetonitrile with 0.2 M phosphoric acid. The flow rate of the mobile phase was set at 1 mL min⁻¹, and the injection volume for each sample was 20 μL. Detection was performed using a UV-Vis detector at a wavelength of 210 nm. Each run was completed within a duration of 5 minutes. Calibration curves for BA and BAI were established using five standard concentrations in the range of 0.2 to 2 mM, which displayed excellent linearity with an R-squared value greater than 0.999. This ensured the accuracy and reliability of the concentration measurements obtained from the HPLC analysis.

The concentrations of other aliphatic and aromatic alcohols (Table 2-6), along with their corresponding aldehydes, were determined using gas chromatography (GC) equipped with a flame ionization detector (FID) operating at 280 °C. The inlet temperature was controlled at 250 °C. Helium served as the carrier gas, with hydrogen fueling the flame. The oven temperature program commenced at an initial temperature of 130 °C, holding for 1 minute, then ramping up at 5 °C min⁻¹ to 180 °C, holding for another 2 minutes, and finally increasing the temperature at a rate of 30 °C min⁻¹ to a terminal temperature of 220 °C with a 1-minute hold. For most substrates and their aldehydes, except for 1-Hexanol and 1-Heptanol, 1-Hexanol was employed as the internal standard to ensure analytical consistency. For 1-Hexanol and 1-Heptanol analyses, 3-Octanol was utilized as the internal standard.

2.3.2.5 Calculation

The alcohol conversion X_o [%], aldehyde selectivity S_o [%], and aldehyde yield Y_o [%] are calculated as

$$X_o = \frac{C_{AL0} - C_{AL1}}{C_{AL0}} \times 100 \quad (2-11)$$

$$S_o = \frac{C_{AID1}}{C_{AL0} - C_{AL1}} \times 100 \quad (2-12)$$

$$Y_o = \frac{C_{AID1}}{C_{AL0}} \times 100 \quad (2-13)$$

In batch experiments, C_{AL0} represents the initial concentration of the substrate alcohol before exposure to light. C_{AL1} is the concentration of the substrate alcohol following a period of

illumination, while C_{AID1} indicates the concentration of the formed aldehyde after this illumination period.

In continuous-flow experiments utilizing the μ PMR, C_{AL0} signifies the initial concentration of the substrate alcohol, either in the recirculation setup within the feed bottle or as the inlet concentration in single-pass experiments prior to light exposure. C_{AL1} corresponds to the concentration of the substrate alcohol either remaining in the feed bottle after a certain duration of illumination in recirculation experiments or at the outlet in single-pass experiments. Similarly, C_{AID1} denotes the concentration of the produced aldehyde either in the feed bottle following the specified period of illumination in recirculation setups or at the outlet in single-pass experiments.

The subscript “o” is utilized to signify parameters related to photooxidation experiments, distinguishing them from degradation experiments, where “re” indicates removal. “Al” means alcohol while “AlD” means aldehyde.

3. Photocatalytic degradation of pollutant

This chapter delves into the photocatalytic degradation of pollutants, commencing in the first part with a kinetic analysis conducted through both batch and μ PMR experiments. The second part explores the μ PMR's utility in enhancing RhB photodegradation, particularly focusing on the synergistic interplay between membrane filtration and photocatalysis. Additionally, the μ PMR's efficacy in the photodegradation of three classic micropollutants is presented. It concludes with an examination of degradation under real sunlight conditions, highlighting the practical applicability of the system.

3.1 Kinetic study - from batch to continuous-flow microreactor

Kinetic studies are important for understanding the specific local conditions and processes governing photocatalytic pollutant degradation. The kinetic study of this work is anticipated to enrich our understanding of the photodegradation process across batch and continuous-flow reactor setups. Additionally, it seeks to highlight the μ PMR system's capability in performing precise kinetic analyses, attributable to its operation under well-defined conditions.

The study starts by establishing models that incorporate a light irradiation model specifically tailored to the catalyst coating, complemented by reaction kinetic models designed for both batch and continuous-flow reactor systems. In the context of the batch reactor, several reaction constants are determined for the intrinsic kinetic model, which are subsequently applied to the continuous-flow setup. The developed models are then assessed through a comparison between the simulated outcomes and actual experimental data for RhB degradation with TiO_2 P25. It is important to note that within this kinetic study, only the surface-flow configuration (Mode 4) was employed for the continuous-flow scenario.

3.1.1 Modelling

3.1.1.1 Light irradiation model

In photocatalysis, the rate of reaction is influenced by factors beyond just the concentration of reactants and temperature. It is significantly affected by the number of photons striking the catalyst's surface per unit time and their energy. For a fixed wavelength, to isolate the impacts of photon flux and photon energy from those of concentration and temperature, the reaction rate constant k [$\text{g g}^{-1} \text{s}^{-1}$], can be modeled to depend on the light intensity I [mW cm^{-2}] as follows [106]:

$$k = aI^b \quad (3-1)$$

a [$\text{g cm}^{2b} \text{g}^{-1} \text{s}^{-1} \text{mW}^{-b}$] and b [-] are constants to be determined from experiments. b is dimensionless whereas the unit of a depends on the value of b . In scenarios involving immobilized photocatalysts, the light intensity I decays along the irradiation direction y toward the bottom of the layer. This attenuation of light intensity can be described by the Beer-Lambert Law (as illustrated in Figure 3-1):

$$I = I_0 e^{-\omega y} \quad (3-2)$$

Here, I_0 [mW cm^{-2}] is the incident light intensity and ω [m^{-1}] is the extinction coefficient. ω can be determined by fitting the measured transmission T_L to the layer thickness δ_L [m] according to the following equation:

$$-\ln(T_L) = \omega \delta_L \quad (3-3)$$

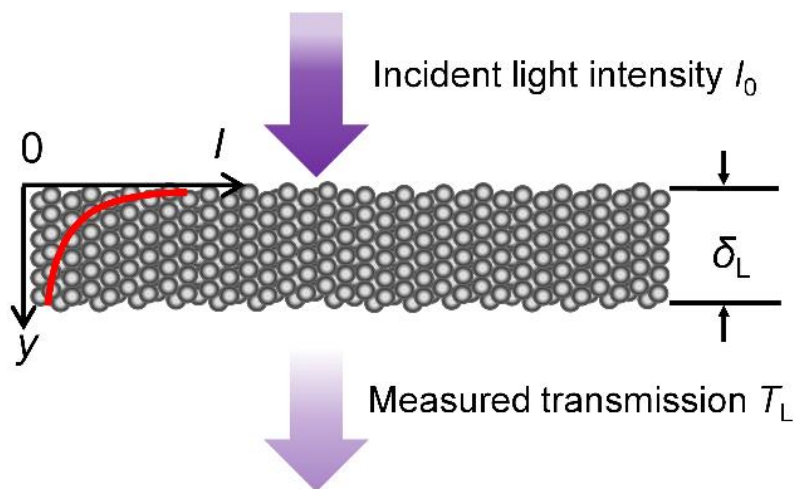


Figure 3-1 Light penetration through the photocatalyst layer. [64]

The effective rate constant \bar{k} [$\text{g g}^{-1} \text{s}^{-1}$] of a catalyst layer with thickness of δ_L is then found by integrating Eq. (3-1) over the layer thickness:

$$\bar{k} = \frac{1}{\delta_L} \int_0^{\delta_L} k(y) dy = \frac{1}{\delta_L} \int_0^{\delta_L} a I_0^b e^{-b\omega y} dy = \frac{a I_0^b}{b\omega\delta_L} (1 - e^{-b\omega\delta_L}) \quad (3-4)$$

The parameters a and b are experimentally ascertainable by conducting tests with varying thicknesses of the catalyst layer δ_L , while maintaining constant temperature and light wavelength, ensuring the absence of mass transport limitations. These conditions were adhered to in the batch reactor experiments of this study, as will be discussed in Section 3.1.1.2.

For the formulation of the light irradiation model pertinent to this research, several key assumptions were made:

- The UV lamp operates stably, with its irradiance remaining constant throughout the duration of the experiment.
- The light is uniformly distributed across the geometric surface of the catalyst layer, with the incident intensity denoted as I_0 .
- The catalyst layer possesses a uniform structure, ensuring consistent photocatalytic activity across its entirety.

3.1.1.2 Reaction kinetics

The concentration of the model pollutant RhB was determined through its measured absorbance, employing the Lambert-Beer law that establishes a relationship between absorbance and concentration. Any potential impact of temperature variations on the kinetic processes during the experiments was deemed negligible, as evidenced by the stable temperature measurements of the RhB solution in both reactor systems, which remained within a ± 2 K range.

The following Langmuir-Hinshelwood (LH) expression is a widely used model for describing heterogeneous photocatalytic reactions [61, 66]. For a monomolecular irreversible degradation reaction, r_{int} [g s^{-1}], according to Eq. (3-5), is the intrinsic reaction rate:

$$r_{\text{int}} = \frac{k_{\text{int}} g_{\text{cat}} K_{\text{LH}} C}{1 + K_{\text{LH}} C} \quad (3-5)$$

where k_{int} [$\text{g g}^{-1} \text{s}^{-1}$] is the intrinsic (catalyst-mass-related) rate constant, g_{cat} [g] is the catalyst mass, K_{LH} [$\text{m}^3 \text{g}^{-1}$] is the adsorption equilibrium constant of the reactant, and C [g m^{-3}] is the mass concentration of the pollutant in the liquid phase. Note that the reaction rate is always

positive. When applying Eq. (3-5) to the printed catalyst layers of this study, k_{int} has to be replaced with \bar{k} from Eq. (3-4).

As opposed to the intrinsic reaction rate, the observed rate of consumption of the pollutant in the batch reactor $R_{\text{obs-batch}}$ [g s^{-1}] is defined in accordance with the material balance for the pollutant:

$$R_{\text{obs-batch}} = V_{\text{batch}} \frac{dC_b}{dt} \quad (3-6)$$

where V_{batch} [m^3] is the constant volume of the reactant solution in the batch experiment, and $\frac{dC_b}{dt}$ represents the observed differential change of the bulk concentration C_b [g m^{-3}] with time t [s] in the reactor. Eq. (3-6) assumes that for a given time t the bulk concentration is the same everywhere in the reactor due to vigorous stirring.

Assuming that concentration gradients within the catalyst layer, as well as any concentration difference between the bulk liquid and the catalyst layer's geometric surface, are negligible, the liquid phase concentration C in Eq. (3-5) equates to the bulk liquid concentration C_b in Eq. (3-6). Consequently, the observed reaction rate aligns with the intrinsic reaction rate. This premise enables the consolidation of Eq. (3-4), (3-5), and (3-6) into the subsequent Eq. (3-7):

$$\frac{dC_b}{dt} = - \frac{1}{V_{\text{batch}}} \frac{a I_0^b (1 - e^{-b\omega\delta_L})}{b\omega\delta_L} \frac{g_{\text{cat}} K_{\text{LH}} C_b}{1 + K_{\text{LH}} C_b} \quad (3-7)$$

Estimations for the constants a , b and K_{LH} were derived by fitting the solution of Equation (3-7), obtained using Matlab® ODE45 solver, against the observed concentration profiles for various catalyst layer thicknesses and initial concentrations in the batch reactor. This fitting utilized a weighted least squares method for the objective function minimization, where $RSS = \sum_i [(C_{b,\text{exp},i} - C_{b,\text{sim},i}) / \Delta C_{b,\text{exp},i}]^2$. Here, $\Delta C_{b,\text{exp},i}$ represents the measured standard error of the experimentally observed concentration $C_{b,\text{exp},i}$ at time point i (calculated from 3 replicate measurements), and $C_{b,\text{sim},i}$ denotes the simulated concentration from the model corresponding to the same time point.

Before proceeding, the nonexistence of external (film) diffusion limitations was confirmed experimentally by incrementally increasing the stirring speed in the batch reactor until no further enhancement in the reaction rate was observed (detailed results can be found in section 3.1.2). Additionally, the absence of internal (pore) diffusion limitations was validated through evaluation of the Weisz modulus. The generalized form of the Weisz modulus is presented in

Equation (3-8) [202]:

$$\psi_{WP} = \left(\frac{V_{cat}}{A_{cat.ext.}} \right)^2 \frac{n+1}{2} \frac{r_{obs-batch}}{D_{eff} C_s} \quad (3-8)$$

V_{cat} [m³] is the volume of the catalyst layer, $A_{cat.ext.}$ [m²] is the external surface area of the catalyst layer, n is the reaction order, $r_{obs-batch}$ [g s⁻¹ m⁻³] is the observed reaction rate divided by the catalyst volume, D_{eff} [m² s⁻¹] is the effective diffusion coefficient of RhB in the catalyst layer, and C_s [g m⁻³] is the mass concentration of the pollutant on the external catalyst surface. It has to be noted that a catalyst layer with thickness δ_L , accessible to the reactant only from the top surface, effectively functions like a flat catalyst plate of thickness $2\delta_L$. This is due to symmetry reasons. Consequently, for the calculation of the Weisz-Prater modulus, the ratio of catalyst volume to external catalyst area $\frac{V_{cat}}{A_{cat.ext.}}$ was substituted with $2\delta_L$.

The influence of internal diffusion on the observed reaction rate is considered negligible when the Weisz modulus does not exceed a specific threshold. This threshold signifies that the observed reaction rate diminishes by no more than 5%, compared to the conditions prevailing at the external surface due to concentration drops within the catalyst, attributed to finite diffusion rates. For a monomolecular irreversible reaction adhering to Langmuir-Hinshelwood (LH) kinetics, this critical value is tied to the product of $K_{LH}C$, essentially $K_{LH}C_b$ for batch reactor conditions as previously addressed [203]. Satterfield [204] analyzed such reactions in the context of a flat catalyst plate, offering a correlation of effectiveness factors to the Weisz modulus for varying $K_{LH}C$ values. This relationship was utilized to establish threshold values for this study, noting that smaller $K_{LH}C$ values correspond to lower threshold values.

Under this context, for all batch reactor experiments in this study, the most stringent threshold values occurred towards the end of each experiment, where concentrations were minimal. Calculated Weisz modulus values for varying catalyst layer thicknesses (ranging from 110 to 990 nm) at experiment ends consistently fell below these thresholds, a detailed discussion of which appears in Section 3.1.2.

Given these findings, it is clear that the kinetic data from the batch experiments are unaffected by pore diffusion limitations. This conclusion is particularly robust considering that, in our study, the reaction rate diminishes further within the catalyst layer due to light attenuation, which reduces the rate constant - a phenomenon not accounted for in the straightforward Weisz modulus estimation. As detailed in section 3.1.1, this light attenuation results in a further deceleration of the reaction rate deeper within the layer, whereas the rate of diffusion remains

constant.

For the microreactor working under surface-flow mode (Mode 4), the material balance for the pollutant reads:

$$\frac{dC_b}{dz} = \frac{1}{\bar{V}L_{MR}} R_{obs-PMR} \quad (3-9)$$

Pore diffusion's impact on the observed reaction rate $R_{obs-PMR}$ in the microreactor experiments can also be confidently ruled out. This is because the light intensity within the microreactor was lower than that in the batch reactor, resulting in a reduced reaction rate, while the pollutant concentration remained similar and the catalyst layer thickness was consistent at approximately 990 nm.

In the context of the microreactor experiments, the scenario for external mass transport is notably different due to the low flow velocities utilized. As a result, the observed reaction rate in the microreactor, represented by $R_{obs-PMR}$ in Eq. (3-9), cannot be straightforwardly linked to the bulk liquid concentration, C_b . Instead, it necessitates determining the unknown pollutant concentration, C_s , at the external surface of the printed catalyst layer. This determination involves balancing the diffusive flux to the layer's external surface with the consumption rate within the layer, factoring in its external surface area. The same approach was also taken, e.g., by Charles et al. [205]:

$$\beta_m(C_b - C_s) = \frac{\bar{k}g_{cat}K_{LH}C_s}{1+K_{LH}C_s} \frac{1}{A_{cat}} = \frac{\delta_L\rho_{cat}\bar{k}K_{LH}C_s}{1+K_{LH}C_s} \quad (3-10)$$

Here, β_m [$m\ s^{-1}$] is the mass transfer coefficient, A_{cat} [m^2] is the external surface area of the catalyst layer and ρ_{cat} [$g\ m^{-3}$] is the density of the TiO_2 P25 catalyst layer which is calculated in section 2.2.1. After rearranging, a quadratic equation for calculating C_s is obtained:

$$C_s^2 + \left(\frac{1}{K_{LH}} - C_b + \frac{\delta_L\rho_{cat}\bar{k}}{\beta_m} \right) C_s - \frac{C_b}{K_{LH}} = 0 \quad (3-11)$$

Eq. (3-11) has two analytical solutions, which read:

$$C_{s_{\frac{1}{2}}} = -\frac{1}{2} \left(\frac{1}{K_{LH}} - C_b + \frac{\delta_L\rho_{cat}\bar{k}}{\beta_m} \right) \pm \sqrt{\frac{1}{4} \left[\frac{1}{K_{LH}} - C_b + \frac{\delta_L\rho_{cat}\bar{k}}{\beta_m} \right]^2 + \frac{C_b}{K_{LH}}} \quad (3-12)$$

Obviously, one of the two solutions of Eq. (3-12) is negative, and hence only the positive one is meaningful, which reads:

$$C_s = -\frac{1}{2} \left(\frac{1}{K_{LH}} - C_b + \frac{\delta_L \rho_{cat} \bar{k}}{\beta_m} \right) + \sqrt{\frac{1}{4} \left[\frac{1}{K_{LH}} - C_b + \frac{\delta_L \rho_{cat} \bar{k}}{\beta_m} \right]^2 + \frac{C_b}{K_{LH}}} \quad (3-13)$$

Relating $R_{obs-PMR}$ to the surface concentration C_s transforms Eq. (3-9) into the following form:

$$\frac{dC_b}{dz} = -\frac{1}{\bar{V}L_{MR}} \frac{\bar{k}g_{cat}K_{LH}C_s}{1+K_{LH}C_s} \quad (3-14)$$

Substituting C_s from Eq. (3-13) into Eq. (3-14) eliminates the unknown surface concentration by relating it to the bulk concentration C_b and the mass transfer coefficient β_m . The mass transfer coefficient β_m can be calculated from an established empirical correlation for laminar flow in microchannels using the Sherwood number Sh , Reynolds number Re and Schmidt number Sc [206]:

$$Sh = \frac{\beta_m d_h}{D_{RhB}} = 7.54 \left(1 + 0.095 \frac{d_h}{L_{MR}} Re Sc \right)^{0.45} \quad (3-15)$$

$$Re = \frac{\bar{u} d_h}{\nu} \quad (3-16)$$

$$Sc = \frac{\nu}{D_{RhB}} \quad (3-17)$$

where d_h [m] is the hydraulic diameter of the channel, D_{RhB} [m² s⁻¹] is the binary diffusivity of the pollutant RhB in water, ν [m² s⁻¹] is the kinematic viscosity of water and \bar{u} [m s⁻¹] is the mean flow velocity in the channel.

Based on these equations (3-15) to (3-17), and the data given in Table 3-1, the mass transfer coefficient β_m can be calculated. For flow rates of 0.05, 0.1 and 0.2 ml min⁻¹ employed in this study, β_m is calculated to be 6.61×10⁻⁶, 7.40×10⁻⁶, 8.72×10⁻⁶ m s⁻¹, respectively. This finally allows to solve Eq. (14) with the Matlab® routine ODE45 to obtain the concentration profile of the pollutant along the microchannel.

Table 3-1 Parameters used for calculation of β_m . [64]

Density of water ρ	9.98×10^5	g m^{-3}
Viscosity of water μ	1.00	$\text{g s}^{-1} \text{m}^{-1}$
Volumetric flow rate \dot{V}	8.33×10^{-10}	$\text{m}^3 \text{s}^{-1}$
	1.66×10^{-9}	
	3.33×10^{-9}	
Cross-sectional area of the channel A_r	1.50×10^{-6}	m^2
Microchannel height H	3.00×10^{-4}	m
Perimeter of the channel P_C	1.06×10^{-2}	m
Hydrodynamic diameter $d_h = 4A/P_c$	5.66×10^{-4}	m

3.1.2 Assessment of the reaction kinetics

3.1.2.1 Analysis of possible mass transport limitations

The impact of external mass transport on the batch reactor experiments was checked by varying the stirring speed, as aforementioned in Section 3.1.1. Figure 3-2 illustrates that elevating the stirring speed from 200 to 400 rpm did not alter the rate of degradation over time. This observation suggests that, at the standard stirring speed of 200 rpm employed in this study, film diffusion limitation can be excluded.

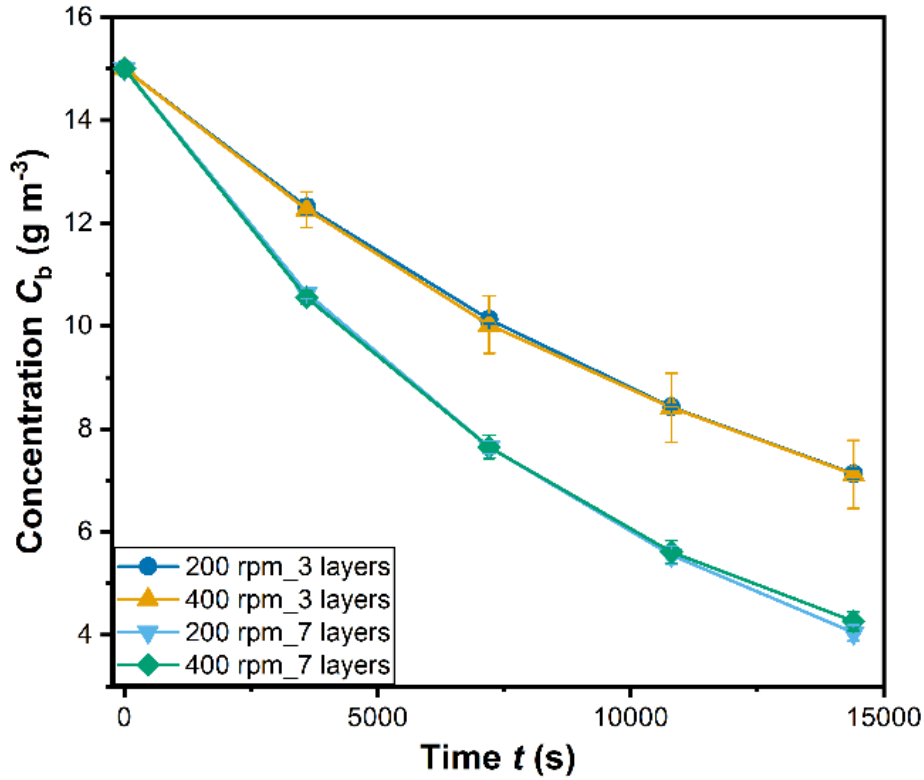


Figure 3-2 Degradation of RhB with different coating at 200 and 400 rpm stirring speed (initial concentration: 15 g m^{-3} ; symbols: mean values of 3 replicates; error bars: standard error of the mean). [64]

To assess the potential influence of pore diffusion limitations on the reaction, the Weisz-Prater criterion, as outlined in Eq. (3-8) from Section 3.1.1.2, was applied. The effective diffusivity, D_{eff} , was estimated using the equation:

$$D_{\text{eff}} = \frac{\varepsilon D_{\text{RhB}}}{\tau} \quad (3-18)$$

where D_{RhB} represents the diffusion coefficient of the pollutant RhB in water, ε is the porosity and τ is the tortuosity factor. The porosity value of 0.69, derived from the catalyst layer's characterization, along with a tortuosity factor τ of 3 and $D_{\text{RhB}} = 4.27 \times 10^{-10} \text{ m}^2 \text{ s}^{-1}$ from literature [207, 208], were utilized for this evaluation. The Weisz modulus for different catalyst layer thicknesses towards the end of the experiments was calculated, where the lowest concentration and limiting values are expected, as per the methodology detailed in Section 3.1.1.2 and presented in Table 3-2. The limiting values for various $K_{\text{LH}}C$ values were determined following Satterfield's analysis [203, 204], adopting a K_{LH} of $0.14 \text{ m}^3 \text{ g}^{-1}$ derived from curve fitting as will be described in Section 3.1.2.2. The observed reaction rates needed for calculating the Weisz modulus Ψ_{WP} were determined from the degradation curves obtained through experimental data fitting, as depicted in Figure 3-4.

Table 3-2 Calculated Weisz modulus and limiting values for different layer thickness at the end of each experiment. [64]

Thickness (nm)	Limiting value	Ψ_{WP}
110	0.40	0.002
330	0.34	0.021
550	0.31	0.056
770	0.28	0.103
990	0.25	0.153

It can be seen that all the values of Ψ_{WP} are lower than their corresponding limiting values. This indicates that internal mass transport limitations can be neglected.

3.1.2.2 Determination of the kinetic parameters

First, to determine the extinction coefficient ω in Eq. (3-3), the measured transmission T_L for different layer thickness was used, as shown in Figure 3-3. By employing a linear least square fitting, a value of $4.38 \times 10^6 \text{ m}^{-1}$ was obtained for ω .

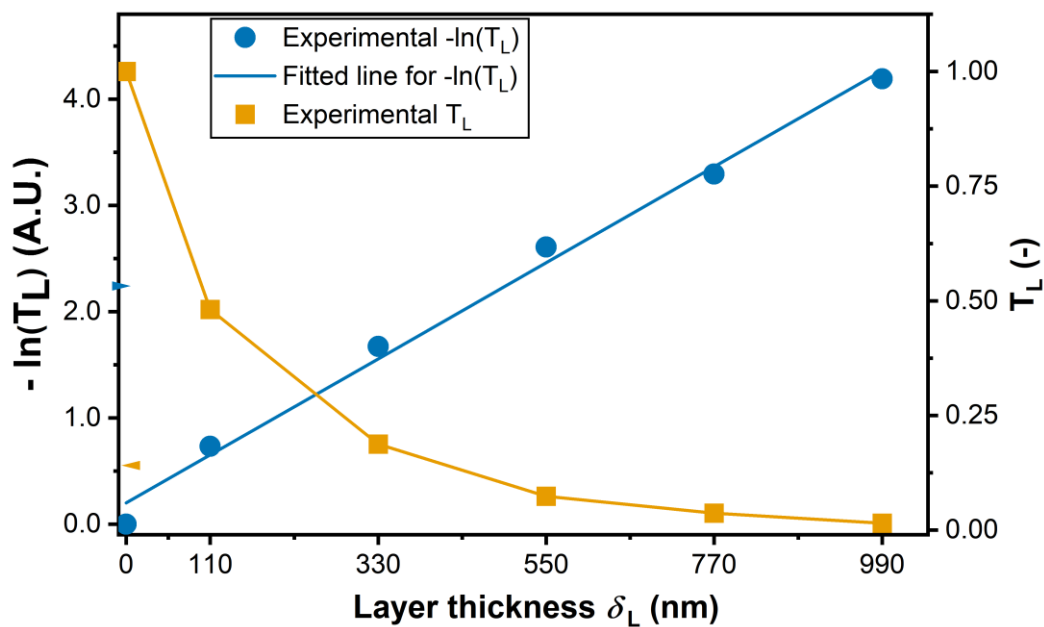


Figure 3-3 Experimental data and fitting of measured transmission T_L and $-\ln(T_L)$ versus layer thickness for determining the extinction coefficient ω . [64]

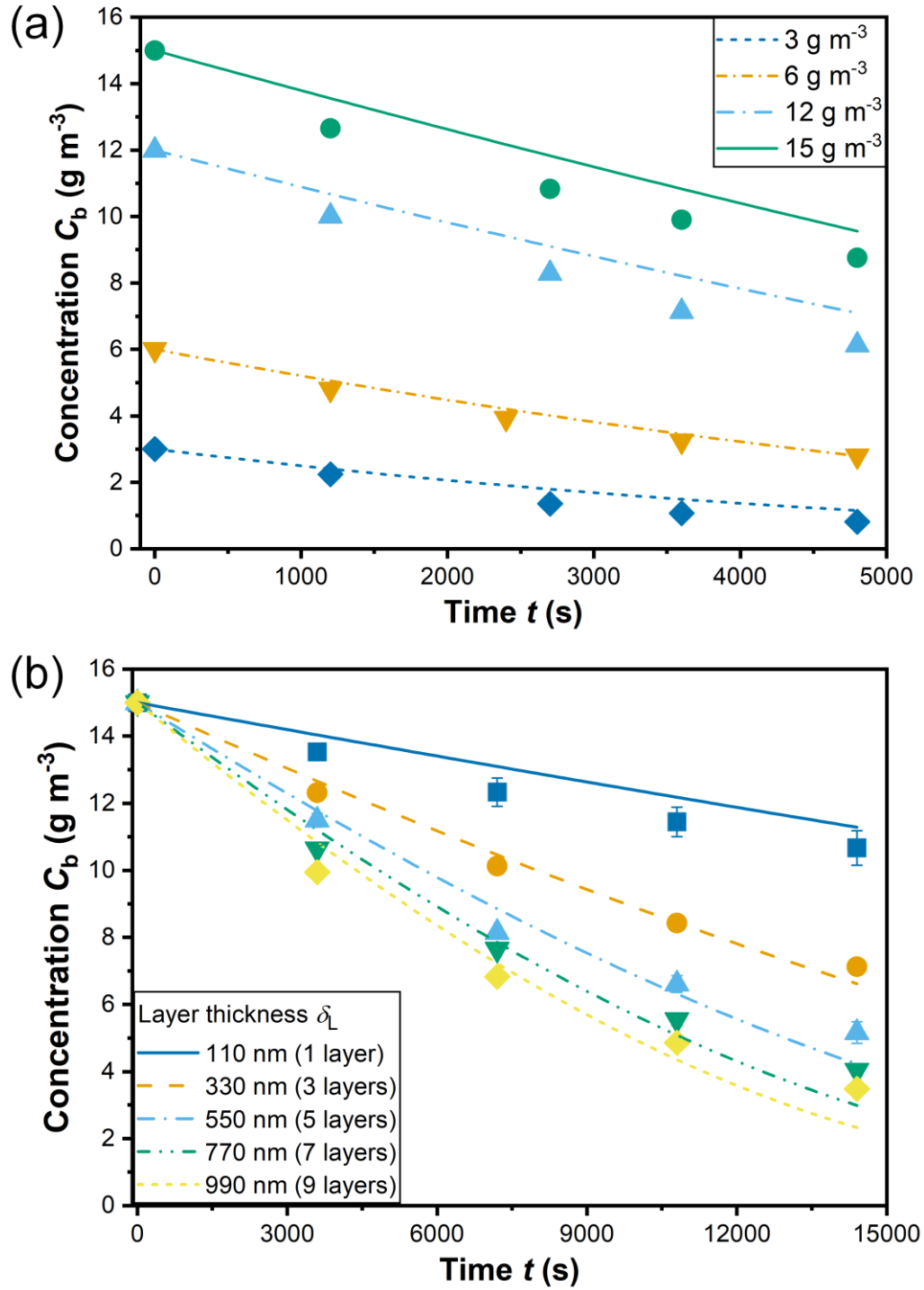


Figure 3-4 Degradation with (a) 9-layer coating (990 nm thickness) at different initial concentrations; (b) coatings of different thickness (symbols: mean values of measured data of $n \geq 3$ replicates; error bars: standard error of the mean; lines: fitting). [64]

Figure 3-4 presents experimental data depicting the degradation performance of a 9-layer coating ($\delta_L = 990$ nm) across initial concentrations ranging from 3 to 15 g m⁻³, and for coatings of various thicknesses at a fixed initial concentration of 15 g m⁻³. A non-linear fitting approach, in line with Eq. (3-7), was employed to derive the kinetic parameters based on these 9 data sets,

which encompass different layer thicknesses and initial concentration levels. This comprehensive analysis aimed to simultaneously estimate the kinetic parameters a , b , and K_{LH} for all variations depicted in Figure 3-4. Although the model slightly underpredicts reaction rates at higher layer thicknesses and initial concentrations, the overall fit is deemed acceptable, particularly when considering the confidence intervals and correlation coefficients associated with the parameter estimates.

The model's fitting to the experimental data is illustrated in Figure 3-4, with kinetic parameters and their confidence intervals at a 95% confidence level detailed in Table 3-3. Analysis of the correlation matrix (Table 3-4) and the joint confidence region plots (Figure 3-5) for parameter pairs (a and b , as well as K_{LH} and b) indicates a moderate correlation between these parameter pairs. However, a notable negative correlation exists between K_{LH} and a , which can be traced back to the dependency of the reaction rate on those two parameters. Note that combining Eq. (3-4) and (3-5) yields:

$$r = \frac{aI_0^b(1-e^{-b\omega\delta_L})}{b\omega\delta_L} \frac{g_{cat}K_{LH}C}{1+K_{LH}C} \quad (3-19)$$

where a and K_{LH} appear in the numerator as a product, and,

$$r \sim \frac{aK_{LH}C}{1+K_{LH}C} \quad (3-20)$$

Hence, for small values of C , the denominator approaches unity and r is both proportional to a and K_{LH} . This means that only the product $a \cdot K_{LH}$ is well defined, but not the individual values of a and K_{LH} . Fortunately, for higher concentrations, the denominator significantly differs from unity, and this in the end still allows the estimation of both a and K_{LH} with acceptable precision, as signified by the confidence intervals reported in Table 3-3.

Table 3-3 Kinetic parameter estimates determined from a non-linear fitting to the experimental data. [64]

	Value	Confidence interval at confidence level of 0.95
a [g cm ^{0.86} g ⁻¹ s ⁻¹ mW ^{-0.43}]	4.01×10^{-5}	7.09×10^{-7}
b [-]	0.43	0.013
K_{LH} [m ³ g ⁻¹]	0.14	0.005

Table 3-4 Correlation matrix of the determined kinetic parameter estimates. [64]

	a	b	K_{LH}
a	1.00	-0.48	-0.98
b	0	1.00	0.51
K_{LH}	0	0	1.00

The adsorption equilibrium constant K_{LH} was determined to be $0.14 \text{ m}^3 \text{ g}^{-1}$. A large number of studies from literature describe the photocatalytic degradation with a pseudo first-order kinetic model assuming that $K_{\text{LH}}C \ll 1$ [61, 121, 163]. However, for the present study, the term $K_{\text{LH}}C$ is close to or even larger than 1, which obviously cannot be neglected.

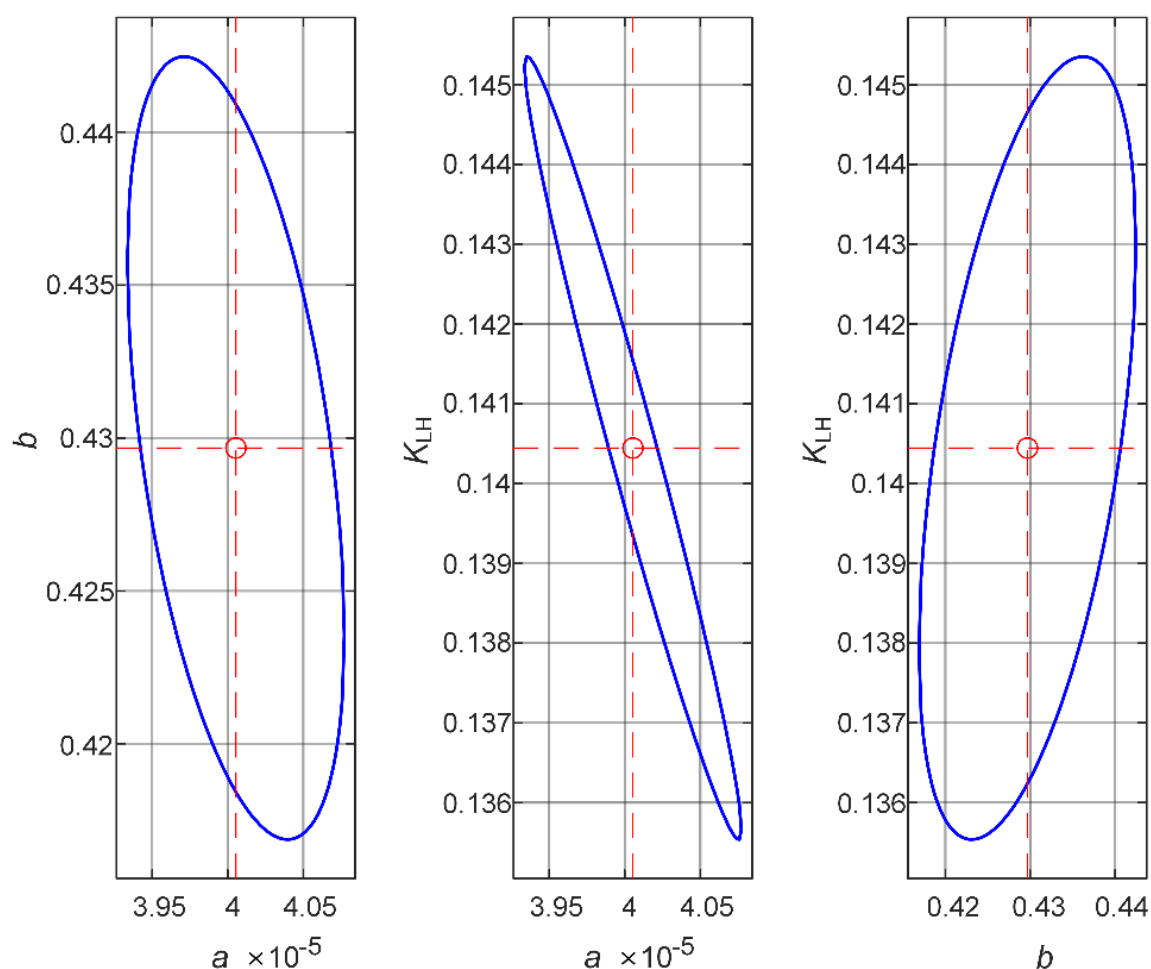


Figure 3-5 Ellipse plot showing the pairwise joint confidence regions of parameter estimates a , b and K_{LH} (units not shown). [64]

3.1.2.3 Kinetic performance in the microreactor under surface-flow

The kinetic model established from the batch experiments was applied to evaluate the continuous-flow μ PMR experiments conducted in surface-flow (Mode 4). To determine the pollutant RhB's conversion rate X_{re} [%], Equation (2-8), detailed in Section 2.3.1.6, was utilized. Within the context of surface-flow mode, where there is a single inlet and outlet leading to $\dot{V}_0 = \dot{V}_1$, the degree of removal, namely, conversion X_{re} is determined as outlined in Eq. (3-21):

$$X_{re} = \frac{\dot{V}_0 \cdot C_0 - \dot{V}_1 \cdot C_1}{\dot{V}_0 \cdot C_0} \times 100 = \frac{C_0 - C_1}{C_0} \times 100 \quad (3-21)$$

Here, C_0 is the inlet concentration and C_1 is the measured outlet concentration.

Figure 3-6 showcases the variation in outlet concentration over time for three different sets of operational conditions. As demonstrated in Figure 3-6 (a), keeping flow rate (0.05 mL min^{-1}) and light intensity (1.5 mW cm^{-2}) constant, a higher conversion was achieved at lower initial concentrations of 3 g m^{-3} as compared to that of 15 g m^{-3} . The system requires an initial stabilization period of approximately 220 min after illumination onset to reach steady-state operation (defined as outlet concentration fluctuations within $\pm 5\%$ over three consecutive 30-minute samples). This corresponds to a cumulative volume displacement of 11 mL (calculated as flow rate \times stabilization time). Figure 3-6 (b) highlights the system's operational stability at 0.2 mL min^{-1} , showing a sustained plateau in outlet concentration for over 3 hours following a shorter stabilization period of 30 minutes after illumination was on, corresponding to a cumulative volume displacement of 6 mL

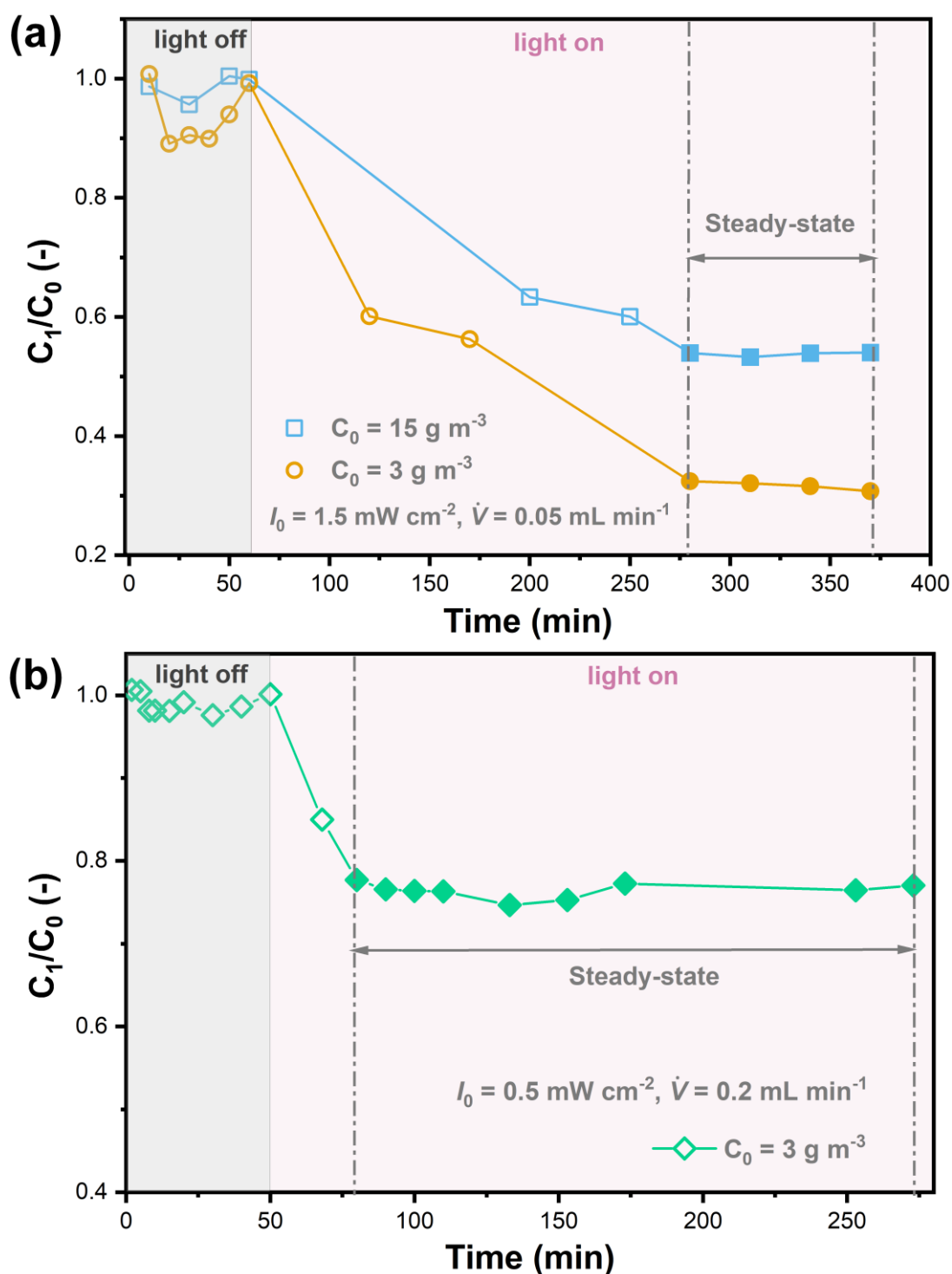


Figure 3-6 An exemplary display of the outlet concentration in the microreactor for 3 different data series (filled symbols represent the points used for data evaluation where steady-state can be assumed) with 2 volumetric flow rate: (a) 0.05 mL min^{-1} ; (b) 0.2 mL min^{-1} . [64]

Table 3-5 systematically summarizes the effects of varying operational parameters (e.g., flow rate, light intensity, initial concentration) on degradation performance. All reported data were collected during steady-state operation, with sampling initiated only after meeting the stabilization criterion: three consecutive outlet concentration measurements (taken at 30-minute

intervals) deviating by $\leq 5\%$.

Table 3-5 Degree of removal in the microreactor by varying the light intensity I_0 (mW cm^{-2}), inlet concentration C_0 (g m^{-3}) and flow rate \dot{V} (mL min^{-1}). [64]

	$C_0 = 15$		$C_0 = 3$	
	$I_0 = 0.5$	$I_0 = 1.5$	$I_0 = 0.5$	$I_0 = 1.5$
$\dot{V} = 0.05$	34	47	60	71
$\dot{V} = 0.1$	21	32	40	53
$\dot{V} = 0.2$	12	20	23	35

Section 3.1.1.2 clarified that internal diffusion limitation was not a factor for the microreactor experiments, as determined by the assessment of the Weisz modulus. However, external mass transport was explicitly accounted for in the model equations (3-13) to (3-17), enabling accurate simulation of degradation in the microreactor.

Figure 3-7 (a) illustrates the simulated profiles of the bulk concentration C_b and the concentration at the external surface of the catalyst layer C_s for a representative experiment. The results reveal a moderate effect of external mass transport, with C_s approximately 10% lower than C_b at the inlet and up to 12% lower at the outlet. As described by Eq. (3-20), the reaction rate r is directly governed by the local surface concentration. Accordingly, this 10–12% difference between C_b and C_s translates to a comparable deviation in the local reaction rate, underscoring the non-negligible role of external mass transport under the studied conditions.

A comparison of predicted conversions against experimental outcomes, presented in a parity plot (Figure 3-7 (b)), shows all data points within a $\pm 20\%$ margin. This level of agreement is generally regarded as satisfactory in complex catalytic reactor studies and indicates that the model reliably captures the key kinetics and transport phenomena.

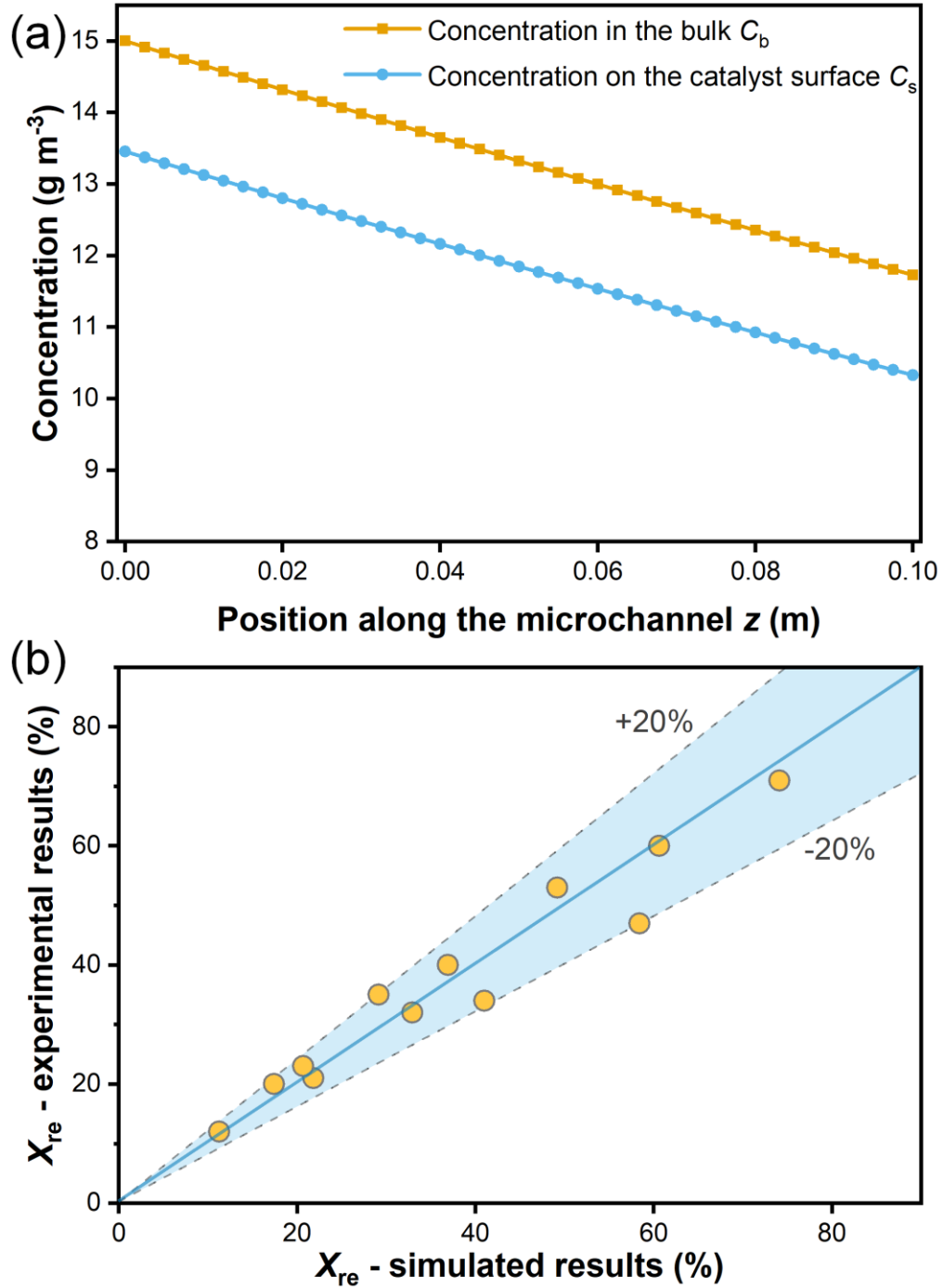


Figure 3-7 (a) Illustration of the bulk concentration C_b and concentration at the external surface of the catalyst layer C_s along the microchannel (experimental condition: $C_0 = 15 \text{ g m}^{-3}$, $I_0 = 0.5 \text{ mW cm}^{-2}$, $\dot{V} = 0.1 \text{ mL min}^{-1}$); (b) comparison of the simulation and experimental results in a parity plot for the microreactor experiment.

3.1.3 Discussion

This section presents a kinetic analysis of RhB degradation, employing a Langmuir-Hinshelwood kinetic model that accounts for light attenuation within the catalyst layer. The model effectively describes the batch reactor experimental data, establishing parameter

estimates for kinetic constants while ruling out external and internal mass transport limitations. The obtained estimates therefore characterize the intrinsic chemical kinetics. Validating this kinetic model using the continuous-flow μ PMR in surface-flow mode showed a strong agreement between simulated and experimental data, affirming that reaction kinetics remain consistent across different reactor setups when the analysis is meticulously conducted.

This work offers a robust framework for kinetic studies in photocatalytic degradation, using RhB as a representative pollutant. While the study focuses on a single pollutant in water, applying this approach to other pollutants or complex mixtures may introduce additional complexities in mass transport and reaction kinetics modeling. Nonetheless, with careful modeling that encompasses all critical effects and experiments conducted under well-defined conditions, the insights gained here should be applicable to other systems, facilitating their scale-up and broader application.

3.2 Study on process enhancement in μ PMR and practical application

This section showcases the capabilities of the μ PMR, designed to operate under well-defined conditions. The focus is on delving into the exploration of the μ PMR's versatility by transitioning from batch and surface-flow modes of last Section 3.1, to a broader range of flow modes, with a primary emphasis on studying the process enhancement. This involves a detailed investigation into the effects of mass transport and the synergistic interaction between membrane filtration and photocatalysis on the photodegradation process. Additionally, the role of light intensity in boosting photodegradation is examined using the established light model. Rhodamine B (RhB) and Rose Bengal (RB) serve as model pollutants for these studies.

To demonstrate the μ PMR's practicality, its application to the photodegradation of several micropollutants, including Carbamazepine (CBZ), Sulfamethoxazole (SMX), and Bezafibrate (BZF) is extended using selected flow modes. Lastly, an examination of degradation under real sunlight conditions is presented, highlighting the practical applicability of the system.

3.2.1 Flow mode comparison

The study of RhB photodegradation across four specific flow modes showed varying efficiencies, as detailed in Figure 3-8. This illustration shows the percentage of RhB removed over 150 minutes. All modes achieved a steady state, as corroborated by a consistent material balance established by monitoring the mass flow of the inlet, permeate, and retentate (Figure C 1), which is prerequisite for the following studies.

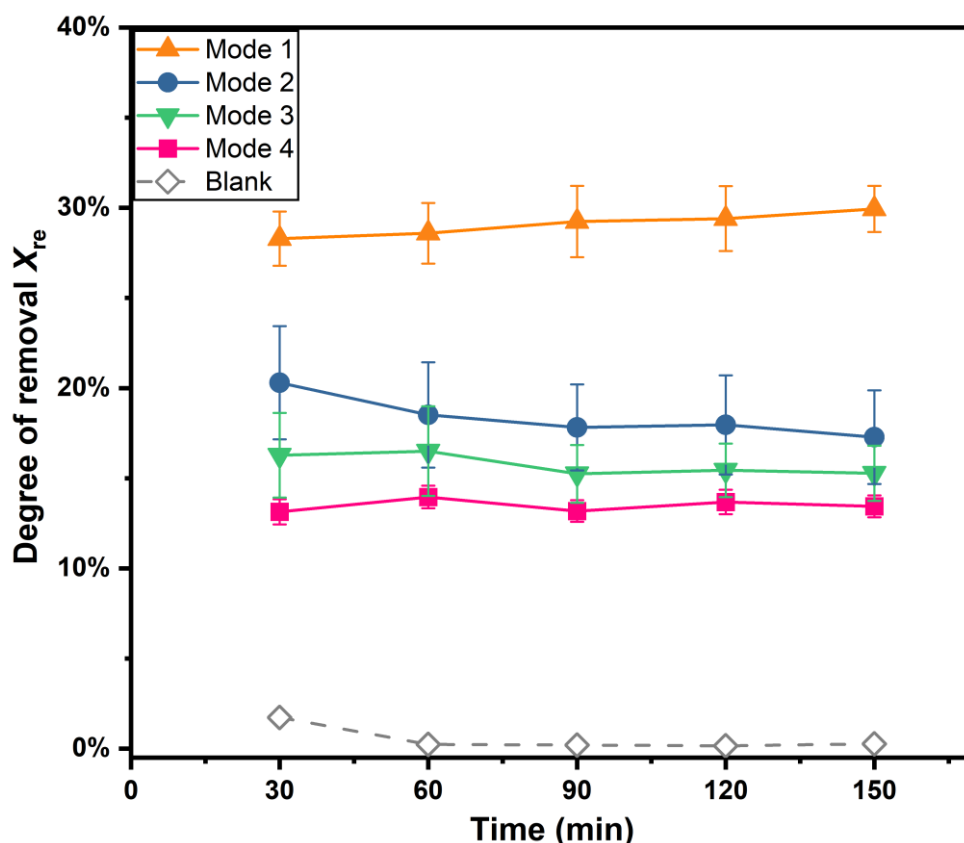


Figure 3-8 Removal of RhB under different flow modes. For Mode 1, 2 and 4, X_{re} denotes the photodegradation. For Mode 3, X_{re} denotes the membrane rejection. Experimental conditions: inlet concentration: 15 mg L^{-1} ; inlet flow rate for all flow modes and blank: 0.2 mL min^{-1} ; UV light intensity (Mode 1, 2, 4 and blank): 1 mW cm^{-2} ; split between permeate and retentate volume flow rate for Mode 1 was 2:1 under transmembrane pressure of $0.5 \pm 0.1 \text{ bar}$; transmembrane pressure for Mode 3: 10 bar ; blank tests were conducted under Mode 4 using a metal plate instead of a coated membrane. Error bars: standard error of the mean. [50]

Photolysis-induced degradation was shown to be minimal, as evidenced by a blank test. The mixed flow-through mode (Mode 1) achieved the highest removal, reaching approximately 30%, with the oxygen distributor mode (Mode 2) close behind at about 18%. In comparison, both nanofiltration (Mode 3) and pure surface-flow (Mode 4) showed nearly the same degree of removal, ranging between 13-15%. Note that in Mode 3 the pollutants are not degraded (as light was not on) but only concentrated in the retentate which has to be subsequently treated.

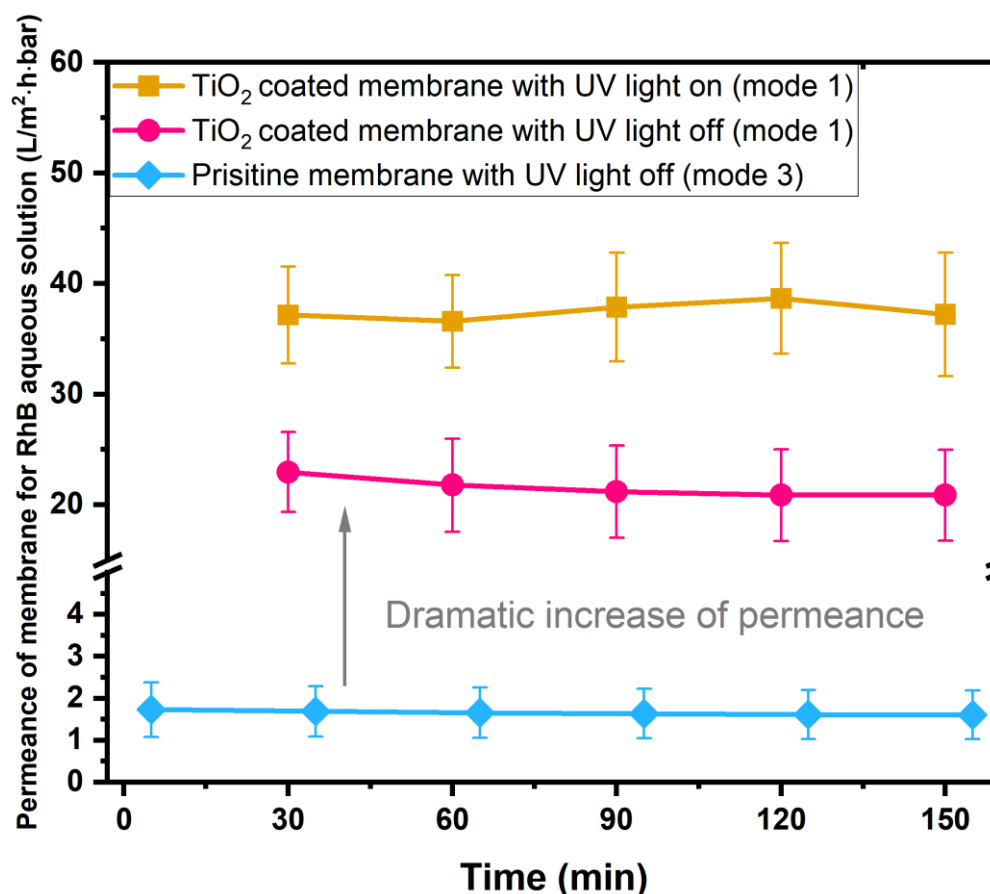


Figure 3-9 Membrane permeance for RhB aqueous solution under Mode 1 and 3. [50]

Mode 1 outperformed nanofiltration by the pristine ceramic membrane (Mode 3), suggesting that the integration of photocatalysis with nanofiltration can significantly boost the effectiveness of pollutant removal performance. This finding is further evaluated in the subsequent sections.

The enhanced performance of Mode 1 becomes even more evident when considering the increase in membrane permeation flux at constant differential pressure, as shown in Figure 3-9. Contrary to expectations that adding an additional layer to the membrane would decrease its permeance, an increase was observed instead. The formation of larger cracks on the membrane surface, which could have occurred during the application of the photocatalyst layer, was ruled out through extensive characterizations (see Appendix Section D). The increase of permeance may be attributed to the improved wettability of the membrane surface, as a result of the hydrophilic and porous nature of the TiO₂ coating [209], or to a decrease in nanofiltration layer blockage due to pollutant degradation, or potentially a combination of these factors. As demonstrated in Figure 3-9, the hydrophilicity of TiO₂ is enhanced under UV illumination, which in turn increases the membrane's surface wettability and water permeance, as corroborated by multiple studies [210-212]. Nonetheless, a definitive explanation for the

observed increase in water permeance with photocatalytically active TiO_2 coating under light exposure remains elusive, indicating the need for further investigations.

Mode 2, where oxygen gas was introduced directly via the membrane to the bottom of the catalyst layer along the microchannel, and Mode 4, where the oxygen and water were co-fed to the inlet, had an extent of removal of around 20% and 15%, respectively. However, the slight advantage of Mode 2 can be explained by an enriched local oxygen concentration near the catalyst's active sites. Oxygen acts as an electron scavenger to enhance the generation of powerful oxidizing species, such as hydroxyl radicals, as reported elsewhere [25].

3.2.2 Process intensification – evaluation of mass transport, synergistic effect of filtration and degradation, and light intensity

3.2.2.1 Evaluation of mass transport

This section delves deeper into the characteristics of the μPMR in the preferred Mode 1, focusing on identifying performance-limiting factors. The impacts of inlet flow rate and transmembrane pressure on the observed reaction rate were investigated while keeping all other operational parameters constant. Figure 3-10 (a) displays the observed reaction rate, $R_{\text{obs-PMR}}$, as a function of the inlet flow rate at constant permeate flow rate. Figure 3-10 (b) illustrates the observed reaction rate and the degree of removal as functions of the transmembrane pressure at the constant inlet flow rate. Notably, higher transmembrane pressure correlates with increased permeate flow, as shown in Figure 3-11. This indicates that the transmembrane flux is crucial for high performance, whereas the inlet flow rate is less influential. Surface-flow mode is shown to be less effective than through-flow mode because pollutants must diffuse from the center of the microchannel to the external surface of the catalyst layer in surface-flow, while convective flow in through-flow mode significantly enhances pollutant supply to the photocatalyst.

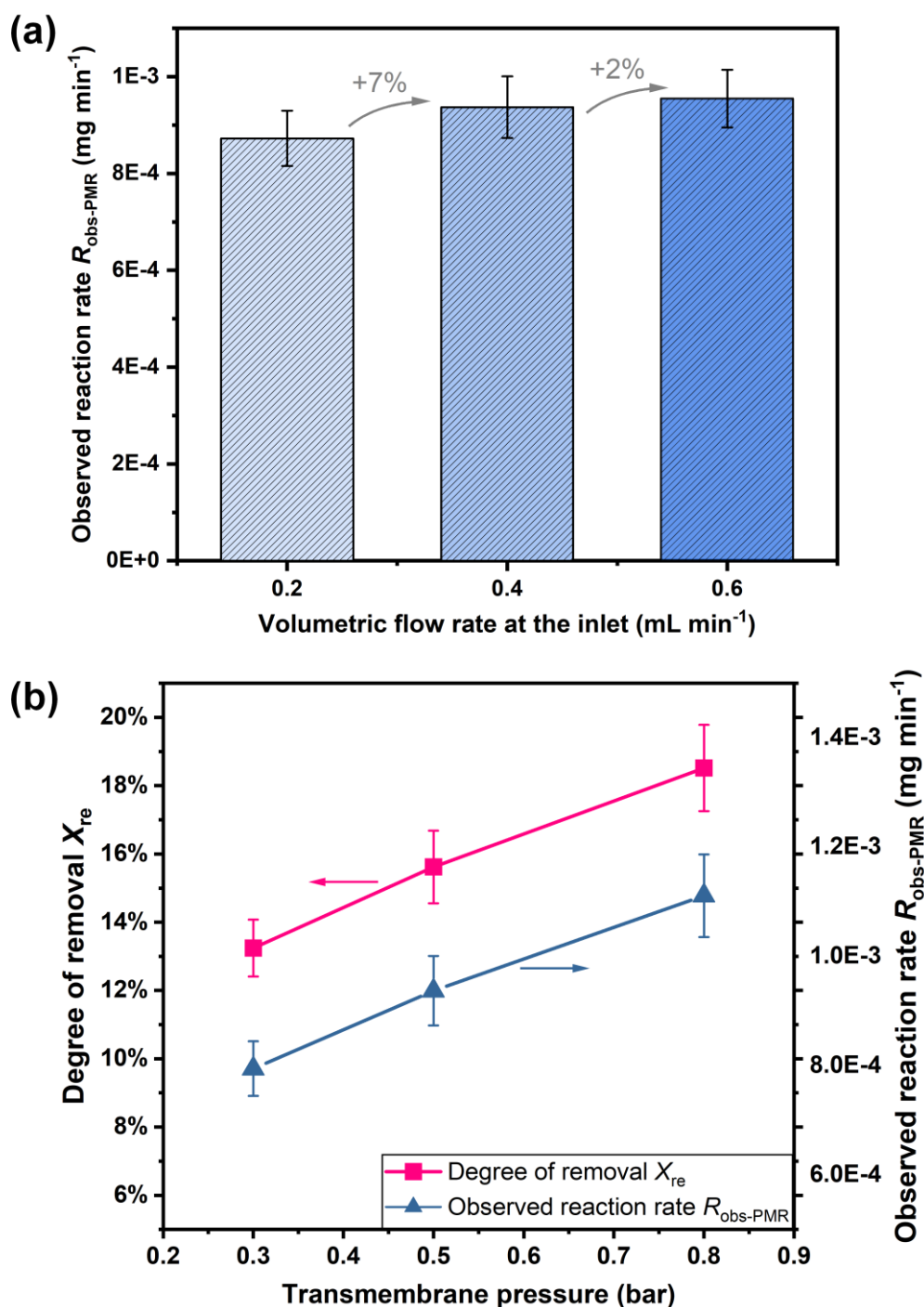


Figure 3-10 Degradation of RhB by varying the inlet flow rate and transmembrane pressure: (a) observed reaction rate of photodegradation at 3 different volumetric feed flow rates; (b) degree of removal and observed reaction rate by photodegradation at 3 different transmembrane pressures. Experimental conditions: membrane type: Membrane 2; inlet concentration: 15 mg L⁻¹; UV light intensity: 1 mW cm⁻²; transmembrane pressure for inlet flow variation experiments was 0.5 ± 0.1 bar to maintain the permeate flow at 0.13 mL min⁻¹; inlet flow rate for transmembrane pressure variation experiments: 0.4 mL min⁻¹; Error bars: standard error of the mean. [50]

The slight increase in the observed reaction rate with higher inlet flow rates is attributed to reduced pollutant depletion in the liquid traveling along the catalyst layer's external surface or to faster external mass transport from the bulk flow in the microchannel to the catalyst layer, or a combination of both. Doubling the inlet flow rate resulted in a 7% increase in reaction rate, and tripling it led to only a 9% increase, suggesting a nearing limit, likely due to the negligible decrease in pollutant concentration from inlet to outlet (retentate). A further increase in the inlet flow rate thus appears ineffective in enhancing the reaction rate. This interpretation is supported by adequate mass transfer at the lowest tested inlet flow rate of 0.4 mL min^{-1} , corroborated by pollutant concentration measurements in the retentate across different flow rates, as documented in Figure 3-12. This inlet flow rate was used for the following experiment.

Experiments with transmembrane pressures rising from 0.3 to 0.8 bar, conducted at an inlet flow rate of 0.4 mL min^{-1} , revealed a linear increase in transmembrane flux with pressure. Unlike in Figure 3-10 (a), the nonlinear response of the observed reaction rate and degree of removal suggest that higher transmembrane pressures could significantly boost reactor performance. The enhanced degree of removal is explained by a greater fraction of inlet flow passing through the catalyst-coated membrane, facilitating photodegradation. Convective transport is more effective than molecular diffusion alone, enhancing both the reaction rate and pollutant removal. With further increases in transmembrane flow, the reaction rate is expected to reach an upper limit once the change in pollutant concentration across the catalyst layer is minimal unless pollutant accumulation due to preferential permeation of water ("concentration polarization") continues to raise the degradation rate.

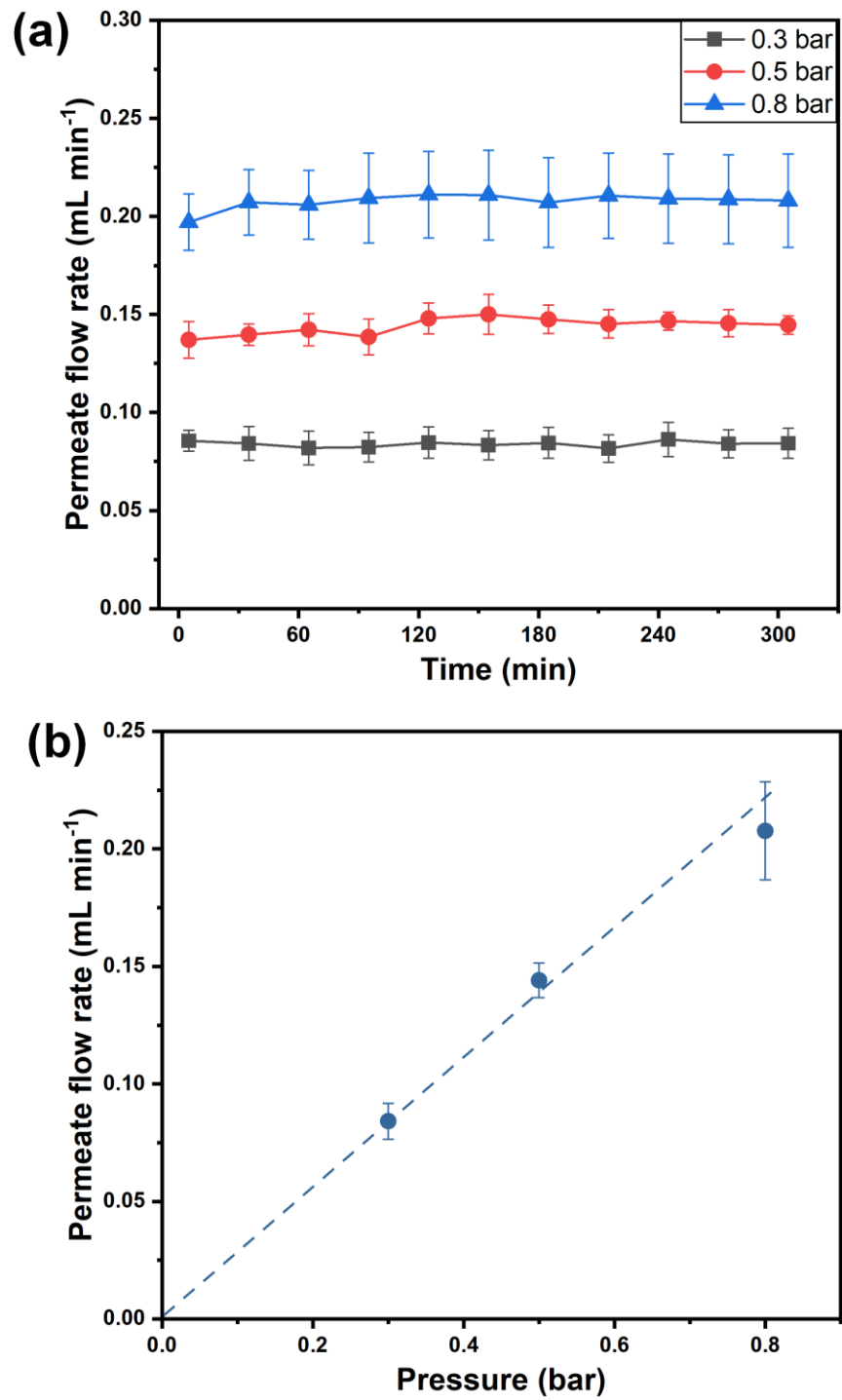


Figure 3-11 (a) Permeate flow rate versus time for various transmembrane pressures; (b) average permeate flow versus transmembrane pressure with a linear fit. [50]

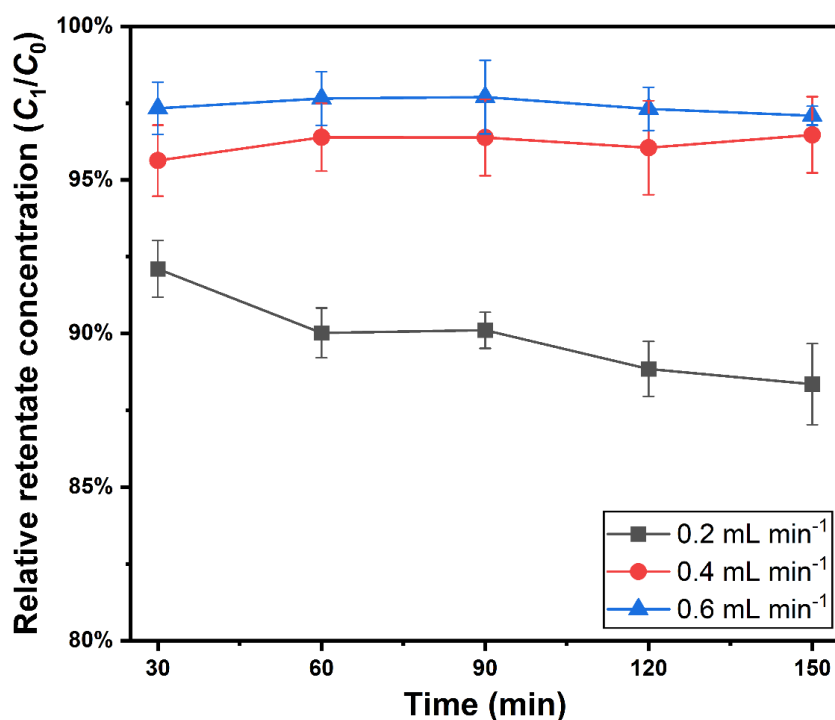


Figure 3-12 Relative retentate concentration versus time. [50]

Conversely, the degree of removal is anticipated to peak and then decline, influenced by the kinetics of photodegradation, as it relates the degraded pollutant amount to the inlet flow-supplied pollutant, given the finite reaction rate for a set catalyst mass. The borderline case would be to close the retentate outlet completely and operate the system in dead-end mode (Figure 3-13). In this case, the maximum of the degree of removal is expected to shift to a rather small value of the transmembrane flux where the convective transport would deliver a sufficient amount of pollutant to the catalyst in order to overcome mass transport limitation.

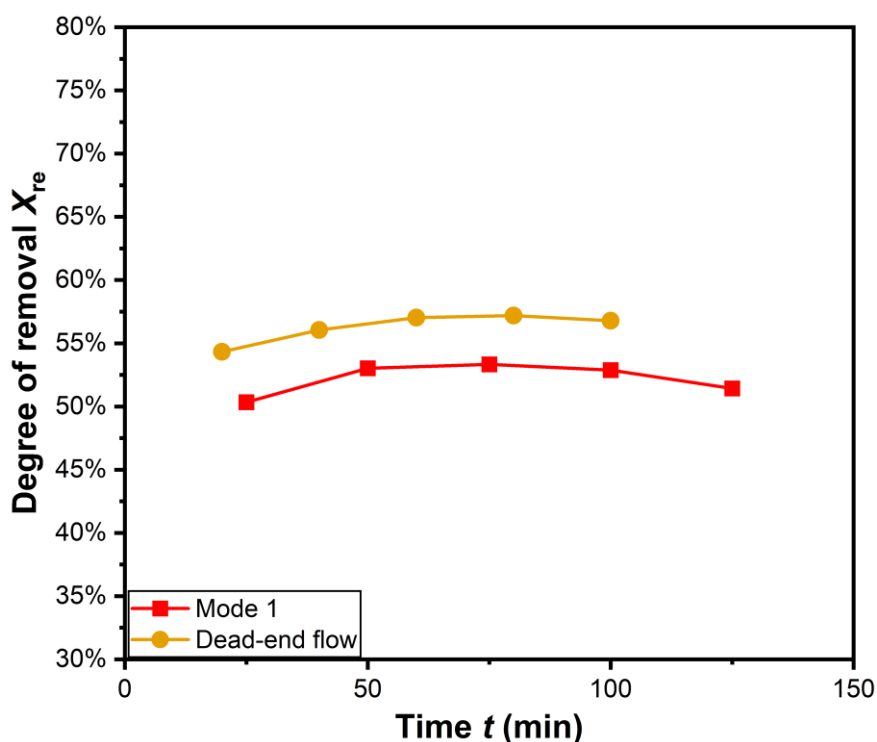


Figure 3-13 Decolorization of RhB under cross-flow (Mode 1) and dead-end flow. Experimental conditions: inlet flow rate: 0.2 mL min^{-1} ; light intensity: UV light, 2 mW cm^{-2} ; split between permeate and retentate volume flow rate for cross-flow: ca. 2:1 (Mode 1). [50]

3.2.2.2 Evaluation of synergistic effect of filtration and degradation

There is a hypothesis suggesting that filtration-induced concentration polarization could enhance the local reaction rate, given that the reaction rate is also concentration-dependent as outlined in Section 3.1.1. This potential synergistic effect between nanofiltration and photodegradation warrants further exploration.

Due to the experimental challenges associated with directly measuring pollutant concentrations above the catalyst-coated membrane surface, an indirect method was utilized to investigate this phenomenon. Specifically, ceramic NF membranes with varying MWCO values, which exhibit different pollutant rejection rates α_{mem} (Eq. (2-9)), were coated with a photocatalyst and subjected to experimental testing. For this study, Rose Bengal (RB) was selected as the model pollutant because its higher molecular weight leads to more significant and MWCO-sensitive rejection by NF membranes. Consequently, a more pronounced concentration polarization effect is expected.

Figure 3-14 shows a notable increase in the rejection rate α_{mem} for coated membranes as the MWCO of the membranes decreases from 750 Da to 250 Da, jumping from 58% to 86%. This

observation aligns with the nearly identical rejection rates seen with pristine membranes, as outlined in Table 3-6. Importantly, a direct relationship between the degree of removal X_{re} and the membrane's rejection rate α_{mem} was identified, as X_{re} increased from 61% to 76%. This relationship highlights that as the membrane increasingly rejects the pollutant, concentration polarization at the membrane surface becomes more pronounced, potentially boosting the rate of photodegradation occurring near or within the catalyst-coated membrane layer due to the increased local concentration. This observation supports the hypothesis that concentration polarization can significantly enhance the overall photodegradation efficiency.

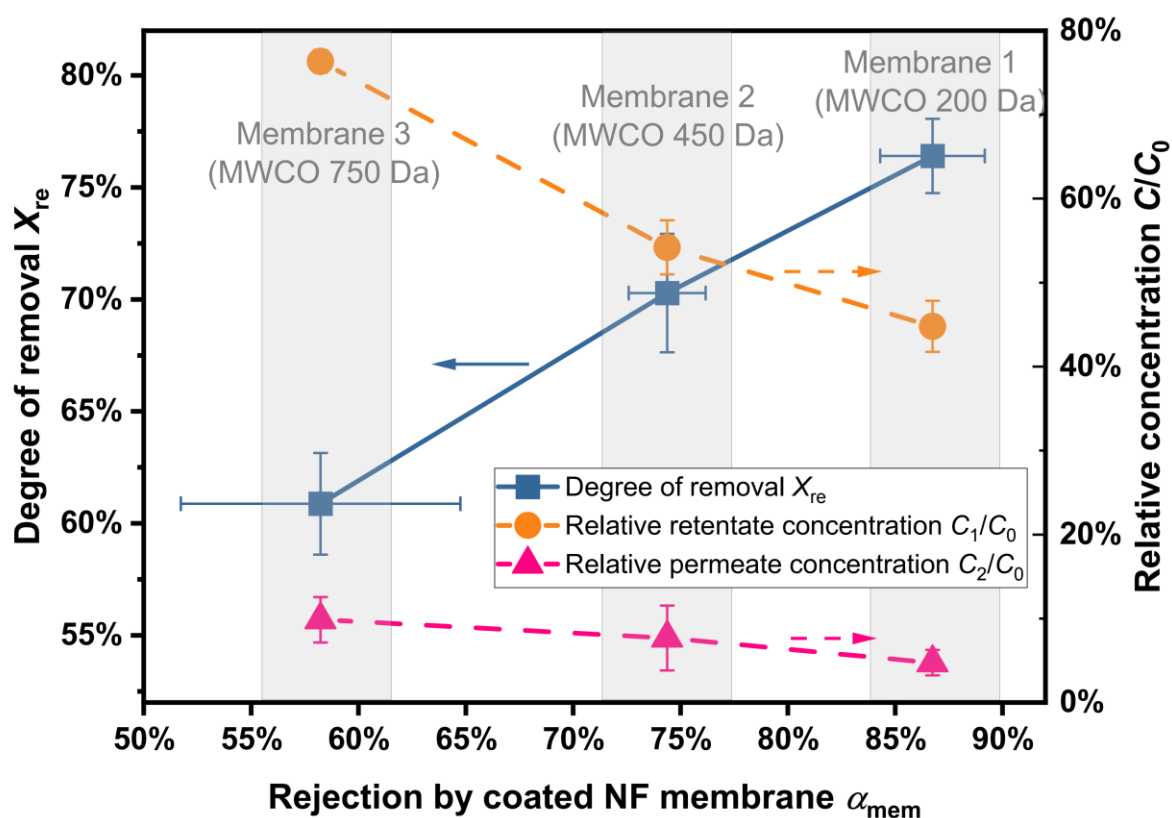


Figure 3-14 Correlation between the rejection α_{mem} with catalyst-coated NF membranes (under Mode 3) and the degree of removal X_{re} of RB (under Mode 1). Experimental conditions: inlet concentration: 15 mg L⁻¹; inlet flow rate: 0.2 mL min⁻¹; light intensity: 2 mW cm⁻²; permeate flow was kept at 0.1 mL min⁻¹ for both Mode 1 and 3; each test was conducted first through a NF rejection test without light, followed by a photo-degradation test under UV light, while keeping the membrane unchanged. Error bars: standard error of the mean. [50]

Table 3-6 Rejection α_{mem} (%) of RB by 3 NF membranes before and after coating TiO_2 .
Error: standard error of the mean. [50]

	Membrane 1 (MWCO 200 Da)	Membrane 2 (MWCO 450 Da)	Membrane 3 (MWCO 750 Da)
Pristine	88.3 ± 6.5	75.1 ± 4.8	63.2 ± 3.3
Coated	86.0 ± 3.1	74.4 ± 1.8	58.2 ± 6.5

Considering the involvement of three different membrane types in this study, it is important to consider the potential charge repulsion effect. This factor could also contribute to the observed variation in both membrane rejection and degree of removal of RB by photodegradation. Zeta-potential measurements indicated near-identical values of -60 mV for both pristine and catalyst-coated surfaces of Membrane 2 at the experimental pH of 8.1, as seen in Figure 3-15. Given that Membranes 1 and 3 were fabricated using the same materials and processes as Membrane 2 (detailed by the manufacturer, Inopor), and that all three membranes were coated with the same TiO_2 P25 catalyst, it is expected that the type of membrane or coated catalyst doesn't contribute to differences in charge effects. Notably, with RB's pKa values of 3.93 and 1.89 [198], the negatively charged membranes and coatings are expected to enhance the rejection of negatively charged RB at the experimental pH due to the charge repulsion effect.

Given that the inlet and permeate flow rates were maintained at 0.2 and 0.1 mL min^{-1} respectively for all experiments, it can be assumed that comparable flow conditions existed. Furthermore, with light intensity and the catalyst layer being consistent across tests, the core conditions driving the intrinsic reactions remained unchanged. These factors collectively strengthen the hypothesis that polarization-induced reaction enhancement plays a significant role. Deba et al. have recently developed a one-dimensional model to forecast the overall photocatalytic removal of MB in a dead-end flow mode [28]. This model, integrating membrane retention with reaction kinetics, suggested that retention can markedly boost MB removal, especially in slower reactions. While these simulation results require further empirical validation, they align with and reinforce our hypothesis.

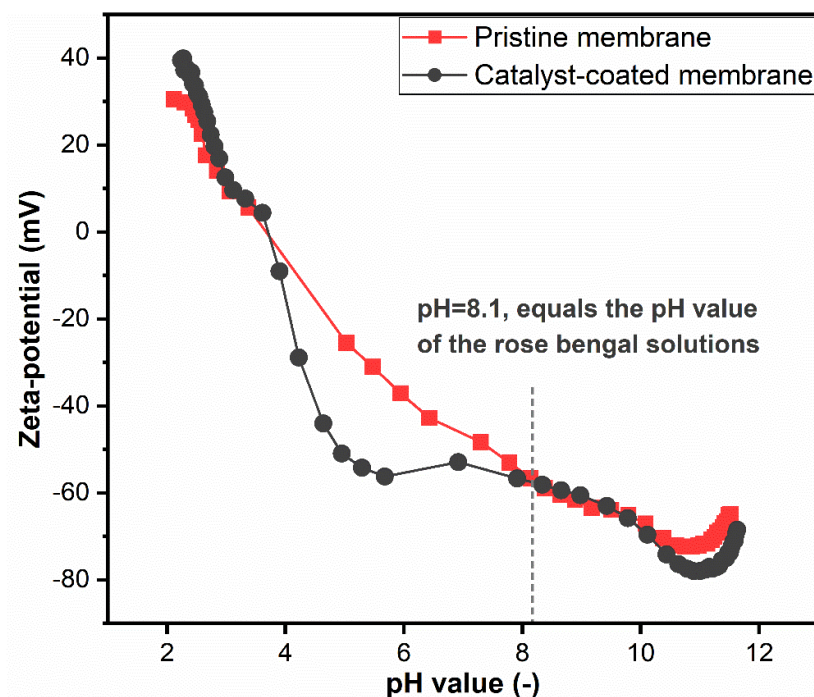


Figure 3-15 Surface charge (zeta-potential) of pristine and catalyst-coated membranes (Membrane 2, MWCO 450 Da) in 1 mM KCl solution, pH adjusted with 0.05 M HCl and 0.05 M NaOH. [50]

3.2.2.3 Evaluation of light intensity

In addition to potential mass transport limitations, the observed reaction rate is also influenced by the incident light intensity, catalyst layer thickness, and mass of catalyst. In this work, the impact of light intensity was investigated particularly. As depicted in Figure 3-16, X_{re} increased from 12 to 18% as the light intensity went from 0.5 to 1.5 mW cm⁻².

It is worth noting that the observed reaction rate, $R_{obs-PMR}$, didn't exhibit a linear relationship with light intensity. This phenomenon can be explained using the light irradiation model as given in Section 3.1.1, which describes the effective reaction rate constant k being dependent on the light intensity I (mW cm⁻²) as per Eq. (3-1). The effective rate constant, \bar{k} , for a catalyst layer of thickness δ_L is represented by Eq. (3-4).

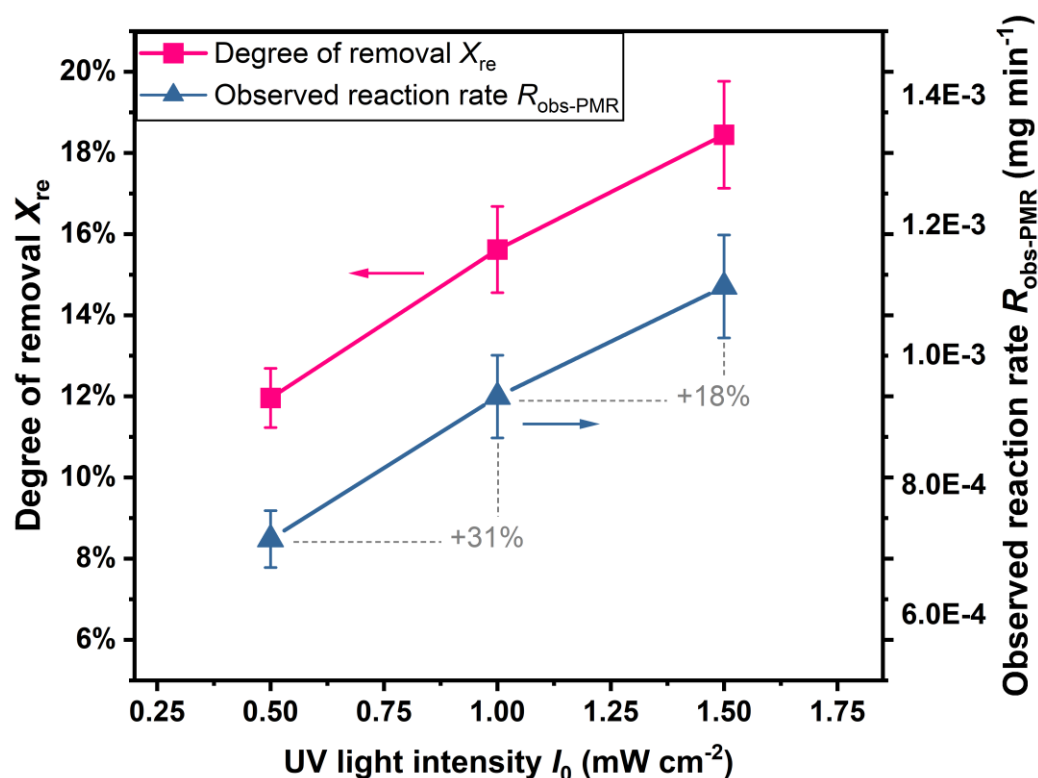


Figure 3-16 Degree of removal and observed reaction rate of RhB degradation by varying the UV light intensity. Experimental conditions: membrane type: Membrane 2; inlet concentration: 15 mg L⁻¹; transmembrane pressure was 0.5 ± 0.1 bar to maintain the permeate flow at 0.13 mL min⁻¹; inlet flow rate: 0.4 mL min⁻¹; Error bars: standard error of the mean. [50]

As discussed earlier, the reaction adheres to Langmuir-Hinshelwood kinetics. Therefore, when the incident light intensity is the sole variable, changes in the observed reaction rate, $R_{obs-PMR}$, are assumed to be solely driven by alterations in the intrinsic reaction rate, which is linearly related to \bar{k} . Specifically, \bar{k} is affected only by the term I_0^b when I_0 is the only variable in this case (see Eq. (3-4)). As I_0 increases from 0.5 to 1 mW cm⁻² and from 1 to 1.5 mW cm⁻², \bar{k} as well as $R_{obs-PMR}$ are calculated to rise by 34.7% and 19% according to Eq. (3-4), respectively. These calculations align very well with the experimental values of 31% and 18% for $R_{obs-PMR}$, respectively.

The experimental observations and theoretical analyses uniformly indicate that enhancing the incident light intensity favorably affects the observed reaction rate. This outcome corroborates the foundational principles of our light irradiation model and underscores the pivotal influence of light intensity on photocatalytic reactions.

3.2.3 Photodegradation of micropollutants

To demonstrate the μ PMR's practicality, its application was extended to the photodegradation

of several micropollutants, including CBZ, SMX and BZF, using selected Mode 1, under UV and visible light. Steady-state conditions were maintained in each experiment, as confirmed by consistent mass flow over time (Figure C 2).

Figure 3-17 illustrates the degree of photocatalytic removal of these pollutants under both light sources, with blank tests indicating negligible photolysis-induced degradation. As depicted in Figure 3-17 (a), under UV light, BZF showed the highest degree of removal, approximately 80%, followed by SMX at about 70%, and CBZ at roughly 50%. Preliminary tests in a batch reactor indicated that under visible light, N-TiO₂ outperformed P25 in decolorization of RhB (data not shown). In the μ PMR, degradation for CBZ, SMX, and BZF under visible light were significantly lower than those under UV light, with CBZ seeing around 10% removal, and SMX and BZF around 30%, all more slowly than under UV light. This variation is attributed to differences in the generation of oxidizing species between N-TiO₂ under visible light and P25 under UV light, influenced by their different band gaps and the reactive species' oxidizing power.

For both lighting conditions, SMX and BZF showed higher degradation rates than CBZ. This could be related to their charge properties, chemical stability, degradation pathways, and adsorption behavior on the catalyst. Filtration tests with catalyst-coated NF membranes showed that SMX and BZF had about 45% rejection, significantly higher than CBZ's 4% (Table 3-7). This difference is due to their molecular weights and charge properties. CBZ is neutral at pH 7.2, while SMX and BZF are negatively charged at pH 7.3 (see Table 2-3). Given that both the membrane and the coating are also negatively charged at the experimental pH, as discussed in Section 3.2.2.2, the negatively charged SMX and BZF are more prone to rejection by the membrane. Ultimately, pollutants that have higher rejection are likely to contribute to an enhanced overall degradation efficiency.

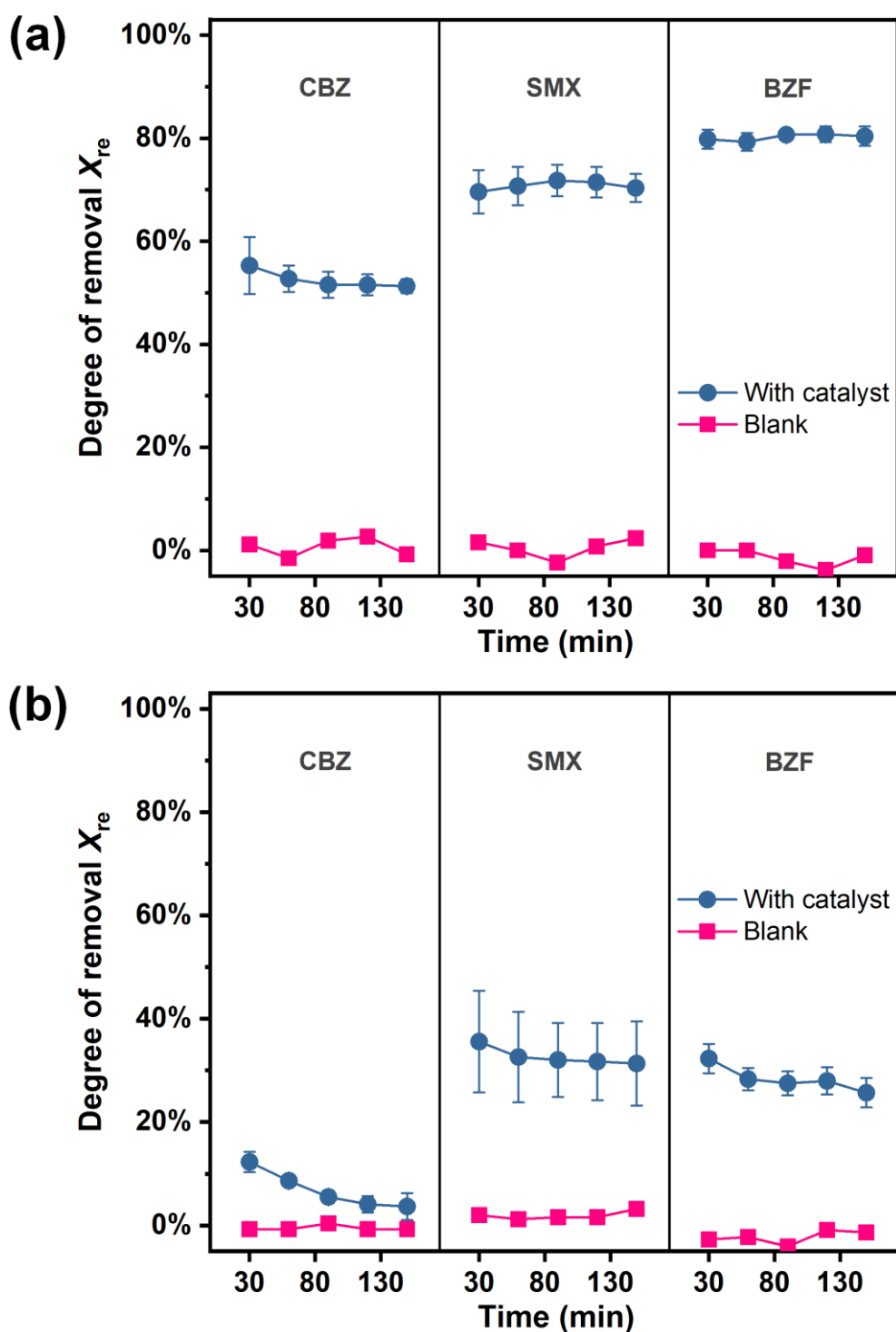


Figure 3-17 Degradation of micropollutants under Mode 1 with (a) UV light and (b) visible light. Experimental conditions: membrane type: Membrane 2; inlet concentration: $20 \mu\text{g L}^{-1}$; inlet flow rate: 0.1 mL min^{-1} ; light intensity: 1.5 mW cm^{-2} for UV light and 0.8 mW cm^{-2} for visible light; split between permeate and retentate volume flow rate was 2:1 under transmembrane pressure of $0.2 \pm 0.1 \text{ bar}$ and $0.3 \pm 0.1 \text{ bar}$ for UV and visible light experiment, respectively; blank tests were conducted under Mode 4 using a metal plate instead of a coated membrane. Error bars: standard error of the mean. [50]

Table 3-7 Rejection of CBZ, SMX and BZF by Membrane 2 under Mode 3 (nanofiltration).

Error: standard error of the mean. [50]

Pollutants	CBZ	SMX	BZF
Rejection α_{mem} (%)	3.9 ± 0.8	43.3 ± 0.4	46.3 ± 0.9

3.2.4 Photodegradation under real sunlight

To further assess the capability of this system in photodegrading pollutants, a proof-of-concept examination was undertaken using real sunlight. The selected pollutants for this investigation were RhB along with two micropollutants, SMX and BZF, with N-TiO₂ serving as the catalyst.

Figure 3-18 illustrates the decolorization of RhB under sunlight, highlighting an initial rapid photocatalytic activity that achieves over 60% removal within the first half-hour. Following this burst, the efficiency plateaus, maintaining a steady state despite a slight reduction in light intensity from over 90 to 80 mW cm⁻².

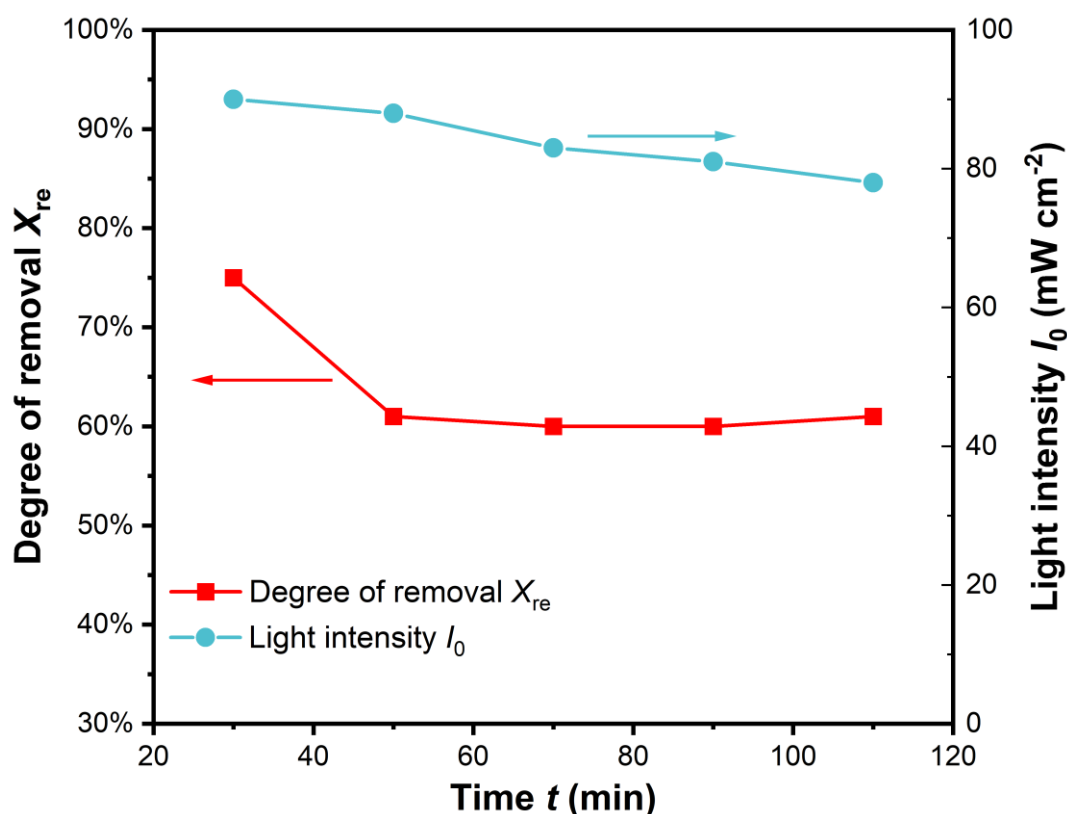


Figure 3-18 Decolorization of RhB under real sunlight. Experimental conditions: flow mode: dead-end flow; inlet flow rate: 0.1 mL min⁻¹; catalyst: N-TiO₂ printed for 10 layers on Membrane 2; inlet concentration: 15 mg L⁻¹.

In contrast, Figure 3-19 captures the degradation process for the micropollutants SMX and BZF under sunlight. The results indicate efficacious photocatalytic activity, with removal efficiencies reaching 61.5% for SMX and 67.3% for BZF. The experiments benefited from consistent sunlight intensity above 95 mW cm^{-2} , thanks to clear weather conditions on the day of testing.

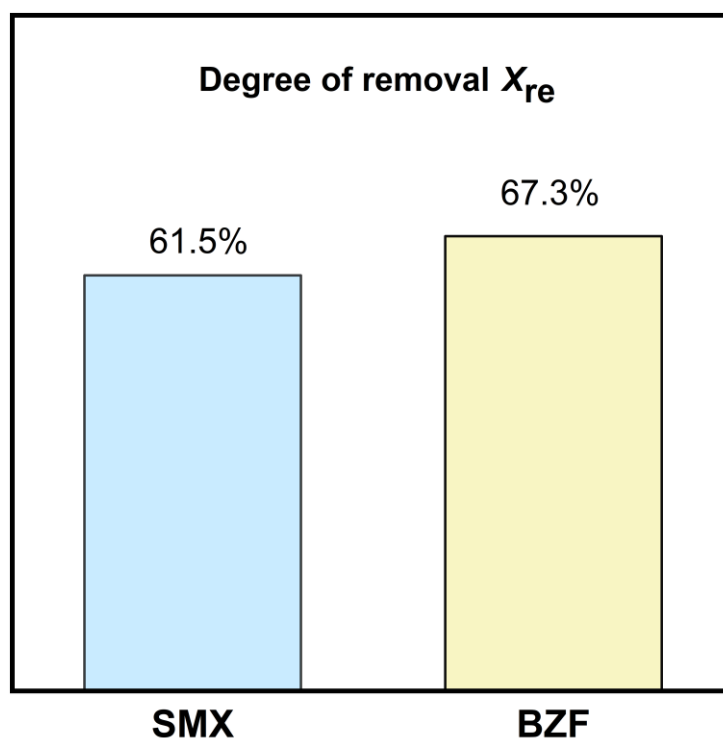


Figure 3-19 Degradation of SMX and BZF under real sunlight. Experimental conditions: flow mode: dead-end flow; inlet flow rate: 0.1 mL min^{-1} ; catalyst: N-TiO₂ printed for 10 layers on Membrane 2; light intensity: $95\text{-}100 \text{ mW cm}^{-2}$; inlet concentration: $50 \mu\text{g L}^{-1}$.

3.2.5 Discussion

Building upon the kinetic study of batch and surface-flow reactors, this section leverages the μ PMR system for a comprehensive analysis of the degradation process, emphasizing process intensification and covering a range of theoretical aspects. Additionally, it explores practical applications, including degradation studies of micropollutants at ultra-low concentrations in the laboratory and under real sunlight conditions.

An initial comparison across four flow modes revealed that the mixed flow-through contactor mode (Mode 1) emerged as the most effective, primarily due to enhanced mass transport under Mode 1. A notable finding was the synergistic effect between nanofiltration and photocatalysis observed in Mode 1, which experimentally enhanced degradation performance. This observed

synergy, potentially induced by increased concentrations of pollutants locally at the membrane surface during filtration, serves to accelerate reaction kinetics. This intriguing effect warrants further investigation to fully understand its implications and optimize degradation processes.

Studies on light intensity further confirmed that an increase in light intensity significantly enhances degradation rates. The trends predicted by the previously developed light model correspond closely with experimental observations, underscoring the model's predictive accuracy.

Degradation experiments with micropollutants demonstrated the system's efficacy, suggesting potential for future systematic studies. The data from these experiments provide a solid foundation for future simulation works.

Moreover, the investigation into real sunlight degradation confirms the system's capability to leverage natural sunlight effectively for the degradation of pollutants, establishing it as a practical tool for photodegradation studies.

4. Selective photooxidation of alcohols

The photocatalytic aerobic oxidation of alcohols is demonstrated in this chapter. Figure 4-1 illustrates this oxidation scheme. The catalyst was applied onto membrane substrates through inkjet-printing. Initial tests in a batch reactor focused on the oxidation of various benzylic and aliphatic alcohols to study optimal experimental conditions. Benzyl alcohol (BA) was selected as the model substrate for in-depth oxidation studies to benzaldehyde (BAI) in the μ PMR, utilizing a continuous-flow setup.

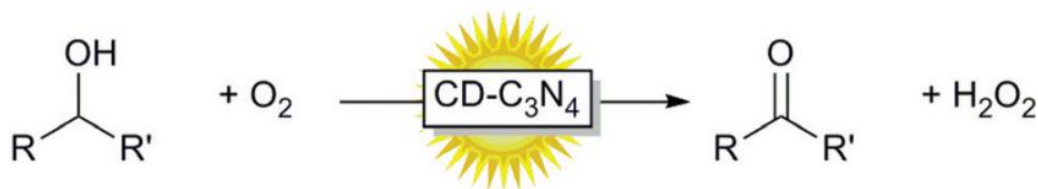


Figure 4-1 Scheme of photocatalytic aerobic oxidation using $\text{CD-C}_3\text{N}_4$

4.1 Experiment in a batch reactor

In the batch experiments, the focused was on two main areas. Initially, various experimental parameters were explored such as the calcination temperature of the printed $\text{CD-C}_3\text{N}_4$, type of catalyst, choice of solvent, introduction of gas into the reactor, number of $\text{CD-C}_3\text{N}_4$ layers printed, and the initial concentration of BA. Subsequently, the photooxidation efficacy across different substrates under the optimized conditions identified from the first part of the study was assessed.

4.1.1 Experimental condition study

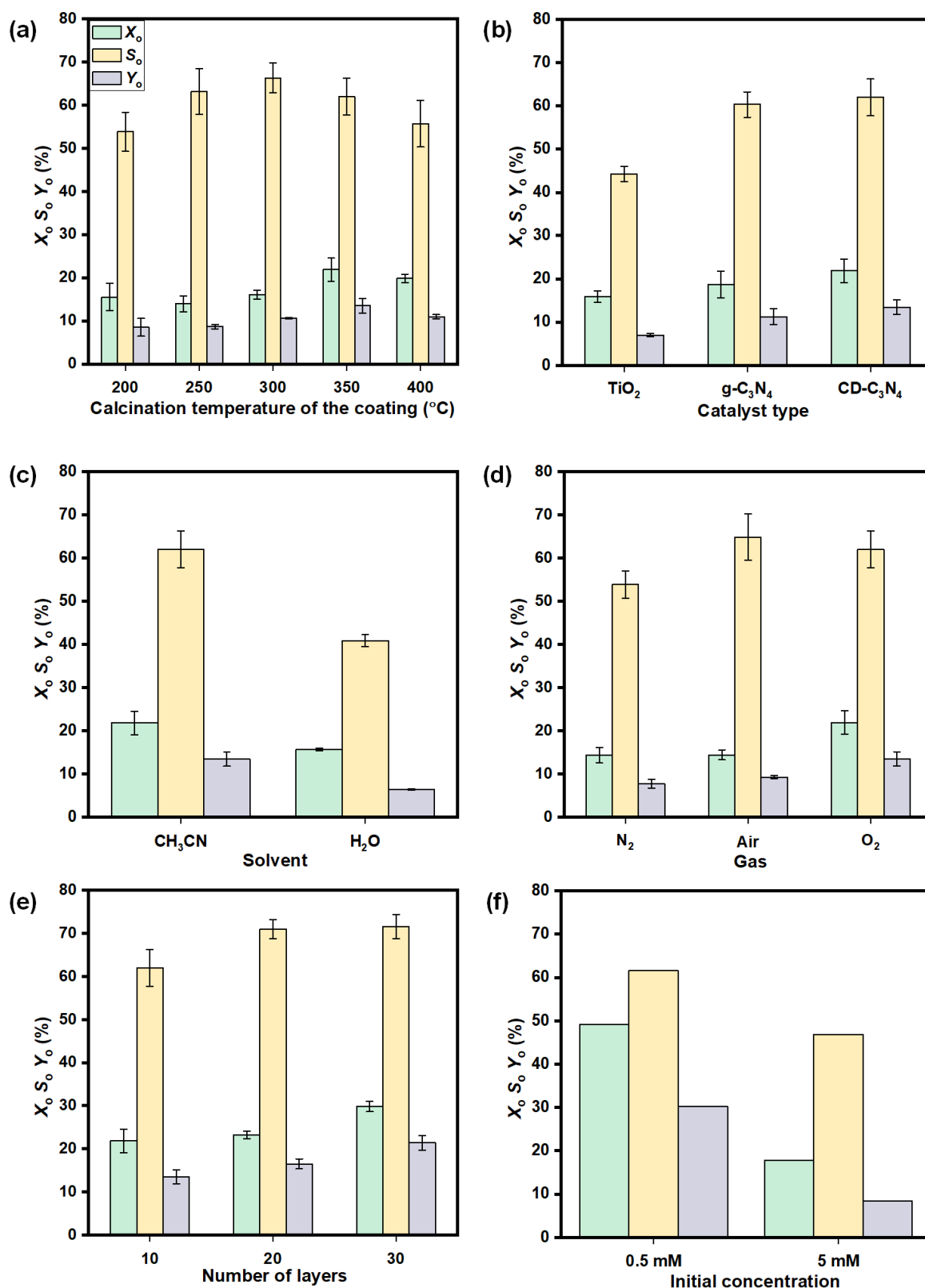


Figure 4-2 Photooxidation of BA in the batch reactor with variations of: (a) calcination temperature of the printed CD-C₃N₄; (b) catalyst type; (c) solvent; (d) gas introduced to the reactor; (e) number of layers of the printed CD-C₃N₄; (f) initial concentration of BA. Reaction conditions: see Table 2-6. Error bars: standard error of the mean.

The experimental conditions were systematically investigated, with key findings illustrated in Figure 4-2. Analysis of single parameters revealed:

- Calcination temperature of the coating

Figure 4-2 (a) illustrates how calcination temperature influences the photooxidation capability of the catalyst over a range from 200 °C to 400 °C, with 350 °C emerging as the optimal one. Lower temperatures may fail to adequately remove organic solvents from the ink, potentially hinder the reaction. On the other hand, calcination influences the catalyst's crystallinity and surface area. Here in this experiment, higher temperatures might induce agglomeration and reduce surface area, thereby adversely impacting photocatalytic efficiency. Consequently, 350 °C was selected for subsequent experiments due to its balance of these factors.

- Catalyst

Figure 4-2 (b) evaluates different catalysts: TiO_2 , $\text{g-C}_3\text{N}_4$, and $\text{CD-C}_3\text{N}_4$, revealing that $\text{CD-C}_3\text{N}_4$ is the highest in conversion, selectivity, and yield. The integration of carbon nanodots in $\text{CD-C}_3\text{N}_4$ likely adds more active sites that improve charge separation and transfer, thus boosting its photocatalytic performance over undoped $\text{g-C}_3\text{N}_4$ and TiO_2 . While $\text{g-C}_3\text{N}_4$ alone shows limited photocatalytic activity due to quick recombination of photoinduced charges, TiO_2 's lower efficacy is attributed to its wider band gap and restricted visible light absorption. In contrast, C_3N_4 -based catalysts, with their narrower band gaps, more efficiently harness the light spectrum. Notably, without a photocatalyst or light source (blank test, data not shown), there was no detectable conversion.

- Solvent

Figure 4-2 (c) demonstrates how solvent affects photocatalytic reactions, comparing acetonitrile (CH_3CN) with water (H_2O). The results show acetonitrile yields better performance than water in all evaluated aspects. The choice of solvent plays a critical role in photocatalysis, affecting reactant solubility, the catalyst's absorption spectrum, and catalyst-solvent interactions. Water, as a solvent in heterogeneous photocatalysis, tends to be adsorbed on the catalyst's surface and undergoes oxidation, producing hydroxyl radicals. This can complicate control over the reaction's selectivity due to water's intense oxidizing conditions and the limited solubility of many organic compounds. In contrast, organic solvents like acetonitrile, which resist oxidation by photogenerated holes, are preferred for ensuring the selectivity of photocatalytic synthesis without participating in the reaction, thus preventing interference with the photocatalytic

process [213].

The beneficial "shield effect" of acetonitrile, reported in literature [214-216], describes its role as a weak base that stabilizes reaction products through solvation, minimizing undesired side reactions by inhibiting proton transfer and radical species formation.

- Gas

Figure 4-2 (d) explores the impact of various gases on photocatalytic efficacy, testing nitrogen (N_2), air, and oxygen (O_2). Oxygen's introduction markedly improves conversion, selectivity, and yield, a result that aligns with its critical role in aerobic oxidation reactions. By capturing electrons, oxygen mitigates electron-hole recombination, thus boosting the efficiency of photocatalytic processes. Air, albeit containing oxygen, exhibits lesser performance compared to pure oxygen, likely due to its diluted oxygen content. Nitrogen, an inert gas, demonstrates minimal effect on photocatalytic outcomes, underscoring the importance of an oxidant in optimizing photocatalytic activity.

- Layer number

Figure 4-2 (e) reveals the impact of varying the number of catalyst layers on the photocatalytic reaction. An upward trend in conversion and yield is observed as the layer count rises from 10 to 30, although selectivity experiences a slight decrease. This improvement in performance with additional layers can likely be linked to the increased presence of active sites, facilitating greater conversion and yield. Yet, the selectivity's reduction could indicate that extra layers may inadvertently foster side reactions or excessive oxidation of the target product due to the augmented layer thickness. Note that very thick layers may also increase the probability to overoxidation due to pore diffusion limitations.

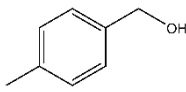
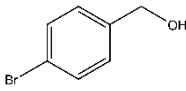
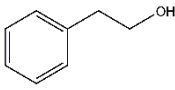
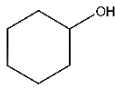
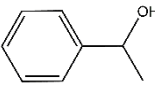
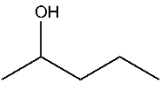
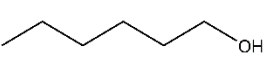
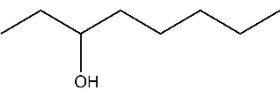
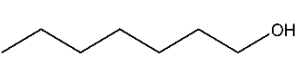
- Initial concentration

Figure 4-2 (f) displays how varying initial concentrations of BA, from 0.5 mM to 5 mM, influences the photocatalytic reaction. The findings indicate enhanced conversion, selectivity, and yield at lower BA concentrations. This enhancement could stem from the active catalyst sites remaining unsaturated at lower reactant levels, facilitating more efficient interactions with BA molecules. Conversely, at higher BA concentrations, these active sites might reach saturation, thereby diminishing overall performance.

4.1.2 Various substrates

The application of CD-C₃N₄ was further expanded using the selected optimum conditions in the batch reactor to include a wider array of substrates, with the outcomes presented in Table 4-1.

Table 4-1 Photocatalytic selective oxidation of various benzylic and aliphatic alcohols with the printed CD-C₃N₄.

Substrate	Structural Formula	X ₀ (%)	S ₀ (%)	Y ₀ (%)
4-Methylbenzyl alcohol		61	67	41
4-Bromobenzyl alcohol		68	52	35
Phenethyl alcohol		25	17	4
Cyclohexanol		31	33	10
1-Phenylethanol		38	38	14
2-Pentanol		29	28	8
1-Hexanol		24	38	9
3-Octanol		21	13	3
1-Heptanol		26	29	8

Reaction conditions: temperature 23 °C, light intensity 100 mW cm⁻², solvent CH₃CN, calcination temperature for the sample 350 °C, number of printed layers 30, initial concentration 1.5 mM, O₂ 5 ml min⁻¹ at 1 atm, reaction time 12 h.

Particularly striking is the performance exhibited by 4-Methylbenzyl alcohol, which achieved a conversion rate of 61%, coupled with a high selectivity of 67% and a notable yield of 41%. This result demonstrates the robust catalytic efficiency of CD-C₃N₄ when applied to substrates that possess an electron-donating group, such as a methyl moiety, in the para position relative to the hydroxyl function. The electron-donating characteristics may facilitate the photocatalytic process, enhancing the reactivity of the hydroxyl group and thereby improving overall conversion rates.

On the other hand, cyclohexanol presents a contrasting scenario. With a modest conversion rate of 31%, a selectivity of 33%, and a yield limited to 10%, it becomes evident that the cyclic structure of this alcohol poses a significant hindrance to the photocatalytic oxidation process. The lack of extended conjugation, as found in benzyl alcohols, could be a factor in the reduced efficiency seen with cyclohexanol, highlighting the importance of molecular structure in influencing the photocatalytic activity.

The results for phenethyl alcohol and various longer-chain aliphatic alcohols (e.g., 1-hexanol and 1-heptanol) reveal a consistent trend of decreasing catalytic performance with increasing alkyl chain length. Phenethyl alcohol, with a conversion and selectivity both at 38% and yield at 14%, indicates a moderate catalytic activity. This activity decreases progressively as the aliphatic chain elongates, with 1-hexanol and 1-heptanol showing reduced conversion rates of 24% and 26%, selectivity rates of 38% and 29%, and yields of 9% and 8%, respectively. Such results imply that as the substrate's molecular size increases, the accessibility or interaction with the catalytic sites may be impeded, leading to lower photocatalytic effectiveness.

4.2 Photooxidation of benzyl alcohol in the μ PMR

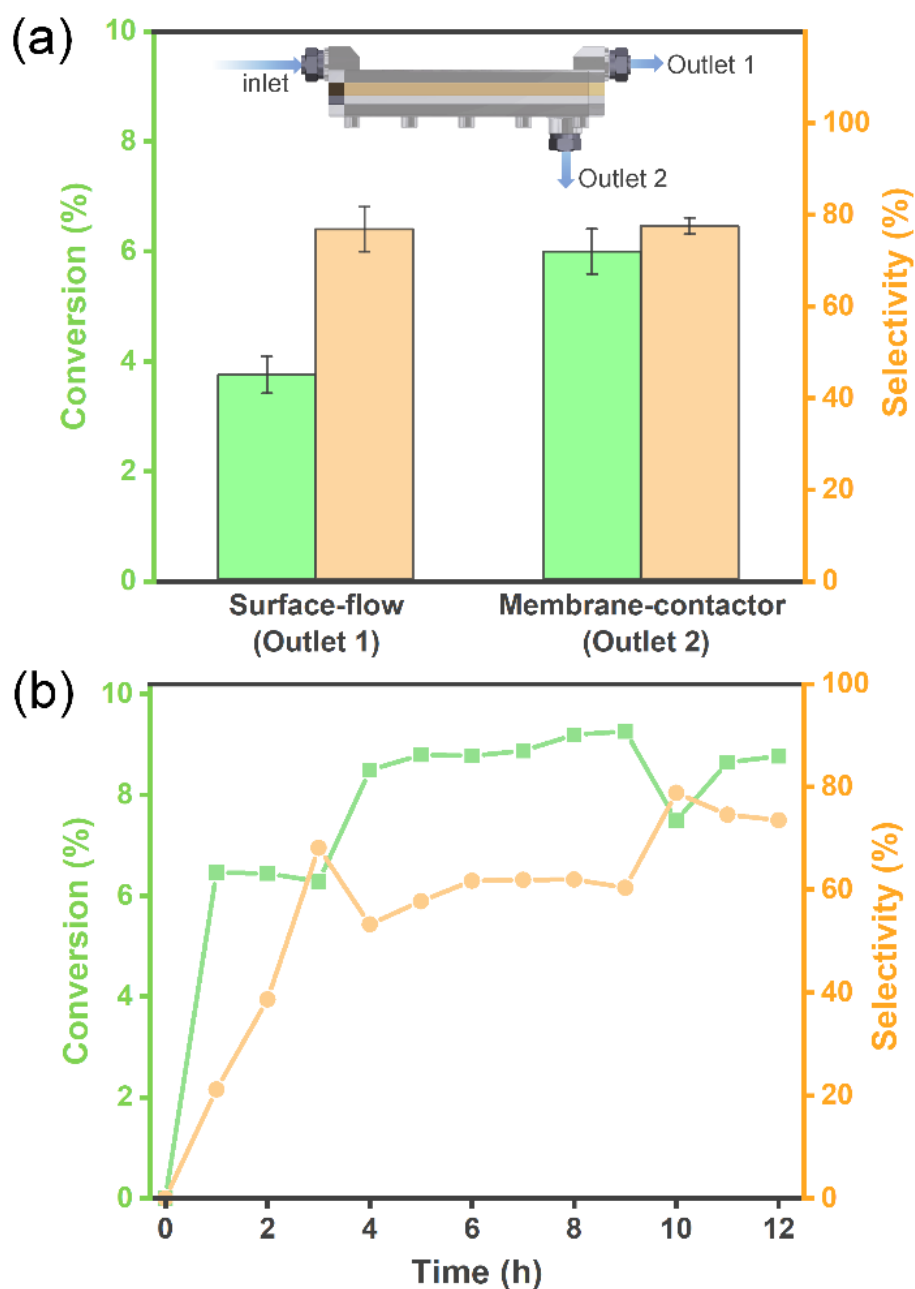


Figure 4-3 Results of photooxidation of BA in μ PMR: (a) comparison of two flow modes on the photooxidation of BA by recirculating the flow in the system; (b) 12-hour test of membrane contactor flow mode under dead-end flow without recirculation. Reaction conditions: see Section 2.3.2.3.

Photooxidation of BA in the μ PMR was also conducted. The results are shown in Figure 4-3. Figure 4-3 (a) illustrates a comparison between the performance of membrane-contactor mode (Mode 1) and surface-flow mode (Mode 4). The results underpin that the membrane-contactor mode achieves higher conversion than the surface-flow mode, while maintaining similar levels

of selectivity for both modes. This improvement in the membrane-contactor mode is attributed to enhanced mass transport. By allowing the reactant to flow through the catalyst layer, it increases the mass transfer coefficient, thereby facilitating higher conversion rates. This finding is also given in Chapter 3. The consistent selectivity across both modes suggests that they share comparable selectivity towards the desired reaction pathway, despite the variance in mass transport efficiency.

Figure 4-3 (b) presents results from a 12-hour experiment utilizing the membrane-contactor mode for the photooxidation of BA, conducted without recirculation of the reactant. Given the single-run flow's shorter residence time, the conversion stabilized at approximately 8%. However, the selectivity observed was comparable to the results from Figure 4-3 (a),

4.3 Discussion

This chapter shifts focus from the detailed exploration of photodegradation processes discussed earlier, introducing preliminary proof-of-concept experiments that highlight the system's versatility across a broader spectrum of photocatalytic reactions. These initial findings underscore the system's adaptability to defined operational parameters, providing a foundation for more targeted and systematic future studies.

The results from these preliminary experiments reveal that factors such as the solvent used, the type of photocatalyst, the presence of oxygen significantly influence the selectivity and conversion of the reactions. The μ PMR shows its advantage in mass transport when operating in contactor mode, as it was the case also for the photodegradation study.

The focus on the selective oxidation of benzyl alcohols contrasts with the potentially more industrially relevant, yet more complex, oxidation of aliphatic or secondary alcohols. Despite numerous studies into photocatalytic oxidation of alcohols under visible light, achieving high conversion and selectivity remains a considerable challenge, particularly for aliphatic alcohols. The quest for photocatalysts that efficiently harness solar energy while managing charge carriers and oxidative species with precision underscores the ongoing need for innovation in this field.

Moreover, transitioning these processes from batch to continuous-flow operations to enhance yields presents its own set of challenges, necessitating further in-depth exploration to unlock the potential of photocatalytic reactions for industrial applications.

5. Summary and conclusions

This dissertation presents the development and application of a microstructured photocatalytic membrane reactor (μ PMR) for addressing two significant environmental challenges: the photodegradation of pollutants in water and the selective photooxidation of alcohols. The μ PMR design integrates advanced photocatalysis with membrane technology, offering a novel approach to enhance reaction efficiencies under well-defined operational conditions.

The μ PMR was designed with a dual microchannel configuration and an innovative optical system, ensuring uniform light distribution and optimal reactor illumination. This design facilitated the deployment of two types of photocatalysts: TiO_2 for pollutant degradation and carbon-nanodot-doped C_3N_4 (CD- C_3N_4) for alcohol photooxidation. The reactor's capability to operate in continuous flow under well-defined conditions, such as light type, intensity, and flow mode, marks a significant advancement in photocatalytic reactors.

Focusing on the photodegradation application, the μ PMR demonstrated remarkable efficiency in degrading model dye pollutants, including Rhodamine B (RhB), and three pharmaceutical micropollutants: Carbamazepine (CBZ), Sulfamethoxazole (SMX), and Bezafibrate (BZF). A detailed kinetic study, adopting the Langmuir–Hinshelwood model, accounted for intrinsic reaction kinetics and mass transport limitations, underscoring the reactor's effectiveness in pollutant degradation. This study not only confirmed the μ PMR's potential for environmental remediation but also highlighted the synergistic effects of integrating membrane filtration with photocatalysis.

The organic synthesis section presents initial proof-of-concept experiments in both batch and μ PMR setups, demonstrating the catalytic activity of C_3N_4 for the selective photooxidation of alcohols to their corresponding aldehydes. These experiments focused on optimizing operational parameters within a batch reactor and exploring the performance across various alcohol substrates. Moreover, the μ PMR demonstrated its capability to enhance mass transport

significantly when operating in contactor mode.

The development of the μ PMR and its application to both environmental remediation and organic synthesis represents a substantial contribution to the field of photocatalysis. This work successfully addresses the limitations of traditional photocatalytic systems by providing a versatile platform that combines high efficiency and operational control. Furthermore, the reactor's design and operational flexibility underscore its potential for scale-up and application in various photocatalytic processes.

This dissertation underscores the significant potential of microstructured photocatalytic membrane reactors in environmental and synthetic chemistry applications. The μ PMR's innovative design, combined with the strategic use of photocatalysts, paves the way for advanced photocatalytic processes that are efficient, selective, and adaptable to a wide range of applications. This research not only contributes to the fundamental understanding of photocatalytic processes but also offers practical solutions for pollutant degradation and the synthesis of valuable chemical products.

6. Outlook

The development of PMRs represents a significant advancement in the fields of environmental and synthetic chemistry, offering innovative approaches for water treatment and organic synthesis. However, the transition from laboratory-scale prototypes to industrial-scale applications presents a variety of challenges. This summary highlights both future research directions necessary for the advancement of PMRs and the critical challenges associated with scaling these systems for practical use.

Future research in PMRs should focus on deepening the understanding of photocatalytic reactions through simulation studies. This is essential for refining theoretical models and optimizing PMRs for better performance. Additionally, it is important to test PMRs in real water matrices to evaluate their effectiveness against complex environmental pollutants, thereby pushing the boundaries of this technology beyond controlled laboratory conditions. Furthermore, the identification of degradation products is necessary to ensure that the treatment process yields less harmful or non-toxic byproducts. The search for new photocatalysts is also crucial, with an emphasis on materials that are active under visible light, exhibit high stability, activity, and selectivity, and can utilize full sunlight efficiently. Expanding the range of model reactions investigated with PMRs will demonstrate their versatility across different chemical processes and broaden their potential applications.

Scaling up PMRs to an industrial level involves overcoming several complex challenges. Ensuring uniform light distribution in larger reactors is crucial but challenging, necessitating innovative reactor designs for optimal light penetration. Heat management becomes increasingly important in large-scale operations to avoid negatively impacting the catalysts and reaction dynamics; thus, effective heat dissipation methods are needed to prevent hotspots. Additionally, achieving effective mass transfer is more challenging as the reactor size increases, requiring careful design and optimization of flow patterns to enhance reaction efficiency.

For PMRs to find industrial applications, several practical aspects must be addressed. Developing materials that can withstand harsh operational conditions is critical for the durability of catalysts and membranes within PMRs. The economic feasibility of PMRs also hinges on identifying cost-effective materials and optimizing system design. Moreover, harmonizing photocatalytic and membrane processes through advanced control strategies will be crucial for enhancing the efficiency of PMRs.

Moreover, the integration of micro process technology with photocatalytic reactors presents an exciting avenue for decentralized applications. Microreactor platforms enable precise control over operation parameters, which can significantly enhance photocatalytic efficiency even at small scales. Such systems are ideally suited for on-site wastewater treatment units in remote or distributed locations, where conventional large-scale plants are impractical. Furthermore, continuous-flow microreactors can be engineered for the selective photooxidation or reduction of fine chemicals and active pharmaceutical ingredients (APIs), offering streamlined, scalable synthesis with improved safety, reduced footprint, and lower energy consumption.

In conclusion, while PMRs offer great promise for sustainable applications, realizing their full potential demands overcoming significant technical and practical challenges. Addressing these challenges through continued research and innovation will pave the way for the successful industrial implementation of PMRs, contributing to environmental sustainability and the advancement of green chemistry.

Abbreviations and symbols

Abbreviations

AFM	atomic force microscopy
ALD	atomic layer deposition
API	active pharmaceutical ingredient
ATR-FTIR	attenuated total reflectance - Fourier transform infrared spectroscopy
BA	benzyl alcohol
BAI	benzaldehyde
BET	brunauer–emmett–teller
BF	bright-field
BJH	barrett-joyner-halenda
BPR	back pressure regulator
BZF	bezafibrate
CBZ	carbamazepine
CCD	charge coupled device
CD-C ₃ N ₄	carbon-nanodot-doped C ₃ N ₄
COF	covalent organic framework
CVD	chemical vapor deposition
DLS	dynamic light scattering
DRS	diffuse reflectance spectroscopy
E2	β-oestradiol
EDC	endocrine disrupting compound
ESI	electro spray ionization
FID	flame ionization detector
FPR	fixed-bed photocatalytic reactors

GC	gas chromatography
g-C ₃ N ₄	graphitic carbon nitride
HPLC	high performance liquid chromatography
IMVT	institute for micro process engineering
LED	light emitting diode
LH	Langmuir-Hinshelwood
MB	methylene blue
MFC	mass flow controller
MOF	metal-organic framework
MS	mass spectrometric
MWCO	molecular weight cut-off
N-TiO ₂	nitrogen-doped TiO ₂
NF	nanofiltration
PANI	polyaniline
PES	polyether sulfone
PEEK	polyetheretherketone
PMR	photocatalytic membrane reactor
PTFE	polytetrafluoroethylene
PVDF	polyvinylidene fluoride
PVC	polyvinyl chloride
RB	rose bengal
RhB	rhodamine B
RIR	reference intensity ratio
RO	reverse osmosis
ROS	reactive oxygen species
SAED	selected area electron diffraction
SEM	scanning electron microscopy

SMX	sulfamethoxazole
TEM	transmission electron microscopy
TGA	thermogravimetric analysis
UV	ultraviolet
Vis	visible
XPS	x-ray photoelectron spectroscopy
XRD	x-ray diffraction
μ PMR	microstructured photocatalytic membrane reactor

Symbols

A	m^2	area
C	g m^{-3}	concentration
D	$\text{m}^2 \text{s}^{-1}$	diffusivity
d	m	diameter
E_g	eV	bandgap energy
H	m	height
I	mW cm^{-2}	light intensity
i	μm	distance between two droplets in x- or y-direction
K	$\text{m}^3 \text{g}^{-1}$	equilibrium constant
k	$\text{g g}^{-1} \text{s}^{-1}$	reaction rate constant
\bar{k}	$\text{g g}^{-1} \text{s}^{-1}$	effective rate constant
L	m	length
l	m	length
g	g	mass
N	-	total number
P	m	perimeter
R	g s^{-1}	reaction rate

S	%	selectivity
T	-	transmission
t	s	time
\bar{u}	m s^{-1}	mean flow velocity
V	m^3	volume
\dot{V}	$\text{m}^3 \text{s}^{-1}$	volumetric flow rate
X	%	conversion of reaction or degree of degradation
Y	%	yield

α_{noz}	μm	nozzle diameter
α_{mem}	%	membrane rejection
a	-	absorption coefficient
β_{m}	m s^{-1}	mass transfer coefficient
ω	m^{-1}	extinction coefficient
τ	-	tortuosity
ε	-	porosity
δ	m	thickness
η	$\text{kg m}^{-1} \text{s}^{-1}$	dynamic viscosity
h	J s^{-1}	Planck's constant
ν	Hz or $\text{m}^2 \text{s}^{-1}$	light frequency or kinematic viscosity
ρ	g m^{-3}	density
γ	kg s^{-2}	surface tension
Ψ_{WP}	-	Weisz modulus

Z	-	non-dimensional number for assessing printability
Oh	-	Ohnesorge number
We	-	Weber Number

<i>Re</i>	-	Reynolds number
<i>Sh</i>	-	Sherwood number
<i>Sc</i>	-	Schmidt number

Subscripts and superscripts

eff	effective
ad	adsorption
x	x direction
y	y direction
cat	catalyst
L	printed layer
ink	ink
b	bulk
re	removal
obs	observed
ini	initial
eva	evaporation
act	actual
meas	measured
o	oxidation
Al	alcohol
AlD	aldehyde
batch	batch reactor
int	intrinsic
i	time point i
sim	simulation
exp	experiment

WP	Weisz-Prater
ext.	external
n	reaction order
s	surface
h	hydraulic
C	channel

References

- [1] D. Cambie, C. Bottecchia, N.J. Straathof, V. Hessel, T. Noel, Applications of continuous-flow photochemistry in organic synthesis, material science, and water treatment, *Chem Rev*, 116 (2016) 10276-10341.
- [2] A. Fujishima, K. Honda, Electrochemical photolysis of water at a semiconductor electrode, *Nature*, 238 (1972) 37-38.
- [3] H. Kisch, Semiconductor photocatalysis-mechanistic and synthetic aspects, *Angew Chem Int Ed Engl*, 52 (2013) 812-847.
- [4] K. Nakata, A. Fujishima, TiO₂ photocatalysis: design and applications, *Journal of Photochemistry and Photobiology C: Photochemistry Reviews*, 13 (2012) 169-189.
- [5] M.S. Mauter, I. Zucker, F.o. Perreault, J.R. Werber, J.-H. Kim, M. Elimelech, The role of nanotechnology in tackling global water challenges, *Nature Sustainability*, 1 (2018) 166-175.
- [6] X. Zhang, S. Xiong, A. Sathiyaseelan, L. Zhang, Y. Lu, Y. Chen, T. Jin, M.-H. Wang, Recent advances in photocatalytic nanomaterials for environmental remediation: Strategies, mechanisms, and future directions, *Chemosphere*, 364 (2024) 143142.
- [7] A.S. Mestre, A.P. Carvalho, Photocatalytic degradation of pharmaceuticals carbamazepine, diclofenac, and sulfamethoxazole by semiconductor and carbon materials: a review, *Molecules*, 24 (2019).
- [8] D.A. Lambropoulou, M.D. Hernando, I.K. Konstantinou, E.M. Thurman, I. Ferrer, T.A. Albanis, A.R. Fernandez-Alba, Identification of photocatalytic degradation products of bezafibrate in TiO₂ aqueous suspensions by liquid and gas chromatography, *J Chromatogr A*, 1183 (2008) 38-48.
- [9] M. Gmurek, M. Olak-Kucharczyk, S. Ledakowicz, Photochemical decomposition of endocrine disrupting compounds – a review, *Chemical Engineering Journal*, 310 (2017) 437-456.
- [10] R. Lyubimenko, O.I. Gutierrez Cardenas, A. Turshatov, B.S. Richards, A.I. Schäfer, Photodegradation of steroid-hormone micropollutants in a flow-through membrane reactor coated with Pd(II)-porphyrin, *Applied Catalysis B: Environmental*, 291 (2021) 120097.
- [11] S. Lotfi, K. Fischer, A. Schulze, A.I. Schäfer, Photocatalytic degradation of steroid hormone micropollutants by TiO₂-coated polyethersulfone membranes in a continuous flow-through process, *Nature Nanotechnology*, 17 (2022) 417-423.
- [12] R. Lyubimenko, A. Turshatov, A. Welle, P.G. Weidler, B.S. Richards, A.I. Schäfer, Enhanced photocatalytic efficiency via improved contact in a solar-driven membrane reactor for steroid hormone removal, *Chemical Engineering Journal*, 451 (2023) 138449.
- [13] M.H. Dehghani, S. Ahmadi, S. Ghosh, M.S. Khan, A. Othmani, W.A. Khanday, Ö. Gökkuş, C. Osagie, M. Ahmaruzzaman, S.R. Mishra, E.C. Lima, N.M. Mubarak, R.R. Karri, K. Ansari,

Sustainable remediation technologies for removal of pesticides as organic micro-pollutants from water environments: a review, *Applied Surface Science Advances*, 19 (2024) 100558.

[14] M. Clara, N. Kreuzinger, B. Strenn, O. Gans, H. Kroiss, The solids retention time-a suitable design parameter to evaluate the capacity of wastewater treatment plants to remove micropollutants, *Water Res*, 39 (2005) 97-106.

[15] S. Esplugas, D.M. Bila, L.G. Krause, M. Dezotti, Ozonation and advanced oxidation technologies to remove endocrine disrupting chemicals (EDCs) and pharmaceuticals and personal care products (PPCPs) in water effluents, *J Hazard Mater*, 149 (2007) 631-642.

[16] B.I. Escher, H.M. Stapleton, E.L. Schymanski, Tracking complex mixtures of chemicals in our changing environment, *Science*, 367 (2020) 388-392.

[17] A.C. Johnson, X. Jin, N. Nakada, J.P. Sumpter, Learning from the past and considering the future of chemicals in the environment, *Science*, 367 (2020) 384-387.

[18] E. Diamanti-Kandarakis, J.-P. Bourguignon, L.C. Giudice, R. Hauser, G.S. Prins, A.M. Soto, R.T. Zoeller, A.C. Gore, Endocrine-disrupting chemicals: an endocrine society scientific statement, *Endocrine Reviews*, 30 (2009) 293-342.

[19] M.N. Chong, B. Jin, C.W.K. Chow, C. Saint, Recent developments in photocatalytic water treatment technology: a review, *Water Research*, 44 (2010) 2997-3027.

[20] A.J.C. Semião, A.I. Schäfer, Removal of adsorbing estrogenic micropollutants by nanofiltration membranes. Part A - Experimental evidence, *Journal of Membrane Science*, 431 (2013) 244-256.

[21] L.D. Nghiem, A. Manis, K. Soldenhoff, A.I. Schäfer, Estrogenic hormone removal from wastewater using NF/RO membranes, *Journal of Membrane Science*, 242 (2004) 37-45.

[22] A. Imbrogno, A.I. Schäfer, Comparative study of nanofiltration membrane characterization devices of different dimension and configuration (cross flow and dead end), *Journal of Membrane Science*, 585 (2019) 67-80.

[23] S. Sanches, C. Nunes, P.C. Passarinho, F.C. Ferreira, V.J. Pereira, J.G. Crespo, Development of photocatalytic titanium dioxide membranes for degradation of recalcitrant compounds, *Journal of Chemical Technology & Biotechnology*, 92 (2017) 1727-1737.

[24] H. Liu, H. Zhang, X. Dong, C. Wu, E. Lichtfouse, Removal of antibiotics from black water by a membrane filtration-visible light photocatalytic system, *Journal of Water Process Engineering*, 53 (2023) 103605.

[25] H.C. Aran, D. Salamon, T. Rijnaarts, G. Mul, M. Wessling, R.G.H. Lammertink, Porous photocatalytic membrane microreactor (P2M2): a new reactor concept for photochemistry, *Journal of Photochemistry and Photobiology A: Chemistry*, 225 (2011) 36-41.

[26] S. Leong, A. Razmjou, K. Wang, K. Hapgood, X. Zhang, H. Wang, TiO₂ based photocatalytic membranes: a review, *Journal of Membrane Science*, 472 (2014) 167-184.

[27] C. Chen, L. Lu, L. Fei, J. Xu, B. Wang, B. Li, L. Shen, H. Lin, Membrane-catalysis integrated system for contaminants degradation and membrane fouling mitigation: a review, *Science of The Total Environment*, 904 (2023) 166220.

- [28] S.A. Heredia Deba, B.A. Wols, D.R. Yntema, R.G.H. Lammertink, Transport and surface reaction model of a photocatalytic membrane during the radical filtration of methylene blue, *Chemical Engineering Science*, 254 (2022) 117617.
- [29] S.A. Heredia Deba, B.A. Wols, D.R. Yntema, R.G.H. Lammertink, Photocatalytic ceramic membrane: effect of the illumination intensity and distribution, *Journal of Photochemistry and Photobiology A: Chemistry*, 437 (2023) 114469.
- [30] S.A. Heredia Deba, B.A. Wols, D.R. Yntema, R.G.H. Lammertink, Advanced ceramics in radical filtration: TiO₂ layer thickness effect on the photocatalytic membrane performance, *Journal of Membrane Science*, 672 (2023) 121423.
- [31] M. Raffaele, A. Pietro, L. Cristina, Review on reduction and partial oxidation of organics in photocatalytic (membrane) reactors, *Current Organic Chemistry*, 17 (2013) 2516-2537.
- [32] G. Palmisano, V. Augugliaro, M. Pagliaro, L. Palmisano, Photocatalysis: a promising route for 21st century organic chemistry, *Chem Commun (Camb)*, (2007) 3425-3437.
- [33] C.-J. Li, G.-R. Xu, B. Zhang, J.R. Gong, High selectivity in visible-light-driven partial photocatalytic oxidation of benzyl alcohol into benzaldehyde over single-crystalline rutile TiO₂ nanorods, *Applied Catalysis B: Environmental*, 115-116 (2012) 201-208.
- [34] P. Ciambelli, D. Sannino, V. Palma, V. Vaiano, Photocatalysed selective oxidation of cyclohexane to benzene on MoO_x/TiO₂, *Catalysis Today*, 99 (2005) 143-149.
- [35] S. Lacombe, T. Pigot, Materials for selective photo-oxygenation vs. photocatalysis: preparation, properties and applications in environmental and health fields, *Catalysis Science & Technology*, (2016) 1571-1592.
- [36] A. Maldotti, L. Andreotti, A. Molinari, S. Tollari, A. Penoni, S. Cenini, Photochemical and photocatalytic reduction of nitrobenzene in the presence of cyclohexene, *Journal of Photochemistry and Photobiology A: Chemistry*, 133 (2000) 129-133.
- [37] K. Imamura, T. Yoshikawa, K. Hashimoto, H. Kominami, Stoichiometric production of aminobenzenes and ketones by photocatalytic reduction of nitrobenzenes in secondary alcoholic suspension of titanium(IV) oxide under metal-free conditions, *Applied Catalysis B: Environmental*, 134-135 (2013) 193-197.
- [38] Z. Shen, Y. Hu, B. Li, Y. Zou, S. Li, G. Wilma Busser, X. Wang, G. Zhao, M. Muhler, State-of-the-art progress in the selective photo-oxidation of alcohols, *Journal of Energy Chemistry*, 62 (2021) 338-350.
- [39] S. Najafshirtari, K. Friedel Ortega, M. Douthwaite, S. Pattison, G.J. Hutchings, C.J. Bondue, K. Tschulik, D. Waffel, B. Peng, M. Deitermann, G.W. Busser, M. Muhler, M. Behrens, A perspective on heterogeneous catalysts for the selective oxidation of alcohols, *Chemistry – A European Journal*, 27 (2021) 16809-16833.
- [40] Y. Su, N.J. Straathof, V. Hessel, T. Noel, Photochemical transformations accelerated in continuous-flow reactors: basic concepts and applications, *Chemistry*, 20 (2014) 10562-10589.
- [41] G. Odling, N. Robertson, Bridging the gap between laboratory and application in photocatalytic water purification, *Catalysis Science & Technology*, 9 (2019) 533-545.

- [42] S. Chang, X. Yang, Y. Sang, H. Liu, Highly efficient photocatalysts and continuous-flow photocatalytic reactors for degradation of organic pollutants in wastewater, *Chem Asian J*, 11 (2016) 2352-2371.
- [43] J. Hogan, A little goes a long way, *Nature*, 442 (2006) 2.
- [44] S.E. M., W. Peter, Photochemical flow reactions, *Israel Journal of Chemistry*, 54 (2014) 361-370.
- [45] E.E. Coyle, M. Oelgemöller, Micro-photochemistry: photochemistry in microstructured reactors. The new photochemistry of the future?, *Photochem Photobiol Sci*, 7 (2008) 1313-1322.
- [46] H.P. Gemoets, Y. Su, M. Shang, V. Hessel, R. Luque, T. Noel, Liquid phase oxidation chemistry in continuous-flow microreactors, *Chem Soc Rev*, 45 (2016) 83-117.
- [47] X. Zheng, Z.-P. Shen, L. Shi, R. Cheng, D.-H. Yuan, Photocatalytic Membrane Reactors (PMRs) in Water Treatment: Configurations and Influencing Factors, *Catalysts*, 7 (2017) 224.
- [48] S. Mozia, On photocatalytic membrane reactors in water and wastewater treatment and organic synthesis, *Copernican Letters*, 6 (2015).
- [49] O. Iglesias, M.J. Rivero, A.M. Urtiaga, I. Ortiz, Membrane-based photocatalytic systems for process intensification, *Chemical Engineering Journal*, 305 (2016) 136-148.
- [50] X. Zhan, Y. Wang, M. Rubin, Y. Bao, F. Kirschhöfer, G. Brenner-Weiß, A.I. Schäfer, R. Dittmeyer, A novel microstructured photocatalytic membrane reactor for enhanced photodegradation of pollutants - from process understanding to practical application, *Separation and Purification Technology*, (Submitted).
- [51] K. Loubière, M. Oelgemöller, T. Aillet, O. Dechy-Cabaret, L. Prat, Continuous-flow photochemistry: a need for chemical engineering, *Chemical Engineering and Processing: Process Intensification*, 104 (2016) 120-132.
- [52] M. Oelgemöller, Solar photochemical synthesis: from the beginnings of organic photochemistry to the solar manufacturing of commodity chemicals, *Chemical Reviews*, 116 (2016) 9664-9682.
- [53] C. Sambigioglio, T. Noël, Flow photochemistry: shine some light on those tubes!, *Trends in Chemistry*, (2019).
- [54] C. Raviola, L. Capaldo, D. Ravelli, A tan for molecules: photocatalyzed synthesis with direct sunlight, *Rendiconti Lincei. Scienze Fisiche e Naturali*, 30 (2019) 485-495.
- [55] Y. Qu, X. Duan, Progress, challenge and perspective of heterogeneous photocatalysts, *Chem Soc Rev*, 42 (2013) 2568-2580.
- [56] S. Malato, P. Fernández-Ibáñez, M.I. Maldonado, J. Blanco, W. Gernjak, Decontamination and disinfection of water by solar photocatalysis: recent overview and trends, *Catalysis Today*, 147 (2009) 1-59.
- [57] A.L. Linsebigler, G. Lu, J.T. Yates, Photocatalysis on TiO₂ surfaces: principles, mechanisms, and selected results, *Chemical Reviews*, 95 (1995) 735-758.

- [58] D. Tang, G. Lu, Z. Shen, Y. Hu, L. Yao, B. Li, G. Zhao, B. Peng, X. Huang, A review on photo-, electro- and photoelectro- catalytic strategies for selective oxidation of alcohols, *Journal of Energy Chemistry*, 77 (2023) 80-118.
- [59] P.V. Laxma Reddy, B. Kavitha, P.A. Kumar Reddy, K.-H. Kim, TiO₂-based photocatalytic disinfection of microbes in aqueous media: a review, *Environmental Research*, 154 (2017) 296-303.
- [60] X. Li, J. Wang, Y. Men, Z. Bian, TiO₂ mesocrystal with exposed (001) facets and CdS quantum dots as an active visible photocatalyst for selective oxidation reactions, *Applied Catalysis B: Environmental*, 187 (2016) 115-121.
- [61] J.-M. Herrmann, Heterogeneous photocatalysis: fundamentals and applications to the removal of various types of aqueous pollutants, *Catalysis Today*, 53 (1999) 115-129.
- [62] A. Visan, J.R. van Ommen, M.T. Kreutzer, R.G.H. Lammertink, Photocatalytic reactor design: guidelines for kinetic investigation, *Industrial & Engineering Chemistry Research*, 58 (2019) 5349-5357.
- [63] A. Visan, D. Rafieian, W. Ogieglo, R.G.H. Lammertink, Modeling intrinsic kinetics in immobilized photocatalytic microreactors, *Applied Catalysis B: Environmental*, 150-151 (2014) 93-100.
- [64] X. Zhan, C. Yan, Y. Zhang, G. Rinke, G. Rabsch, M. Klumpp, A.I. Schäfer, R. Dittmeyer, Investigation of the reaction kinetics of photocatalytic pollutant degradation under defined conditions with inkjet-printed TiO₂ films – from batch to a novel continuous-flow microreactor, *Reaction Chemistry & Engineering*, 5 (2020) 1658–1670.
- [65] J.P.S. Valente, P.M. Padilha, A.O. Florentino, Studies on the adsorption and kinetics of photodegradation of a model compound for heterogeneous photocatalysis onto TiO₂, *Chemosphere*, 64 (2006) 1128-1133.
- [66] K.V. Kumar, K. Porkodi, F. Rocha, Langmuir–Hinshelwood kinetics – A theoretical study, *Catalysis Communications*, 9 (2008) 82-84.
- [67] D. Chen, F. Li, A.K. Ray, Effect of mass transfer and catalyst layer thickness on photocatalytic reaction, *AIChE Journal*, 46 (2000) 1034-1045.
- [68] R. Ghamarpoor, A. Fallah, M. Jamshidi, A review of synthesis methods, modifications, and mechanisms of ZnO/TiO₂-based photocatalysts for photodegradation of contaminants, *ACS Omega*, 9 (2024) 25457-25492.
- [69] M. D'Arienzo, R. Scotti, L. Wahba, C. Battocchio, E. Bemporad, A. Nale, F. Morazzoni, Hydrothermal N-doped TiO₂: explaining photocatalytic properties by electronic and magnetic identification of N active sites, *Applied Catalysis B: Environmental*, 93 (2009) 149-155.
- [70] Y. Park, W. Kim, H. Park, T. Tachikawa, T. Majima, W. Choi, Carbon-doped TiO₂ photocatalyst synthesized without using an external carbon precursor and the visible light activity, *Applied Catalysis B: Environmental*, 91 (2009) 355-361.
- [71] U. Tsutomu, Y. Tetsuya, T. Sigeru, A. Keisuke, Visible light-induced degradation of methylene blue on S-doped TiO₂, *Chemistry Letters*, 32 (2003) 330-331.

- [72] M.A. Barakat, R.I. Al-Hutailah, E. Qayyum, J. Rashid, J.N. Kuhn, Pt nanoparticles/TiO₂ for photocatalytic degradation of phenols in wastewater, *Environ Technol*, 35 (2014) 137-144.
- [73] L. Cui, Y. Wang, M. Niu, G. Chen, Y. Cheng, Synthesis and visible light photocatalysis of Fe-doped TiO₂ mesoporous layers deposited on hollow glass microbeads, *Journal of Solid State Chemistry*, 182 (2009) 2785-2790.
- [74] Q.R. Deng, X.H. Xia, M.L. Guo, Y. Gao, G. Shao, Mn-doped TiO₂ nanopowders with remarkable visible light photocatalytic activity, *Materials Letters*, 65 (2011) 2051-2054.
- [75] D. Zhao, G. Sheng, C. Chen, X. Wang, Enhanced photocatalytic degradation of methylene blue under visible irradiation on graphene@TiO₂ dyade structure, *Applied Catalysis B: Environmental*, 111-112 (2012) 303-308.
- [76] K. Woan, G. Pyrgiotakis, W. Sigmund, Photocatalytic carbon-nanotube–TiO₂ composites, *Advanced Materials*, 21 (2009) 2233-2239.
- [77] G. Xi, Y. Yan, Q. Ma, J. Li, H. Yang, X. Lu, C. Wang, Synthesis of multiple-shell WO₃ hollow spheres by a binary carbonaceous template route and their applications in visible-light photocatalysis, *Chemistry*, 18 (2012) 13949-13953.
- [78] J. Tang, Z. Zou, J. Ye, Photocatalytic decomposition of organic contaminants by Bi₂WO₆ under visible light irradiation, *Catalysis Letters*, 92 (2004) 53-56.
- [79] M.D. Quinn, N.H. Ho, S.M. Notley, Aqueous dispersions of exfoliated molybdenum disulfide for use in visible-light photocatalysis, *ACS Appl Mater Interfaces*, 5 (2013) 12751-12756.
- [80] J. Ungelenk, C. Feldmann, Synthesis of faceted β-SnWO₄ microcrystals with enhanced visible-light photocatalytic properties, *Chemical Communications*, 48 (2012) 7838-7840.
- [81] M. Zhang, Y. Yang, X. An, L.-a. Hou, A critical review of g-C₃N₄-based photocatalytic membrane for water purification, *Chemical Engineering Journal*, 412 (2021) 128663.
- [82] S. Higashimoto, N. Kitao, N. Yoshida, T. Sakura, M. Azuma, H. Ohue, Y. Sakata, Selective photocatalytic oxidation of benzyl alcohol and its derivatives into corresponding aldehydes by molecular oxygen on titanium dioxide under visible light irradiation, *Journal of Catalysis*, 266 (2009) 279-285.
- [83] X. Ji, Y. Chen, B. Paul, S. Vadivel, Photocatalytic oxidation of aromatic alcohols over silver supported on cobalt oxide nanostructured catalyst, *Journal of Alloys and Compounds*, 783 (2019) 583-592.
- [84] O. Tomita, T. Otsubo, M. Higashi, B. Ohtani, R. Abe, Partial oxidation of alcohols on visible-light-responsive WO₃ photocatalysts loaded with palladium oxide cocatalyst, *ACS Catalysis*, 6 (2016) 1134-1144.
- [85] A. Tanaka, K. Hashimoto, H. Kominami, Selective photocatalytic oxidation of aromatic alcohols to aldehydes in an aqueous suspension of gold nanoparticles supported on cerium(iv) oxide under irradiation of green light, *Chemical Communications*, 47 (2011) 10446-10448.
- [86] S. Meng, X. Ye, X. Ning, M. Xie, X. Fu, S. Chen, Selective oxidation of aromatic alcohols to aromatic aldehydes by BN/metal sulfide with enhanced photocatalytic activity, *Applied*

Catalysis B: Environmental, 182 (2016) 356-368.

[87] M.A. Nasalevich, E.A. Kozlova, T.P. Lyubina, A.V. Vorontsov, Photocatalytic oxidation of ethanol and isopropanol vapors on cadmium sulfide, *Journal of Catalysis*, 287 (2012) 138-148.

[88] H. She, Y. Sun, S. Li, J. Huang, L. Wang, G. Zhu, Q. Wang, Synthesis of non-noble metal nickel doped sulfide solid solution for improved photocatalytic performance, *Applied Catalysis B: Environmental*, 245 (2019) 439-447.

[89] X. Wang, K. Maeda, A. Thomas, K. Takanabe, G. Xin, J.M. Carlsson, K. Domen, M. Antonietti, A metal-free polymeric photocatalyst for hydrogen production from water under visible light, *Nat Mater*, 8 (2009) 76-80.

[90] Y. Wang, X. Wang, M. Antonietti, Polymeric graphitic carbon nitride as a heterogeneous organocatalyst: from photochemistry to multipurpose catalysis to sustainable chemistry, *Angew Chem Int Ed Engl*, 51 (2012) 68-89.

[91] L. Zhang, D. Liu, J. Guan, X. Chen, X. Guo, F. Zhao, T. Hou, X. Mu, Metal-free g-C₃N₄ photocatalyst by sulfuric acid activation for selective aerobic oxidation of benzyl alcohol under visible light, *Materials Research Bulletin*, 59 (2014) 84-92.

[92] S. Verma, R.N. Baig, M.N. Nadagouda, R.S. Varma, Selective oxidation of alcohols using photoactive VO@g-C₃N₄, *ACS Sustainable Chemistry & Engineering*, 4 (2016) 1094-1098.

[93] W.-J. Ong, L.-L. Tan, Y.H. Ng, S.-T. Yong, S.-P. Chai, Graphitic carbon nitride (g-C₃N₄)-based photocatalysts for artificial photosynthesis and environmental remediation: are we a step closer to achieving sustainability?, *Chemical Reviews*, 116 (2016) 7159-7329.

[94] Z. Wu, X. Huang, H. Zheng, P. Wang, G. Hai, W. Dong, G. Wang, Aromatic heterocycle-grafted NH₂-MIL-125(Ti) via conjugated linker with enhanced photocatalytic activity for selective oxidation of alcohols under visible light, *Applied Catalysis B: Environmental*, 224 (2018) 479-487.

[95] G. Lu, X. Huang, Z. Wu, Y. Li, L. Xing, H. Gao, W. Dong, G. Wang, Construction of covalently integrated core-shell TiO₂ nanobelts@COF hybrids for highly selective oxidation of alcohols under visible light, *Applied Surface Science*, 493 (2019) 551-560.

[96] G. Lu, X. Huang, Y. Li, G. Zhao, G. Pang, G. Wang, Covalently integrated core-shell MOF@COF hybrids as efficient visible-light-driven photocatalysts for selective oxidation of alcohols, *Journal of Energy Chemistry*, 43 (2020) 8-15.

[97] S. Samanta, S. Khilari, D. Pradhan, R. Srivastava, An efficient, visible light driven, selective oxidation of aromatic alcohols and amines with O₂ Using BiVO₄/g-C₃N₄ nanocomposite: a systematic and comprehensive study toward the development of a photocatalytic process, *ACS Sustainable Chemistry & Engineering*, 5 (2017) 2562-2577.

[98] L. Sun, B. Li, X. Chu, N. Sun, Y. Qu, X. Zhang, I. Khan, L. Bai, L. Jing, Synthesis of Si-O-bridged g-C₃N₄/WO₃ 2D-heterojunctional nanocomposites as efficient photocatalysts for aerobic alcohol oxidation and mechanism insight, *ACS Sustainable Chemistry & Engineering*, 7 (2019) 9916-9927.

[99] J. Yan, G. Wu, N. Guan, L. Li, Nb₂O₅/TiO₂ heterojunctions: synthesis strategy and

photocatalytic activity, *Applied Catalysis B: Environmental*, 152-153 (2014) 280-288.

[100] S.K. Verma, R. Verma, Y.R. Girish, F. Xue, L. Yan, S. Verma, M. Singh, Y. Vaishnav, A.B. Shaik, R.R. Bhandare, K.P. Rakesh, K.S. Sharath Kumar, K.S. Rangappa, Heterogeneous graphitic carbon nitrides in visible-light-initiated organic transformations, *Green Chemistry*, 24 (2022) 438-479.

[101] A. Akhundi, A. Badiei, G.M. Ziarani, A. Habibi-Yangjeh, M.J. Muñoz-Batista, R. Luque, Graphitic carbon nitride-based photocatalysts: toward efficient organic transformation for value-added chemicals production, *Molecular Catalysis*, 488 (2020) 110902.

[102] L. Chen, J. Tang, L.-N. Song, P. Chen, J. He, C.-T. Au, S.-F. Yin, Heterogeneous photocatalysis for selective oxidation of alcohols and hydrocarbons, *Applied Catalysis B: Environmental*, 242 (2019) 379-388.

[103] R. Binjhade, R. Mondal, S. Mondal, Continuous photocatalytic reactor: critical review on the design and performance, *Journal of Environmental Chemical Engineering*, 10 (2022) 107746.

[104] S. Mozia, Photocatalytic membrane reactors (PMRs) in water and wastewater treatment. A review, *Separation and Purification Technology*, 73 (2010) 71-91.

[105] M.E. Leblebici, G.D. Stefanidis, T. Van Gerven, Comparison of photocatalytic space-time yields of 12 reactor designs for wastewater treatment, *Chemical Engineering and Processing: Process Intensification*, 97 (2015) 106-111.

[106] D.D. Phan, F. Babick, M.T. Nguyen, B. Wessely, M. Stintz, Modelling the influence of mass transfer on fixed-bed photocatalytic membrane reactors, *Chemical Engineering Science*, 173 (2017) 242-252.

[107] S. Carbonaro, M.N. Sugihara, T.J. Strathmann, Continuous-flow photocatalytic treatment of pharmaceutical micropollutants: activity, inhibition, and deactivation of TiO₂ photocatalysts in wastewater effluent, *Applied Catalysis B: Environmental*, 129 (2013) 1-12.

[108] A. Manassero, M.L. Satuf, O.M. Alfano, Photocatalytic reactors with suspended and immobilized TiO₂: comparative efficiency evaluation, *Chemical Engineering Journal*, 326 (2017) 29-36.

[109] M.F.J. Dijkstra, A. Michorius, H. Buwalda, H.J. Panneman, J.G.M. Winkelman, A.A.C.M. Beenackers, Comparison of the efficiency of immobilized and suspended systems in photocatalytic degradation, *Catalysis Today*, 66 (2001) 487-494.

[110] I. Horovitz, D. Avisar, M.A. Baker, R. Grilli, L. Lozzi, D. Di Camillo, H. Mamane, Carbamazepine degradation using a N-doped TiO₂ coated photocatalytic membrane reactor: influence of physical parameters, *J Hazard Mater*, 310 (2016) 98-107.

[111] C. Regmi, S. Lotfi, J.C. Espíndola, K. Fischer, A. Schulze, A.I. Schäfer, Comparison of photocatalytic membrane reactor types for the degradation of an organic molecule by TiO₂-coated PES membrane, *Catalysts*, 10 (2020) 725.

[112] S. Murgolo, V. Yargeau, R. Gerbasi, F. Visentin, N. El Habra, G. Ricco, I. Lacchetti, M. Carere, M.L. Curri, G. Mascolo, A new supported TiO₂ film deposited on stainless steel for the photocatalytic degradation of contaminants of emerging concern, *Chemical Engineering*

Journal, 318 (2017) 103-111.

[113] T. Claes, A. Dilissen, M.E. Leblebici, T. Van Gerven, Translucent packed bed structures for high throughput photocatalytic reactors, *Chemical Engineering Journal*, 361 (2019) 725-735.

[114] V. Vaiano, O. Sacco, D. Pisano, D. Sannino, P. Ciambelli, From the design to the development of a continuous fixed bed photoreactor for photocatalytic degradation of organic pollutants in wastewater, *Chemical Engineering Science*, 137 (2015) 152-160.

[115] D. Li, H. Zheng, Q. Wang, X. Wang, W. Jiang, Z. Zhang, Y. Yang, A novel double-cylindrical-shell photoreactor immobilized with monolayer TiO₂-coated silica gel beads for photocatalytic degradation of Rhodamine B and Methyl Orange in aqueous solution, *Separation and Purification Technology*, 123 (2014) 130-138.

[116] A. Danion, J. Disdier, C. Guillard, O. Païssé, N. Jaffrezic-Renault, Photocatalytic degradation of imidazolinone fungicide in TiO₂-coated optical fiber reactor, *Applied Catalysis B: Environmental*, 62 (2006) 274-281.

[117] H. O'Neal Tugaoen, S. Garcia-Segura, K. Hristovski, P. Westerhoff, Compact light-emitting diode optical fiber immobilized TiO₂ reactor for photocatalytic water treatment, *Science of The Total Environment*, 613-614 (2018) 1331-1338.

[118] T. Van Gerven, G. Mul, J. Moulijn, A. Stankiewicz, A review of intensification of photocatalytic processes, *Chemical Engineering and Processing: Process Intensification*, 46 (2007) 781-789.

[119] M. Krivec, K. Žagar, L. Suhadolnik, M. Čeh, G. Dražić, Highly efficient TiO₂-based microreactor for photocatalytic applications, *ACS Appl Mater Interfaces*, 5 (2013) 9088-9094.

[120] S. Das, V.C. Srivastava, Microfluidic-based photocatalytic microreactor for environmental application: a review of fabrication substrates and techniques, and operating parameters, *Photochemical & Photobiological Sciences*, 15 (2016) 714-730.

[121] H. Maleki, V. Bertola, TiO₂ nanofilms on polymeric substrates for the photocatalytic degradation of methylene blue, *ACS Applied Nano Materials*, 2 (2019) 7237-7244.

[122] H. Eskandarloo, A. Badiei, M.A. Behnajady, G.M. Ziarani, UV-LEDs assisted preparation of silver deposited TiO₂ catalyst bed inside microchannels as a high efficiency microphotoreactor for cleaning polluted water, *Chemical Engineering Journal*, 270 (2015) 158-167.

[123] J. Zhang, H. Wu, L. Shi, Z. Wu, S. Zhang, S. Wang, H. Sun, Photocatalysis coupling with membrane technology for sustainable and continuous purification of wastewater, *Separation and Purification Technology*, 329 (2024) 125225.

[124] B. Van der Bruggen, M. Mänttari, M. Nyström, Drawbacks of applying nanofiltration and how to avoid them: a review, *Separation and Purification Technology*, 63 (2008) 251-263.

[125] V. Augugliaro, M. Litter, L. Palmisano, J. Soria, The combination of heterogeneous photocatalysis with chemical and physical operations: a tool for improving the photoprocess performance, *Journal of Photochemistry and Photobiology C: Photochemistry Reviews*, 7 (2006) 127-144.

- [126] R.K. Herz, Intrinsic kinetics of first-order reactions in photocatalytic membranes and layers, *Chemical Engineering Journal*, 99 (2004) 237-245.
- [127] J. Alvey, S. Dev, O. Quiñones, E. Dickenson, S. Aggarwal, A. Dotson, Photocatalytic membrane reactor utilizing immobile photocatalytic active layer on membranes for the removal of micropollutants, *ACS ES&T Water*, 3 (2023) 1050-1059.
- [128] T.E. Berger, C. Regmi, A.I. Schäfer, B.S. Richards, Photocatalytic degradation of organic dye via atomic layer deposited TiO₂ on ceramic membranes in single-pass flow-through operation, *Journal of Membrane Science*, 604 (2020) 118015.
- [129] S. Deepracha, L. Atfane, A. Ayral, M. Ogawa, Simple and efficient method for functionalizing photocatalytic ceramic membranes and assessment of its applicability for wastewater treatment in up-scalable membrane reactors, *Separation and Purification Technology*, 262 (2021) 118307.
- [130] S. Li, X. Zhang, R. Fang, Z. Cheng, Q. Xu, S. Ma, J. Xiong, P. Chen, G. Feng, Reactive ceramic membrane for efficient micropollutant purification with high flux by LED visible-light photocatalysis: device Level attempts, *Crystals*, 13 (2023) 651.
- [131] S. Liu, E. Véron, S. Lotfi, K. Fischer, A. Schulze, A.I. Schäfer, Poly (vinylidene fluoride) membrane with immobilized TiO₂ for degradation of steroid hormone micropollutants in a photocatalytic membrane reactor, *J Hazard Mater*, 447 (2023) 130832.
- [132] E. Luster, D. Avisar, I. Horovitz, L. Lozzi, M.A. Baker, R. Grilli, H. Mamane, N-Doped TiO₂-coated ceramic membrane for carbamazepine degradation in different water qualities, *Nanomaterials (Basel)*, 7 (2017).
- [133] N.G. Moustakas, F.K. Katsaros, A.G. Kontos, G.E. Romanos, D.D. Dionysiou, P. Falaras, Visible light active TiO₂ photocatalytic filtration membranes with improved permeability and low energy consumption, *Catalysis Today*, 224 (2014) 56-69.
- [134] D.C. Fabry, Y.A. Ho, R. Zapf, W. Tremel, M. Panthöfer, M. Rueping, T.H. Rehm, Blue light mediated C–H arylation of heteroarenes using TiO₂ as an immobilized photocatalyst in a continuous-flow microreactor, *Green Chemistry*, 19 (2017) 1911-1918.
- [135] C. Bottecchia, N. Erdmann, P.M. Tijssen, L.G. Milroy, L. Brunsveld, V. Hessel, T. Noel, Batch and flow synthesis of disulfides by visible-light-induced TiO₂ photocatalysis, *ChemSusChem*, 9 (2016) 1781-1785.
- [136] V. Nair, J.C. Colmenares, D. Lisovytskiy, Ultrasound assisted ZnO coating in a microflow based photoreactor for selective oxidation of benzyl alcohol to benzaldehyde, *Green Chemistry*, 21 (2019) 1241-1246.
- [137] S.R. Pradhan, V. Nair, D.A. Giannakoudakis, D. Lisovytskiy, J.C. Colmenares, Design and development of TiO₂ coated microflow reactor for photocatalytic partial oxidation of benzyl alcohol, *Molecular Catalysis*, 486 (2020) 110884.
- [138] S.R. Pradhan, D. Lisovytskiy, J.C. Colmenares, Flow photomicroreactor coated with monometal containing TiO₂ using sonication: a versatile tool for visible light oxidation, *Catalysis Communications*, 162 (2022) 106375.
- [139] T. Noël, Photochemical processes in continuous-flow reactors : from engineering

principles to chemical applications, in, World Scientific New Jersey, New Jersey, 2017.

[140] R. Molinari, C. Lavorato, P. Argurio, Recent progress of photocatalytic membrane reactors in water treatment and in synthesis of organic compounds. A review, *Catalysis Today*, 281 (2017) 144-164.

[141] C.P. Park, R.A. Maurya, J.H. Lee, D.P. Kim, Efficient photosensitized oxygenations in phase contact enhanced microreactors, *Lab Chip*, 11 (2011) 1941-1945.

[142] R.A. Maurya, C.P. Park, D.-P. Kim, Triple-channel microreactor for biphasic gas-liquid reactions: Photosensitized oxygenations, *Beilstein Journal of Organic Chemistry*, 7 (2011) 1158-1163.

[143] R. Molinari, A. Caruso, T. Poerio, Direct benzene conversion to phenol in a hybrid photocatalytic membrane reactor, *Catalysis Today*, 144 (2009) 81-86.

[144] R. Molinari, C. Lavorato, P. Argurio, Photocatalytic reduction of acetophenone in membrane reactors under UV and visible light using TiO_2 and Pd/TiO_2 catalysts, *Chemical Engineering Journal*, 274 (2015) 307-316.

[145] M. Siebert, R.R. Zimmermann, M. Armbrüster, R. Dittmeyer, Inkjet printing of GaPd_2 into micro-channels for the selective hydrogenation of acetylene, *ChemCatChem*, 9 (2017) 3733-3742.

[146] A.K. Mogalicherla, S. Lee, P. Pfeifer, R. Dittmeyer, Drop-on-demand inkjet printing of alumina nanoparticles in rectangular microchannels, *Microfluidics and Nanofluidics*, 16 (2014) 655-666.

[147] I. Fasaki, K. Siamos, M. Arin, P. Lommens, I. Van Driessche, S.C. Hopkins, B.A. Glowacki, I. Arabatzis, Ultrasound assisted preparation of stable water-based nanocrystalline TiO_2 suspensions for photocatalytic applications of inkjet-printed films, *Applied Catalysis A: General*, 411-412 (2012) 60-69.

[148] M. Singh, H.M. Haverinen, P. Dhagat, G.E. Jabbour, Inkjet printing-process and its applications, *Adv Mater*, 22 (2010) 673-685.

[149] G.E. Romanos, C.P. Athanasekou, F.K. Katsaros, N.K. Kanellopoulos, D.D. Dionysiou, V. Likodimos, P. Falaras, Double-side active TiO_2 -modified nanofiltration membranes in continuous flow photocatalytic reactors for effective water purification, *J Hazard Mater*, 211-212 (2012) 304-316.

[150] C. Adán, J. Marugán, S. Mesones, C. Casado, R. van Grieken, Bacterial inactivation and degradation of organic molecules by titanium dioxide supported on porous stainless steel photocatalytic membranes, *Chemical Engineering Journal*, 318 (2017) 29-38.

[151] T. Rathna, J. PonnanEttiyappan, D.R. Sudhakar, TiO_2 - WO_3 nanocube-polyaniline hierarchical membrane for efficient removal of chromium in a photocatalytic membrane reactor, *Water and Environment Journal*, n/a.

[152] I. Kolesnyk, J. Kujawa, H. Bubela, V. Konovalova, A. Burban, A. Cyganiuk, W. Kujawski, Photocatalytic properties of PVDF membranes modified with $\text{g-C}_3\text{N}_4$ in the process of Rhodamines decomposition, *Separation and Purification Technology*, 250 (2020) 117231.

[153] S. Kumar, Bhawna, R. Sharma, A. Gupta, K.K. Dubey, A.M. Khan, R. Singhal, R. Kumar, A. Bharti, P. Singh, R. Kant, V. Kumar, TiO₂ based photocatalysis membranes: an efficient strategy for pharmaceutical mineralization, *Science of The Total Environment*, 845 (2022) 157221.

[154] R. Weber, H. Chmiel, V. Mavrov, Characteristics and application of new ceramic nanofiltration membranes, *Desalination*, 157 (2003) 113-125.

[155] A. Joseph, A. Vijayanandan, Review on support materials used for immobilization of nano-photocatalysts for water treatment applications, *Inorganica Chimica Acta*, 545 (2023) 121284.

[156] M. Ateia, M.G. Alalm, D. Awfa, M.S. Johnson, C. Yoshimura, Modeling the degradation and disinfection of water pollutants by photocatalysts and composites: a critical review, *Science of The Total Environment*, 698 (2020) 134197.

[157] A.K. Ray, A.A.C.M. Beenackers, Novel swirl-flow reactor for kinetic studies of semiconductor photocatalysis, *AIChE Journal*, 43 (1997) 2571-2578.

[158] D. Ollis, Integrating photocatalysis and membrane technologies for water treatment, *Advanced Membrane Technology*, 984 (2003) 20.

[159] D.F. Ollis, Kinetic disguises in heterogeneous photocatalysis, *Topics in Catalysis*, 35 (2005) 217-223.

[160] D. Chen, A.K. Ray, Photocatalytic kinetics of phenol and its derivatives over UV irradiated TiO₂, *Applied Catalysis B: Environmental*, 23 (1999) 143-157.

[161] S. Zhou, A.K. Ray, Kinetic studies for photocatalytic degradation of Eosin B on a thin film of titanium dioxide, *Industrial & Engineering Chemistry Research*, 42 (2003) 6020-6033.

[162] D. Chen, F. Li, A.K. Ray, External and internal mass transfer effect on photocatalytic degradation, *Catalysis Today*, 66 (2001) 475-485.

[163] M.L. Satuf, J. Macagno, A. Manassero, G. Bernal, P.A. Kler, C.L.A. Berli, Simple method for the assessment of intrinsic kinetic constants in photocatalytic microreactors, *Applied Catalysis B: Environmental*, 241 (2019) 8-17.

[164] M.E. Leblebici, J. Rongé, J.A. Martens, G.D. Stefanidis, T. Van Gerven, Computational modelling of a photocatalytic UV-LED reactor with internal mass and photon transfer consideration, *Chemical Engineering Journal*, 264 (2015) 962-970.

[165] T.H. Rehm, S. Gros, P. Löb, A. Renken, Photonic contacting of gas-liquid phases in a falling film microreactor for continuous-flow photochemical catalysis with visible light, *Reaction Chemistry & Engineering*, 1 (2016) 636-648.

[166] M. Melchionna, P. Fornasiero, Updates on the roadmap for photocatalysis, *ACS Catalysis*, 10 (2020) 5493-5501.

[167] M. Qureshi, K. Takanabe, Insights on measuring and reporting heterogeneous photocatalysis: efficiency definitions and setup examples, *Chemistry of Materials*, 29 (2016) 158-167.

- [168] D.A. Giannakoudakis, A. Qayyum, M. Barczak, R.F. Colmenares-Quintero, P. Borowski, K. Triantafyllidis, J.C. Colmenares, Mechanistic and kinetic studies of benzyl alcohol photocatalytic oxidation by nanostructured titanium (hydro)oxides: Do we know the entire story?, *Applied Catalysis B: Environmental*, 320 (2023) 121939.
- [169] T. Del Giacco, M. Ranchella, C. Rol, G.V. Sebastiani, Photo-oxidation of some benzylic alcohols sensitized by colloidal TiO₂ in CH₃CN. A kinetic mechanistic study through quantum yield determinations, *Journal of Physical Organic Chemistry*, 13 (2000) 745-751.
- [170] M.R. Karimi Estahbanati, M. Feilizadeh, A. Babin, B. Mei, G. Mul, M.C. Iliuta, Selective photocatalytic oxidation of cyclohexanol to cyclohexanone: a spectroscopic and kinetic study, *Chemical Engineering Journal*, 382 (2020) 122732.
- [171] T. Fujioka, S.J. Khan, J.A. McDonald, L.D. Nghiem, Nanofiltration of trace organic chemicals: a comparison between ceramic and polymeric membranes, *Separation and Purification Technology*, 136 (2014) 258-264.
- [172] Y. Cong, J. Zhang, F. Chen, M. Anpo, Synthesis and characterization of nitrogen-doped TiO₂ nanophotocatalyst with high visible light activity, *The Journal of Physical Chemistry C*, 111 (2007) 6976-6982.
- [173] R. Cherrington, D.J. Hughes, S. Senthilarasu, V. Goodship, Inkjet-Printed TiO₂ nanoparticles from aqueous solutions for dye-sensitized solar cells (DSSCs), *Energy Technology*, 3 (2015) 866-870.
- [174] A. Kosmala, R. Wright, Q. Zhang, P. Kirby, Synthesis of silver nano particles and fabrication of aqueous Ag inks for inkjet printing, *Materials Chemistry and Physics*, 129 (2011) 1075-1080.
- [175] S. Lee, T. Boeltken, A.K. Mogalicherla, U. Gerhards, P. Pfeifer, R. Dittmeyer, Inkjet printing of porous nanoparticle-based catalyst layers in microchannel reactors, *Applied Catalysis A: General*, 467 (2013) 69-75.
- [176] D.A. Giannakoudakis, N. Farahmand, D. Łomot, K. Sobczak, T.J. Bandoz, J.C. Colmenares, Ultrasound-activated TiO₂/GO-based bifunctional photoreactive adsorbents for detoxification of chemical warfare agent surrogate vapors, *Chemical Engineering Journal*, 395 (2020) 125099.
- [177] S. Zhang, D. Liu, L. Song, E. Liu, Significant improvement of TiO₂ photocatalytic hydrogen generation by photothermic synergistic action and underlying mechanism, *International Journal of Hydrogen Energy*, 48 (2023) 26665-26675.
- [178] J. Lynch, C. Giannini, J.K. Cooper, A. Loiudice, I.D. Sharp, R. Buonsanti, Substitutional or interstitial site-selective nitrogen doping in TiO₂ nanostructures, *The Journal of Physical Chemistry C*, 119 (2015) 7443-7452.
- [179] C.R. Hubbard, R.L. Snyder, RIR - measurement and use in quantitative XRD, *Powder Diffraction*, 3 (2013) 74-77.
- [180] D.M. Tobaldi, R.C. Pullar, M.P. Seabra, J.A. Labrincha, Fully quantitative X-ray characterisation of Evonik Aeroxide TiO₂ P25®, *Materials Letters*, 122 (2014) 345-347.
- [181] B. Ohtani, O.O. Prieto-Mahaney, D. Li, R. Abe, What is Degussa (Evonik) P25?

Crystalline composition analysis, reconstruction from isolated pure particles and photocatalytic activity test, *Journal of Photochemistry and Photobiology A: Chemistry*, 216 (2010) 179-182.

[182] H.B. Wu, H.H. Hng, X.W. Lou, Direct synthesis of anatase TiO₂ nanowires with enhanced photocatalytic activity, *Adv Mater*, 24 (2012) 2567-2571.

[183] E. Bilgin Simsek, Solvothermal synthesized boron doped TiO₂ catalysts: photocatalytic degradation of endocrine disrupting compounds and pharmaceuticals under visible light irradiation, *Applied Catalysis B: Environmental*, 200 (2017) 309-322.

[184] K. Lv, H. Zuo, J. Sun, K. Deng, S. Liu, X. Li, D. Wang, (Bi, C and N) codoped TiO₂ nanoparticles, *J Hazard Mater*, 161 (2009) 396-401.

[185] H. Lindström, E. Magnusson, A. Holmberg, S. Södergren, S.-E. Lindquist, A. Hagfeldt, A new method for manufacturing nanostructured electrodes on glass substrates, *Solar Energy Materials and Solar Cells*, 73 (2002) 91-101.

[186] J. Liu, H. Wang, M. Antonietti, Graphitic carbon nitride "reloaded": emerging applications beyond (photo)catalysis, *Chem Soc Rev*, 45 (2016) 2308-2326.

[187] W. Zhang, A. Bariotaki, I. Smonou, F. Hollmann, Visible-light-driven photooxidation of alcohols using surface-doped graphitic carbon nitride, *Green Chemistry*, 19 (2017) 2096-2100.

[188] D.J. Martin, K. Qiu, S.A. Shevlin, A.D. Handoko, X. Chen, Z. Guo, J. Tang, Highly efficient photocatalytic H₂ evolution from water using visible light and structure-controlled graphitic carbon nitride, *Angewandte Chemie International Edition*, 53 (2014) 9240-9245.

[189] J. Liu, Y. Liu, N. Liu, Y. Han, X. Zhang, H. Huang, Y. Lifshitz, S.-T. Lee, J. Zhong, Z. Kang, Metal-free efficient photocatalyst for stable visible water splitting via a two-electron pathway, *Science*, 347 (2015) 970-974.

[190] B. Derby, Inkjet printing ceramics: from drops to solid, *Journal of the European Ceramic Society*, 31 (2011) 2543-2550.

[191] D. Jang, D. Kim, J. Moon, Influence of fluid physical properties on ink-jet printability, *Langmuir*, 25 (2009) 2629-2635.

[192] B. Liang, Y. Rao, X. Duan, The electrical properties and modulation of g-C₃N₄/β-As and g-C₃N₄/β-Sb heterostructures: a first principles study, *RSC Advances*, 9 (2019) 38724-38729.

[193] M.J. Lima, A.M.T. Silva, C.G. Silva, J.L. Faria, Graphitic carbon nitride modified by thermal, chemical and mechanical processes as metal-free photocatalyst for the selective synthesis of benzaldehyde from benzyl alcohol, *Journal of Catalysis*, 353 (2017) 44-53.

[194] F. Su, S.C. Mathew, G. Lipner, X. Fu, M. Antonietti, S. Blechert, X. Wang, mpg-C₃N₄-Catalyzed selective oxidation of alcohols using O₂ and visible Light, *Journal of the American Chemical Society*, 132 (2010) 16299-16301.

[195] O. Fontelles-Carceller, M.J. Muñoz-Batista, M. Fernández-García, A. Kubacka, Interface effects in sunlight-driven Ag/g-C₃N₄ composite catalysts: study of the toluene photodegradation quantum efficiency, *ACS Appl Mater Interfaces*, 8 (2016) 2617-2627.

[196] M.J. Lima, P.B. Tavares, A.M.T. Silva, C.G. Silva, J.L. Faria, Selective photocatalytic

oxidation of benzyl alcohol to benzaldehyde by using metal-loaded g-C₃N₄ photocatalysts, *Catalysis Today*, 287 (2017) 70-77.

[197] R. Zhang, M. Hummelgård, G. Lv, H. Olin, Real time monitoring of the drug release of rhodamine B on graphene oxide, *Carbon*, 49 (2011) 1126-1132.

[198] V.R. Batistela, D.S. Pellosi, F.D. de Souza, W.F. da Costa, S.M. de Oliveira Santin, V.R. de Souza, W. Caetano, H.P.M. de Oliveira, I.S. Scarminio, N. Hioka, pKa determinations of xanthene derivatives in aqueous solutions by multivariate analysis applied to UV-Vis spectrophotometric data, *Spectrochimica Acta Part A: Molecular and Biomolecular Spectroscopy*, 79 (2011) 889-897.

[199] T.X. Bui, H. Choi, Comment on “adsorption and desorption of oxytetracycline and carbamazepine by multiwalled carbon nanotubes”, *Environmental Science & Technology*, 44 (2010) 4828-4828.

[200] H. Lucida, J.E. Parkin, V.B. Sunderland, Kinetic study of the reaction of sulfamethoxazole and glucose under acidic conditions: I. effect of pH and temperature, *International Journal of Pharmaceutics*, 202 (2000) 47-62.

[201] J.M. Castaño-Ortiz, F. Courant, E. Gomez, M.M. García-Pimentel, V.M. León, J.A. Campillo, L.H.M.L.M. Santos, D. Barceló, S. Rodríguez-Mozaz, Combined exposure of the bivalve *Mytilus galloprovincialis* to polyethylene microplastics and two pharmaceuticals (citalopram and bezafibrate): bioaccumulation and metabolomic studies, *J Hazard Mater*, 458 (2023) 131904.

[202] A. Jess, P. Wasserscheid, W. John, Sons, *Chemical technology : an integral textbook*, Wiley-Vch, Weinheim, 2013.

[203] G. Ertl, H. Knözinger, F. Schüth, J. Weitkamp, *Handbook of heterogeneous catalysis*, 8 Volume set, Chapter 6.3, Wiley, 2008.

[204] C.N. Satterfield, *Mass transfer in heterogeneous catalysis*, Chapters 3 & 4, M.I.T. Press, Cambridge, MA, 1970.

[205] G. Charles, T. Roques-Carmes, N. Becheikh, L. Falk, J.-M. Commenge, S. Corbel, Determination of kinetic constants of a photocatalytic reaction in micro-channel reactors in the presence of mass-transfer limitation and axial dispersion, *Journal of Photochemistry and Photobiology A: Chemistry*, 223 (2011) 202-211.

[206] N. Kockmann, *Transport phenomena in micro process engineering*, Chapter 6.2, Springer Berlin Heidelberg, 2007.

[207] N. Padoin, C. Soares, An explicit correlation for optimal TiO₂ film thickness in immobilized photocatalytic reaction systems, *Chemical Engineering Journal*, 310 (2017) 381-388.

[208] C.T. Culbertson, S.C. Jacobson, J. Michael Ramsey, Diffusion coefficient measurements in microfluidic devices, *Talanta*, 56 (2002) 365-373.

[209] S. Banerjee, D.D. Dionysiou, S.C. Pillai, Self-cleaning applications of TiO₂ by photo-induced hydrophilicity and photocatalysis, *Applied Catalysis B: Environmental*, 176-177 (2015) 396-428.

- [210] R. Wang, K. Hashimoto, A. Fujishima, M. Chikuni, E. Kojima, A. Kitamura, M. Shimohigoshi, T. Watanabe, Light-induced amphiphilic surfaces, *Nature*, 388 (1997) 431-432.
- [211] M. Hatat-Fraile, R. Liang, M.J. Arlos, R.X. He, P. Peng, M.R. Servos, Y.N. Zhou, Concurrent photocatalytic and filtration processes using doped TiO₂ coated quartz fiber membranes in a photocatalytic membrane reactor, *Chemical Engineering Journal*, 330 (2017) 531-540.
- [212] K. Guan, Relationship between photocatalytic activity, hydrophilicity and self-cleaning effect of TiO₂/SiO₂ films, *Surface and Coatings Technology*, 191 (2005) 155-160.
- [213] D. Friedmann, A. Hakki, H. Kim, W. Choi, D. Bahnemann, Heterogeneous photocatalytic organic synthesis: state-of-the-art and future perspectives, *Green Chemistry*, 18 (2016) 5391-5411.
- [214] J.C. Colmenares, A. Magdziarz, O. Chernyayeva, D. Lisovytskiy, K. Kurzydłowski, J. Grzonka, Sonication-assisted low-temperature routes for the synthesis of supported Fe–TiO₂ econanomaterials: partial photooxidation of glucose and phenol aqueous degradation, *ChemCatChem*, 5 (2013) 2270-2277.
- [215] J.C. Colmenares, A. Magdziarz, K. Kurzydłowski, J. Grzonka, O. Chernyayeva, D. Lisovytskiy, Low-temperature ultrasound-promoted synthesis of Cr–TiO₂-supported photocatalysts for valorization of glucose and phenol degradation from liquid phase, *Applied Catalysis B: Environmental*, 134-135 (2013) 136-144.
- [216] Y. Shiraishi, T. Hirai, Selective organic transformations on titanium oxide-based photocatalysts, *Journal of Photochemistry and Photobiology C: Photochemistry Reviews*, 9 (2008) 157-170.

Appendix

A. Reactor and continuous-flow system

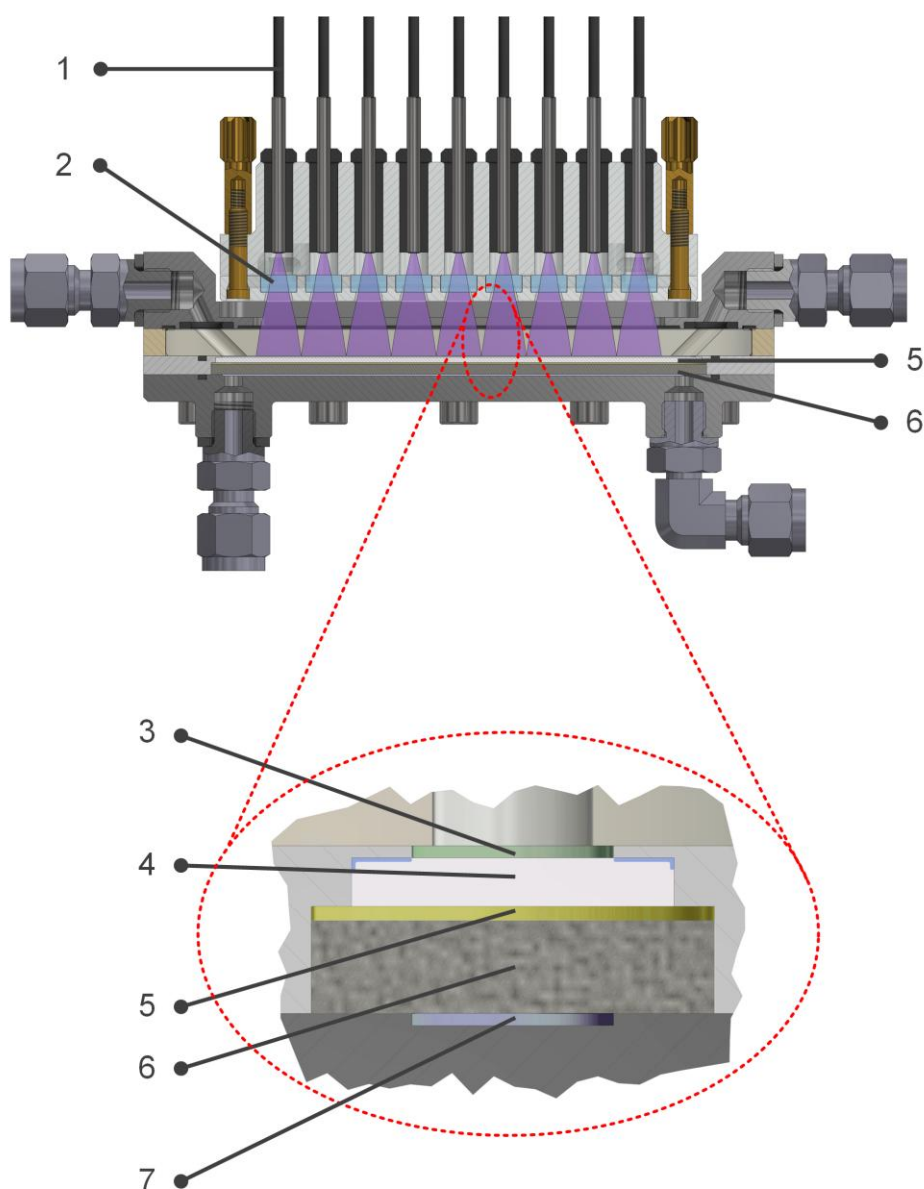


Figure A 1 Structure of the μ PMR: 1. optical fibers; 2. cylindrical lenses made of quartz; 3. upper microchannel; 4. ceramic NF membrane; 5. elastic buffer plate made of silicon (this plate is used to compensate the error of thickness of the membrane); 6. porous metal plate as a support for the membrane; 7. lower microchannel

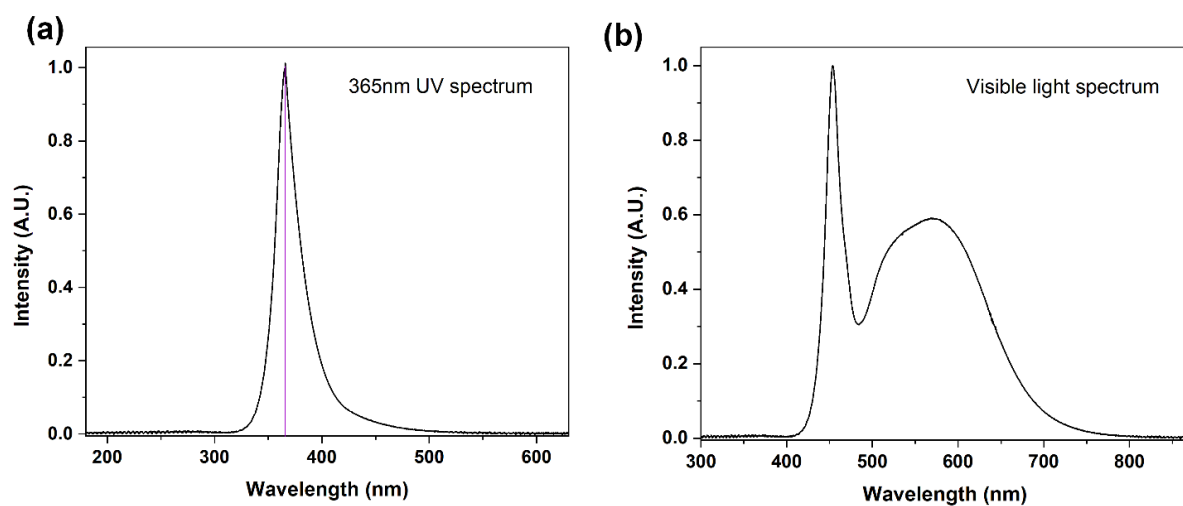


Figure A 2 Spectrum of the LED light used in this work: (a) UV light with 365nm wavelength; (b) white light

B. Characterization techniques

B1. Measuring the thickness of the coating using a 3D optical profiler

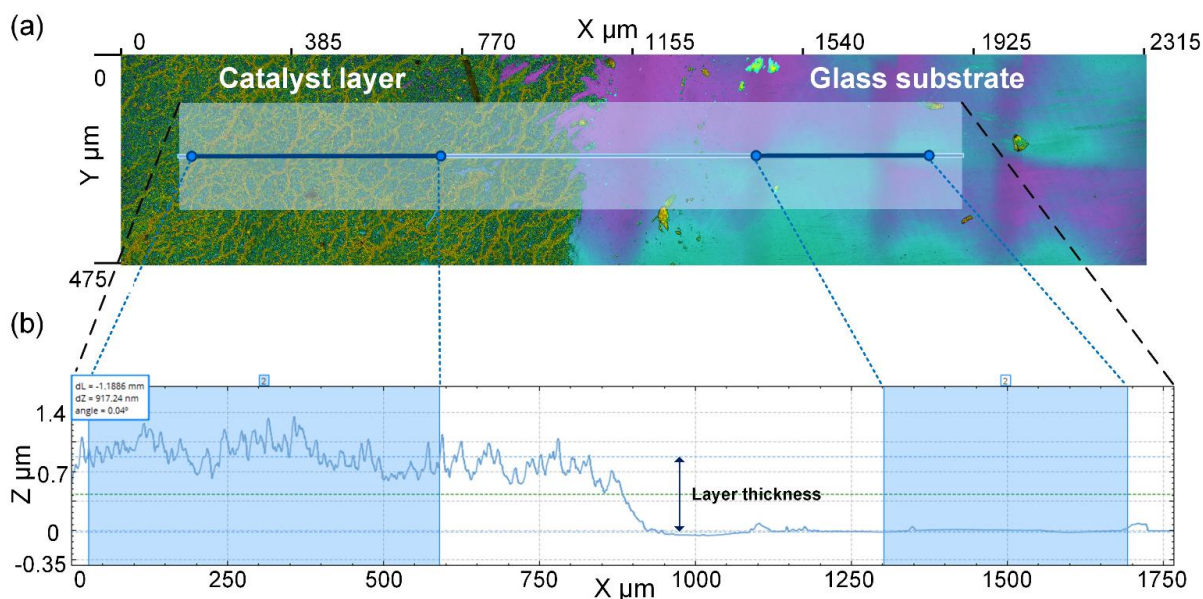


Figure B 1 Illustration of the measurement of the coated TiO_2 P25 layer thickness by 3D optical profiler: (a) 2D overview of the substrate and 9-layer coating, with the selected area used for thickness determination; (b) profile of the Z-value along the X axis, with Z-value being the mean along the Y axis in the selected area.

The 3D optical profiler scanned the sample in confocal mode. In the 2D overview, a rectangular area covering both catalyst coating and uncoated substrate was selected, as shown in Figure B 1 (a). Based on this selected area, the profiler generated a height profile (Z-value) along the X-axis, as illustrated in Figure B1(b). At each X-position, the Z-value represents the average surface height calculated across the full width (Y-direction) of the selected rectangle. To determine the coating thickness, two distinct regions—one on the coated area and one on the uncoated substrate—were selected along the X-axis in the profile. The difference in their average Z-values corresponds to the average coating thickness. This procedure was repeated for three independently prepared samples to obtain the final mean thickness. This method allows to measure the mean thickness of the coating in a certain area, which is advantageous when the coating surface is rough.

B2. Illustration of the layer transmission measurement

To measure the transmission of the TiO_2 coating of different layer numbers, an UV-Vis spectrometer was used to obtain the data at 365 nm wavelength, which equals the wavelength

used for the degradation test described in chapter 2.3. The sample was prepared by printing the TiO_2 layer on quartz glass of $0.5 \text{ cm} \times 2 \text{ cm}$ in size. During the measurement the sample was immersed into the model pollutant (RhB) solution (15 mg L^{-1}) contained in a quartz glass cuvette. The reason for not directly measuring the sample in air is that the actual environment in the degradation experiment is RhB aqueous solution. If the sample would be measured in air, the phase boundary (solid-liquid compared to solid-gas) is different, which can affect the light transmission as well as the absorbance because of the difference in refractive index. To prove this hypothesis, a comparative study was performed by measuring the transmission of the printed samples of 7 and 9 layers first in air and then in deionized water, respectively (Figure B 2). The transmission is normalized to the value obtained from the sample without any coating (transmission 100%). The result shows that if the measurement was done with the sample immersed in water, the transmission is higher, which means that more light can penetrate through the printed layers in water.

Table B 1 Results of the transmission at 365 nm of the samples in 7 layers and 9 layers

	7 layers				9 layers			
	Sample 1	Sample 2	Sample 3	Average	Sample 1	Sample 2	Sample 3	Average
Transmission in water (%)	2.77	2.98	3.61	3.12	0.91	1.63	1.07	1.2
Transmission in air (%)	1.72	1.63	2.31	1.88	0.67	1.19	0.95	0.94

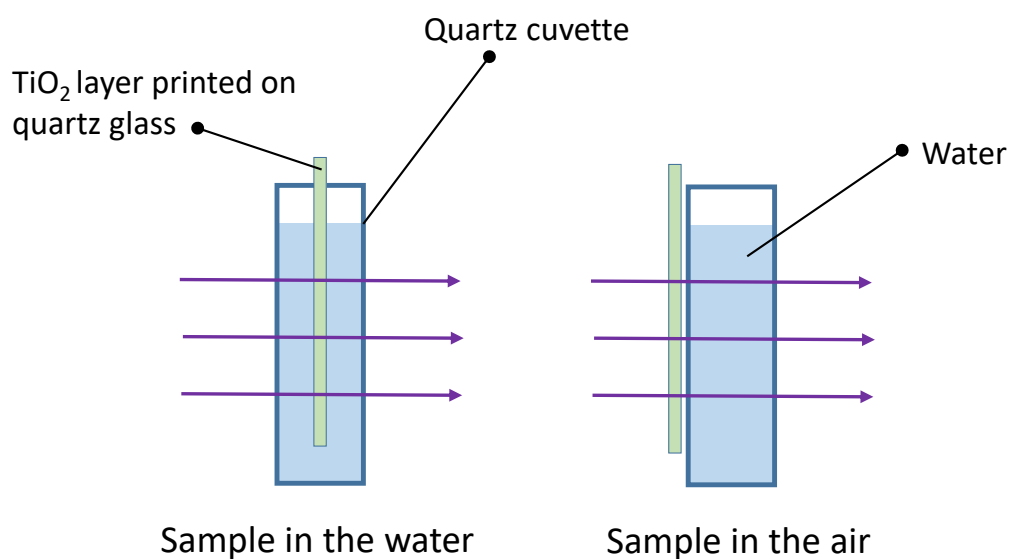


Figure B 2 Illustration of the transmission measurement in two cases

C. Steady-state analysis during the μ PMR experiment

Mass flow and mass balance validation for degradation for the 4 flow modes

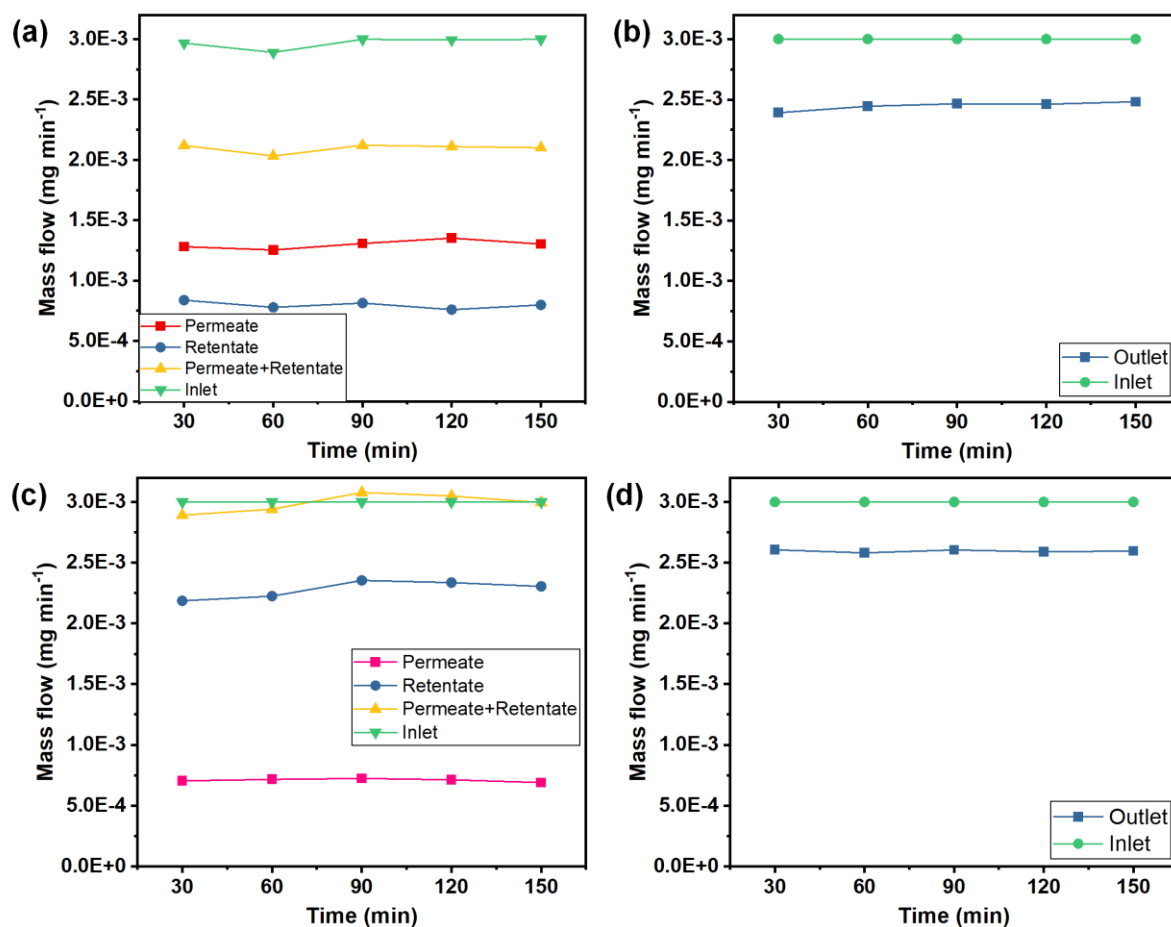


Figure C 1 Mass flow for different flow modes during the experiment: (a) Mode 1; (b) Mode 2; (c) Mode 3; (d) Mode 4.

Table C 1 Mass flow and mass balance validation for RhB degradation in UV under 4 flow modes

Mode 1	Mass flow (×10 ⁻³ mg min ⁻¹)				
Time (min)	Inlet	Permeate	Retentate	Permeate +Retentate	Degradation
30	2.97	1.28	0.84	2.12	0.85
60	2.89	1.25	0.78	2.03	0.86
90	3.00	1.31	0.81	2.12	0.88
120	2.99	1.35	0.76	2.11	0.88
150	3.00	1.30	0.80	2.10	0.90
Mode 2	Mass flow (×10 ⁻³ mg min ⁻¹)				
Time (min)	Inlet	Outlet			Degradation
30	3.00	2.39			0.61
60	3.02	2.44			0.58
90	3.02	2.47			0.55
120	3.01	2.46			0.55
150	3.02	2.48			0.54
Mode 3	Mass flow (×10 ⁻³ mg min ⁻¹)				
Time (min)	Inlet	Permeate	Retentate	Permeate +Retentate	
30	2.99	0.70	2.19	2.89	
60	3.00	0.72	2.22	2.94	
90	3.05	0.72	2.35	3.08	
120	2.99	0.71	2.34	3.05	
150	2.98	0.69	2.31	3.00	
Mode 4	Mass flow (×10 ⁻³ mg min ⁻¹)				
Time (min)	Inlet	Outlet			Degradation
30	3.01	2.61			0.40
60	3.01	2.58			0.43
90	2.99	2.60			0.39
120	3.02	2.59			0.43
150	3.01	2.60			0.41

Mass balance and mass flow for degradation of micropollutants

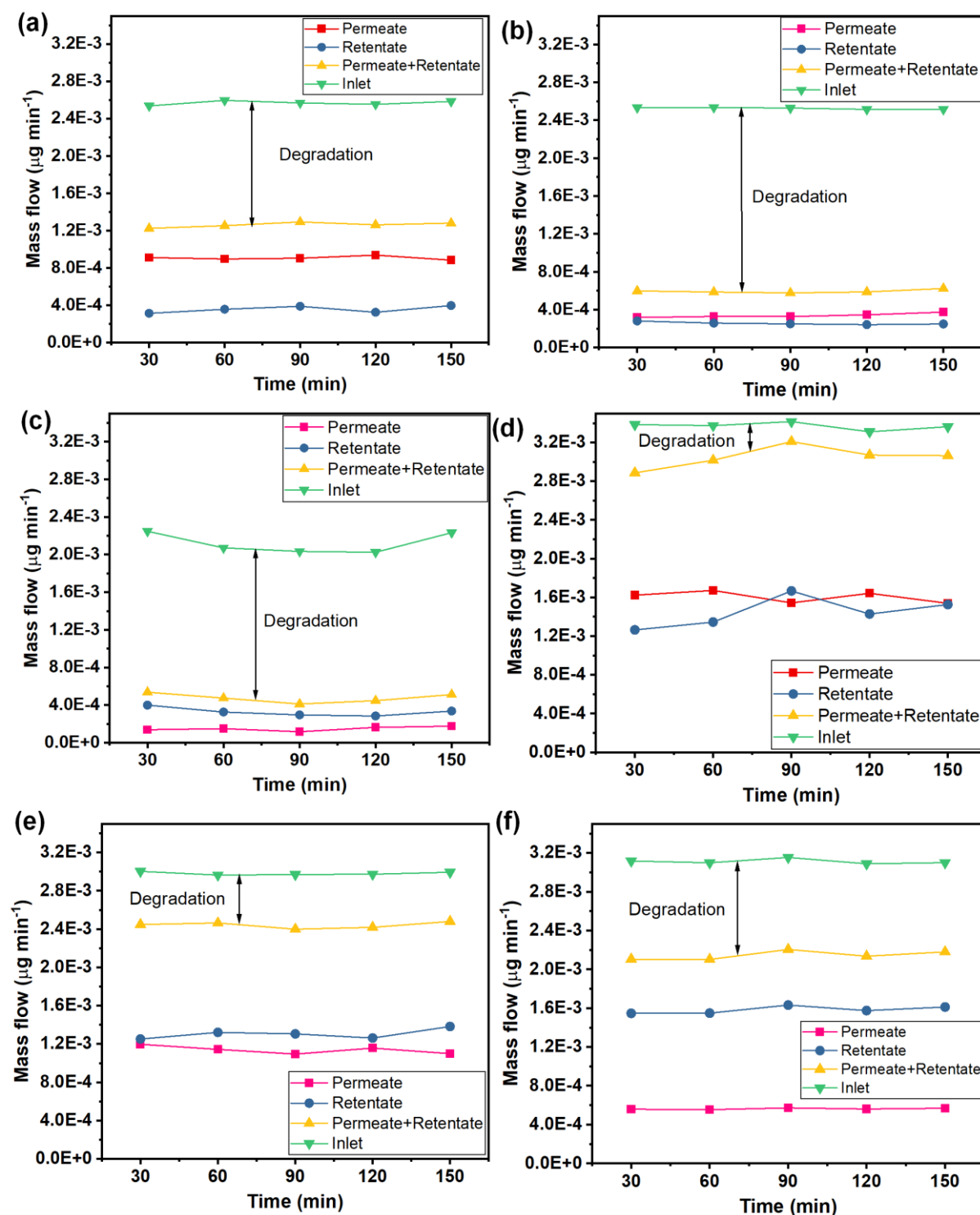


Figure C 2 Mass flow for micropollutant degradation under Mode 1 during the experiment: (a) CBZ under UV light; (b) SMX under UV light; (c) BZF under UV light; (d) CBZ under visible light; (e) SMX under visible light; (f) BZF under visible light.

Table C 2 Mass flow and mass balance validation for micropollutant degradation in UV under Mode 1

CBZ	Mass flow ($\times 10^{-3} \mu\text{g min}^{-1}$)				
Time (min)	Inlet	Permeate	Retentate	Permeate + Retentate	Degradation
30	2.54	0.91	0.31	1.22	1.31
60	2.59	0.90	0.36	1.25	1.34
90	2.57	0.90	0.39	1.29	1.28
120	2.55	0.94	0.32	1.26	1.29
150	2.58	0.88	0.40	1.28	1.30
SMX	Mass flow ($\times 10^{-3} \mu\text{g min}^{-1}$)				
Time (min)	Inlet	Permeate	Retentate	Permeate + Retentate	Degradation
30	2.53	0.32	0.28	0.60	1.94
60	2.54	0.33	0.26	0.59	1.95
90	2.53	0.33	0.25	0.58	1.95
120	2.51	0.35	0.24	0.59	1.93
150	2.51	0.37	0.25	0.62	1.89
BZF	Mass flow ($\times 10^{-3} \mu\text{g min}^{-1}$)				
Time (min)	Inlet	Permeate	Retentate	Permeate + Retentate	Degradation
30	2.25	0.14	0.40	0.54	1.71
60	2.07	0.15	0.33	0.47	1.60
90	2.03	0.12	0.30	0.41	1.62
120	2.02	0.16	0.28	0.45	1.58
150	2.23	0.18	0.34	0.51	1.72

Table C 3 Mass flow and mass balance validation for micropollutant degradation in visible light under Mode 1

CBZ	Mass flow ($\times 10^{-3} \mu\text{g min}^{-1}$)				
Time (min)	Inlet	Permeate	Retentate	Permeate + Retentate	Degradation
30	3.38	1.62	1.26	2.89	0.50
60	3.37	1.67	1.34	3.02	0.36
90	3.42	1.54	1.67	3.21	0.21
120	3.31	1.64	1.43	3.07	0.24
150	3.36	1.54	1.53	3.06	0.30
SMX	Mass flow ($\times 10^{-3} \mu\text{g min}^{-1}$)				
Time (min)	Inlet	Permeate	Retentate	Permeate + Retentate	Degradation
30	3.00	1.20	1.25	2.45	0.56
60	2.96	1.14	1.32	2.46	0.50
90	2.97	1.09	1.31	2.40	0.57
120	2.97	1.16	1.26	2.42	0.55
150	2.99	1.10	1.38	2.48	0.51
BZF	Mass flow ($\times 10^{-3} \mu\text{g min}^{-1}$)				
Time (min)	Inlet	Permeate	Retentate	Permeate + Retentate	Degradation
30	3.12	0.56	1.55	2.10	1.01
60	3.10	0.55	1.55	2.10	1.00
90	3.15	0.57	1.63	2.20	0.95
120	3.09	0.56	1.58	2.14	0.95
150	3.10	0.57	1.61	2.18	0.92

D. Investigation of potential cracking in coated membranes

As depicted in Figure 3-9, TiO₂ coated membranes exhibited enhanced permeance of RhB water solution. This observation was consistently reproduced across multiple independently prepared membranes, suggesting it is not an isolated result. This raised questions regarding potential cracks on the membrane surface. This section analyzes the observation.

Part I: SEM imaging

Initial investigations employed SEM imaging to inspect the membrane surface pre- and post-coating. As evidenced by Figure D 1, no obvious cracks were detected on the same membrane area before and after the coating process. This observation was consistent across 10 randomly selected sites on pristine membranes and those with the coating removed (images not shown for all 10 sites). Graphically, within the resolution limits of our equipment, no cracks were identified.

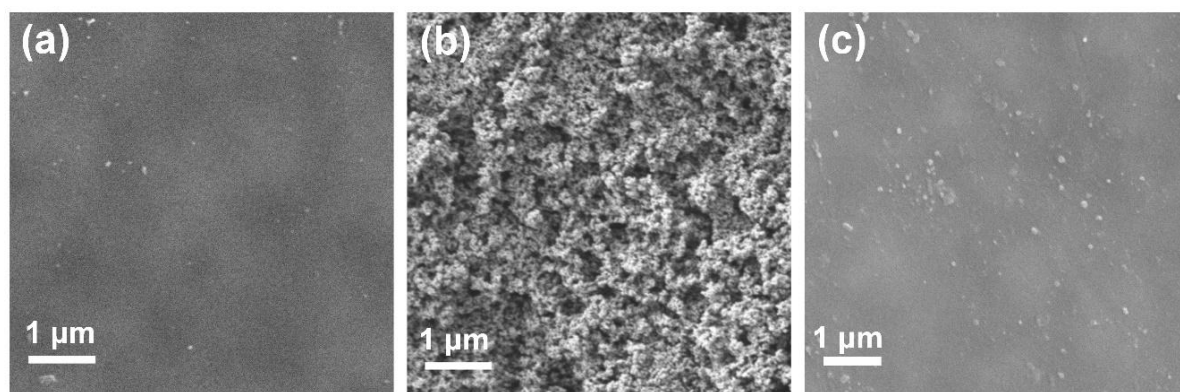


Figure D 1 Surface SEM image of: (a) pristine membrane; (b) membrane with inkjet-printed TiO₂ coating and calcination at 250 °C; (c) membrane with coating removed. Note that all images came from the same piece of membrane.

Part II: helium gas permeance test

While SEM imaging provides valuable insights, it cannot detect minor cracks or pinholes resulting from the coating process due to resolution limits. Hence, helium gas permeance tests were conducted on membranes before and after coating, with results presented in Table D 1.

For membranes 1-3, the procedure began with an initial gas permeance test on the pristine membranes. Subsequent to this, they were coated by inkjet-printing to achieve a 1 μm catalyst thickness, followed by 250 °C calcination. Afterwards, the coated membranes were re-tested for gas permeance. At last, the membrane's coating was removed by dry tissue paper and re-

tested for gas permeance.

The procedure for membranes 4-6 followed the same procedure of that for membranes 1-3, with the exception of the coating process. Here, a 0.5 ml of 0.5 wt.% TiO₂ water suspension (equivalent to ink concentration) was utilized. After a 12-hour natural drying period, proven to be sufficient for complete water evaporation (validated by gas permeance tests, data not presented), the membranes underwent a re-test.

Table D 1 Helium (He) permeance for 3 individual membranes before and after coating TiO₂, and with coating-removed (unit of the gas permeance Pe: 10⁻⁶ mol m⁻² sec⁻¹ Pa⁻¹).

Membrane No.	Pristine membrane	Membrane with TiO ₂ coating (250 °C calcination)	Membrane with TiO ₂ coating (by TiO ₂ water suspension and natural drying)	Membrane with coating removed
1	6.97	1.50	/	6.82
2	4.60	3.05	/	4.53
3	2.67	0.49	/	2.61
4	10.09	/	2.08	9.37
5	5.31	/	2.10	5.20
6	4.26	/	1.52	4.19

Given helium's molecular diameter of just 0.28 nm, while the average pore size of the membrane is 0.9 nm, even minor cracks in the membrane would result in a significant increase in gas permeance. However, our observations indicate that the coatings did not lead to increased gas permeance. In fact, a reduction in gas permeance was noted for both sets of membranes after coating. Especially for membranes 4-6, even without calcination, a reduction in gas permeance was observed. This suggests that the reduction in permeance is due to the additional resistance posed by the TiO₂ coating, as no reaction between the TiO₂ and the membrane surface is expected at room temperature for membranes 4-6.

Additionally, for the same membranes, once the coating was removed, the helium gas permeance reverted to the levels observed in the pristine membrane. Any minor decrease might be attributed to residual TiO₂ coating on the membrane surface, which can be challenging to

completely remove with tissue paper. This further corroborates the idea that the TiO_2 layer introduces resistance to gas permeance, and the absence of cracks is evident given the observation that the gas permeance can be restored.

Part III: water permeance test

To give a preliminary study on the influence of the TiO_2 coating, pure water permeance tests were extended to both pristine and coated membranes. Similar to the test shown in Table D 1, we tested membranes that had inkjet-printed TiO_2 layer followed by calcination, as well as membranes that had TiO_2 layer from TiO_2 water suspension and then naturally dried. Notably, even membranes with naturally dried TiO_2 layers showed a considerable increase in water permeance as shown in Figure D 2. This underscores the TiO_2 layer's pivotal role in altering permeance, possibly due to augmented wettability and hydrophilicity. Figure D 2 further highlights an enhanced water permeance under UV light, supporting the hypothesis of UV light fostering surface hydrophilicity via the generation of polar hydroxyl radicals, a phenomenon extensively documented in the literature [210].

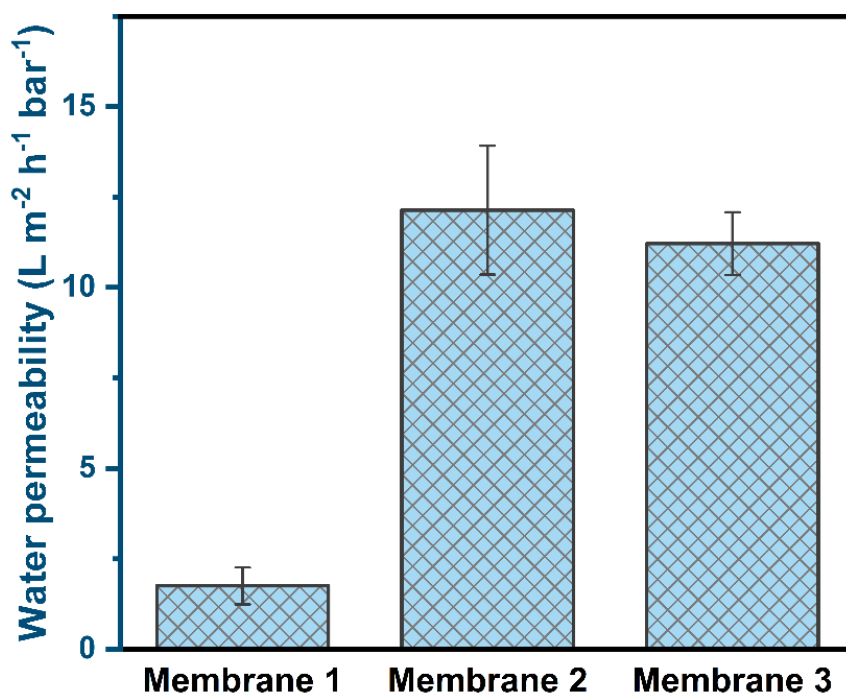


Figure D 2 Water permeance tested under dead-end flow mode for 3 membrane types: membrane 1: pristine membrane; membrane 2: with TiO_2 coating (by inkjet-printing and 250°C calcination); membrane 3: with TiO_2 coating (by TiO_2 water suspension and natural drying)

Part IV: manufacturer's insights on possible crack of this ceramic membrane

Additional details were provided by the membrane manufacturer Inopor (spinoff from

Fraunhofer IKTS, Germany) regarding the membrane performance at extreme conditions.

The ceramic membrane can remain stable and exhibit no behavioral changes at temperatures up to 600°C. Moreover, its performance remains consistent across a pH range of 2-12. This is particularly relevant considering the ink has a pH value of 10. It is also noteworthy that the membrane's supporting layer is comprised of mesoporous Al₂O₃. Given that the surface NF layer is also made of ceramic TiO₂, any potential cracks in the NF layer would manifest as extended fractures as per the manufacturer. Such cracks would be readily detectable through SEM or even through conventional microscopes.